

THESIS FOR THE DEGREE OF DOCTOR OF PHILOSOPHY

Adaptive Programming of RFID Inlays in the Reactive Near Field

Markus Frank



Department of Microtechnology and Nanoscience - MC2
CHALMERS UNIVERSITY OF TECHNOLOGY
Göteborg, Sweden 2018

Adaptive Programming of RFID Inlays in the Reactive Near Field
MARKUS FRANK
ISBN 978-91-7597-683-9

© MARKUS FRANK, 2018.

Doktorsavhandlingar vid Chalmers tekniska högskola
Ny serie nr 4364
ISSN 0346-718X

Technical report MC2-379
ISSN 1652-0769

Micro and Nanosystems Group
Electronics Materials and Systems Laboratory
Department of Microtechnology and Nanoscience - MC2
Chalmers University of Technology
SE-412 96 Göteborg, Sweden
Telephone + 46 (0) 31 – 772 1000

Cover: Principle of sensitive array including a single DTLL with balun excitation and phase shifter.

Typeset by the author using L^AT_EX.

Printed by Chalmers Reproservice
Göteborg, Sweden 2018

Till mina älskade, Gustav, Vilhelm and Linda

Und so wuchs ich heran, um viel vom Vater zu dulden; siehe nun zu was die Streitigkeiten geführt haben und was aus mir geworden ist...

Abstract

Radio frequency identification (RFID) offers a vast variety of options to improve the functionality and efficiency in the automated data collection (ADC) industry and Internet of Things (IoT). In the inventory process of RFID with passive data carriers, a population of battery less tags is located in the working range of an interrogator system. These tags contain transponders receiving operating energy from radio waves which can demodulate and modulate a digital signal from an RF carrier. The fundamental prerequisite in RFID is unique user identities (IDs) stored in the tag memories. Commonly, programming of these IDs occurs in the reactive near field, where the cavity of an RFID enabled bar code printer represents a typical example of such an environment. The two major challenges of user ID programming are the change of the electrical environment presented towards the transponder, as compared to the nominal far field or propagating near field conditions, and electromagnetic spatial selection, to prevent non-target tag programming.

This thesis presents the results from an industrial Ph.D. project, in collaboration between industry and university. In a first part, novel measurement and characterization techniques of RFID transponders are presented, with the main goal of understanding the impact of non-linearity on communication quality under altered reactive near field conditions.

The remaining part of the thesis addresses fundamental components needed in the concept of self adaptive reactive near field coupler technology, for geometry independent and spatially selective programming of RFID tags. The core of the technology is the differential transmission line loop (DTLL), exhibiting highly efficient and spatially selective coupling for varying inlay geometry; as such an array based spatial distribution of the reactive near field coupling is enabled. As exemplary simulations show, the versatility of the DTLL offers flexibility in array design, of creating a phase controlled reactive near field over the entire structure, which hence acts as a sensitive array. The elements act independently, where the amount of phase alteration in each element is a compensation for the geometrical size of the element itself. A fundamental property of the sensitive array is the independency of a software system, controlling the coupling elements. In other words, the reactive near field coupling of the array is self contained.

Keywords: Balun, DTLL, FOM, Phase compensation, Phase shifting, RFID, RNF, Source Impedance Shift, UHF.

Acknowledgments

This work would not have been possible without the support and decision of initiation from my company Sato. Many thanks are directed towards Mats Hedberg, my supervisor and site manager of Sato Techno Lab Europe, for motivating the industrial problem as a scientific one towards the management in Japan. Many years have now passed since the initiation of this project, which presented many challenges, but still with the persisting encouragement from management to complete.

My main supervisor Mattias Thorsell at MEL came in late in the project, which suffered from organizational challenges with time delays as consequence. However, we managed to find a good recipe for qualitative publications. Mattias' straight forward manner towards me, good academic overlook of the project in its entirety, with a road map towards the final goal, has helped pushing the project forward to the completion of this thesis. I am extremely impressed with his qualifications as a reviewer of my written work, and very thankful for his involvement in the project.

Many thanks are also directed towards Peter Enoksson, head of the EMSL Micro and Nanosystems group at MC2, for accepting me, a total stranger from industry and long time out of academia, as a PhD student.

Many warm thanks go out to Robert Eskilsson and his colleagues at Rohde & Schwarz Sweden and Germany for loan and support of instrumentation.

Although I am not present most of the time in my group at EMSL, at those times where I am, I experience warm friendship and good company from Henrik, Sofia, Elof, Per, Amin, Volodymyr and Qi Li.

My beautiful wife has patiently and quietly watched me spending excessive time, battling with difficult theoretical problems, completely missing out on the well needed support of the family. Without her warm caring of our lovely sons, Gustav and Vilhelm, while I was absent, both mentally and physically, this project would also not be possible.

Except Sato Techno Lab Europe, being my employer, this thesis work has also received financial support from the Swedish Research Council.

Markus Frank
Göteborg, Stråvalla 2018

List of Publications

Appended papers

This thesis is based on the following appended papers:

- Paper A.** M. Frank, M. Ferndahl, M. Thorsell and P. Enoksson, “Differential Impedance Measurement Method of RFID Transponder Chips at UHF,” in *2013 43d European Microwave Conference (EuMC)*, 6-10 October, Nuremberg, Germany, 2013, pp. 68-71.
- Paper B.** M. Frank, M. Thorsell, and P. Enoksson, “Shifted Source Impedance and Non-Linearity Impact on RFID Transponder Communication for Drive Level Offsets,” *IEEE Transactions on Microwave Theory and Techniques*, vol. 64, no. 1, pp. 299–309, January 2016.
- Paper C.** M. Frank, M. Thorsell, and P. Enoksson, “A Simplified Model for the Electromagnetical Interaction between Two Differentially Fed Sub-Wavelength Transmission Line Loops,” *Manuscript*.
- Paper D.** M. Frank, M. Thorsell, and P. Enoksson, “Differential Transmission Line Loop for RFID Reactive Near Field Coupling,” Accepted for publication in *IEEE Transactions on Microwave Theory and Techniques*.
- Paper E.** M. Frank, M. Thorsell and P. Enoksson, “Lumped Element Balun with Inherent Complex Impedance Transformation,” in *2017 IEEE MTT-S International Microwave Symposium (IMS)*, Honolulu, HI, USA, 4-9 June, Honolulu, HI, USA, 2017, pp. 1285-1288.
- Paper F.** M. Frank, M. Thorsell, and P. Enoksson, “Design Equations for Lumped Element Balun with Inherent Complex Impedance Transformation,” *IEEE Transactions on Microwave Theory and Techniques*, vol. 65, no. 12, pp. 5162-5170, 2017.
- Paper G.** M. Frank and P. Enoksson, “Phase Compensated Transmission Line for Leakage Field Coupling in UHF RFID Applications,” in *2013 7th European Conference on Antennas and Propagation (EuCAP)*, 8-12 April, Gothenburg, Sweden, 2013, pp. 1702-1706.

List of Acronyms

CG	–	Coupling Geometry
DTLL	–	Differential Transmission Line Loop
DUT	–	Device Under Test
EU	–	Extension Unit
FEM	–	Finite Element Method
FOM	–	Figure Of Merit
GPIB	–	General Purpose Interface Bus
GUI	–	Graphical User Interface
IG	–	Inlay Geometry
MATLAB	–	MATRIX LABORATORY
RF	–	Radio Frequency
RFID	–	Radio Frequency IDENTIFICATION
RFCW	–	Radio Frequency COMMUNICATION WINDOW
RFW	–	Radio Frequency WINDOW
SCPI	–	Standard Commands for Programmable Instruments
SG	–	Signal Ground
TDM	–	True Differential Mode
TRL	–	Transmission Line
VNA	–	Vector Network Analyzer

Contents

Abstract	v
Acknowledgments	vii
List of Publications	ix
List of Acronyms	xi
1 Introduction	1
1.1 Principle of an RFID system	1
1.2 Programming of unique user identities	2
1.3 RFID profiling in the printer	5
1.4 Current RNF coupler technology	6
1.5 The research topics	7
1.6 Organization of thesis	8
2 Electrical Perspective of RFID Programming	9
2.1 Measurement interfaces	9
2.2 The wired interface	11
2.2.1 Probe connection methods	11
2.2.2 Electrical verification of probe connection	13
2.3 The linear channel	14
2.3.1 Gain definitions	14
2.3.2 Q -value reduction	15
2.3.3 Circle theory	16
2.4 Summary of tool set	17
3 Transponder characterization	19
3.1 A review of reported work	19
3.2 General non-linear behavior	20
3.3 The approximation	23
3.4 Verification of source independency	24
3.5 Figure of merit calculation	27
3.5.1 Mismatch theory for source impedance shift	27
3.5.2 The $ \Delta\Gamma $ -value	29
3.5.3 Figure of merit	30
3.6 Measurement system	32

3.7	Measured FOM	33
3.7.1	Averaging	33
3.7.2	FOM results	34
3.8	Conclusions FOM characterization	38
4	Programming of RFID inlays in the reactive near field	39
4.1	Mutual interaction between inlays	39
4.2	The differential transmission line loop	41
4.2.1	The broadside coupling problem	43
4.2.2	Balun transformation	44
4.2.3	Predicted and measured results	45
4.3	Balun concepts	51
4.3.1	Reported work on balun transformation	51
4.3.2	Modification for complex impedance transformation	51
4.3.3	Analytic relationships	52
4.3.4	Experimental validation with demonstrators	55
4.3.5	Discussion on balun transformation for DTLL	58
5	Discussion: Implementation of DTLL in sensitive array applications	61
5.1	Conceptual idea	61
5.2	Predictive model	62
5.3	Example using a phase compensated line	63
5.4	Concluding remarks	64
6	Conclusions and future work	67
A	A short review of the RFID protocol	69
A.1	Baseband	69
A.2	Wake-up signal	70
A.3	Estimation of maximum required recording time	71
A.4	Minimum required system bandwidth	72
B	Graphical user interfaces	73

Chapter 1

Introduction

1.1 Principle of an RFID system

Radio frequency identification (RFID) at ultra high frequencies (UHF) is becoming a standard complement to common bar codes for the tracking of objects in supply chain management [1]. The general RFID system, as illustrated in Figure 1.1, consists of multiple interrogators and multiple antennas linked together in a network, with the purpose of inventory and data collection from a population of data carries.

The data carriers are realized as passive or active (battery assisted) tags. The term tag is used for the combination of an antenna and a transponder connected together, in which the transponder receives, stores and replies information back to the interrogator system. A special case of an RFID tag is an RFID inlay, where the antenna is a flexible metallic film. The term inlay, as opposed to tag, which is more general, will be used throughout this thesis and only passive transponders are considered.

The principle of communication is based on the broadcast of a radio signal, subject to a digital modulation format containing commands, from the interrogator system. The broadcast is followed by replies from the inlays, of which only one selected at a time may respond, also called half duplex communication. The inlay antenna is the frontend towards the energizing RF field and hence represents the source of energy needed by the transponder for proper operation. The transponder converts this energy to a DC bias for digital circuitry. The backward communication link from the inlay to the radio is based on backscattering, in which the inlay reflects and modulates a part of the radio signal back to the interrogator system. Note that one and the same inlay antenna is used for both receiving and backscattering of energy. The protocol enables a population of multiple RFID inlays, each with a unique user identity (ID), to be located in the same radio field. The singulation of inlays is done through an inventory process, performed by the interrogator system [2].

At UHF and higher frequencies the free space wavelength is of a size order where it is possible to design antenna structures which fit into standard bar code media. Since the antenna is tuned for a propagating wave, read and write distances of several meters can be achieved. There also exist RFID tags operating at lower frequencies, such as high frequency (HF) at 13.56 MHz [3]. In this case energy is transferred

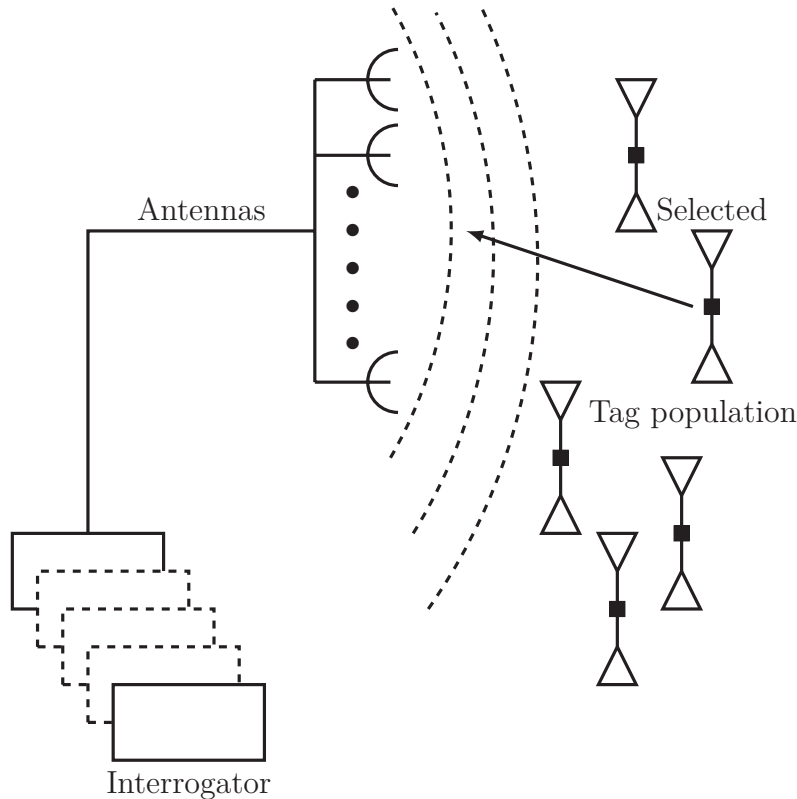


Figure 1.1: Principle of a general RFID system.

by pure inductive coupling. The “antenna” in this case is more or less an inductive coil of a number of turns which is connected to the transponder. This technology is characterized by shorter read and write distances but more robust RF near field performance.

1.2 Programming of unique user identities

A necessary task in an RFID system is the programming of unique user IDs to the inlay transponders. This is a critical and essential procedure, since without unique user IDs inlays are useless in the RFID inventory process. Note that the programming of user IDs precedes the actual end user application, which today is mostly concerned with inventory of unique data carriers. An RFID enabled printer is a common environment where this programming is carried out and represents the electrical conditions being of primary interest in this thesis. The task of an RFID enabled printer is not only to print visual bar code label media. The RFID label printing command also contains RFID commands with information intended for storage in the inlay transponder memory. In order to achieve the programming, the printer is equipped with reactive near field (RNF) coupler technology for wireless transfer of data to the transponder. The typical components of an RFID printer are shown in Figure 1.2.

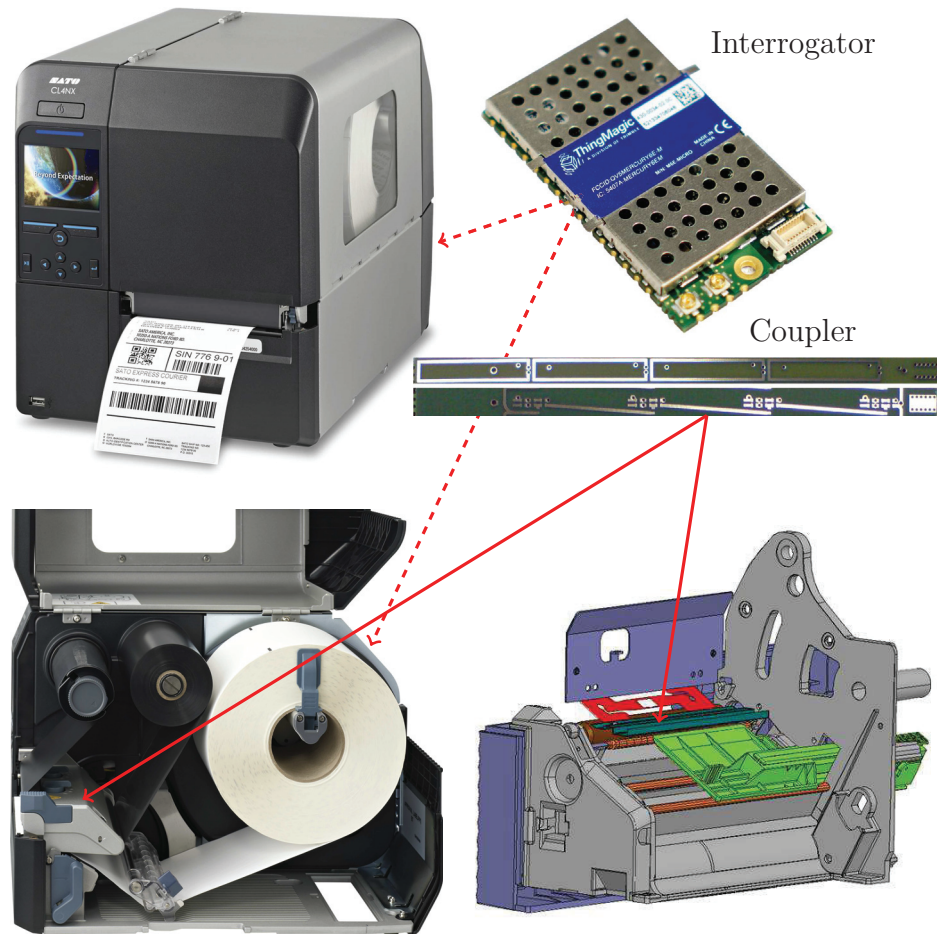


Figure 1.2: Components of an RFID printer.

In the end user application, for which the inlay antenna is designed, the inlay, interrogator antenna and other objects are located some distance apart. Spatial regions with these distances between objects are known as the far field or radiating near field. Certain electrical properties of the inlay, interrogator antenna and other objects will then not be electromagnetically affected by the presence of each other. A completely different situation, such as in an RFID enabled bar code printer, is illustrated in Figure 1.3. In a media roll of inlays to be programmed, the distance between neighbors may be as close as 3 mm, being well within a fraction of the radiating wavelength at UHF. Not only neighboring inlays may be close to the inlay targeted for programming, but also other objects such as media guides, thermal printhead and the wall of the media cavity may be in close vicinity, as seen in Figure 1.2. At such close distances, the electrical properties of all these objects are not independent of each others physical structure any longer. In other words, they are located in the reactive near field of one another. Electrically, the situation may be quantified by the mismatch condition at the interface between inlay antenna and transponder chip, which gives the relative amount of power transferred between the antenna and the transponder. Since the environment surrounding the inlay does not fulfill propagating field distances any longer, the electrical properties, when

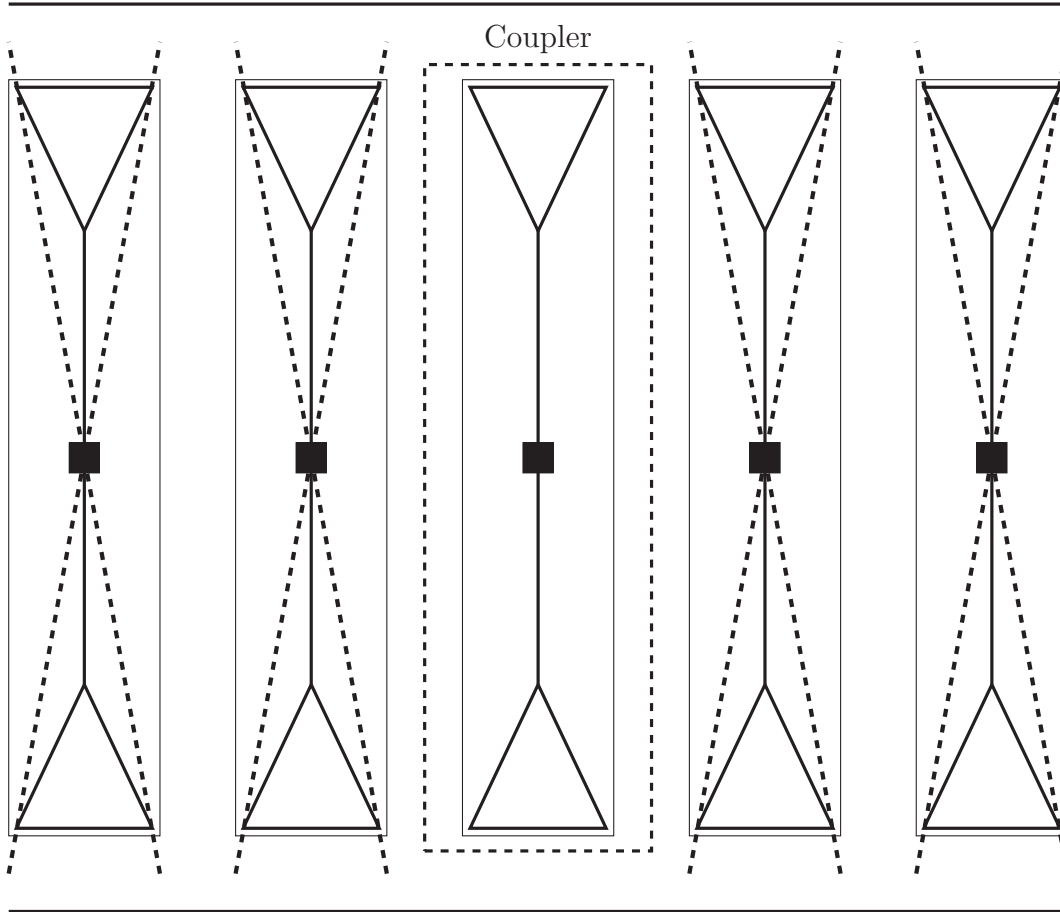


Figure 1.3: Illustration of the isolated programming problem in a printer cavity.

looking into the antenna port, presents some unknown source, which depends on the environment the inlay is located in. The only way to transfer information from the interrogator to the inlay transponder is over the air protocol by the near field coupler arrangement [4–7]. Since this needs to be done in an electromagnetically isolated manner to individual inlays, where the repeated distance between tag neighbors may be very small, it puts special requirements on the coupler.

The geometry of inlays may be very different so in a sense transparency towards inlay geometry is required. Furthermore, the transponder exhibits strong non-linear characteristics for an increased RF power drive level from the interrogator. This non-linearity has strong impact on the communication quality between interrogator and transponder. Therefore the drive level must be kept sufficiently low, as to allow stable communication between interrogator and inlay, yet still being high enough as to exceed the modulation threshold level. From another aspect, drive levels are also required to be as low as possible, in order to assure electromagnetic isolation between neighboring inlays. In summary these constraints put efficiency requirements on the RNF coupling between coupler and inlay antenna. Clearly, the combination of a dense inlay environment and big variety of geometry presents challenges in the coupler design.

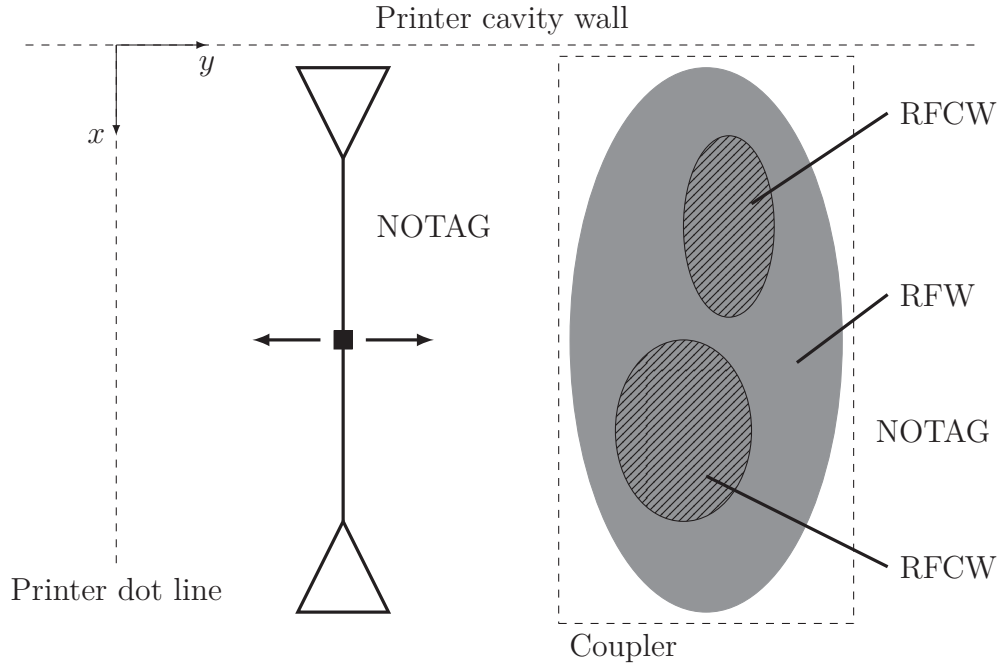


Figure 1.4: Classification of RFID communication regions in a printer cavity.

1.3 RFID profiling in the printer

The transparent programming of RFID inlays in a printer environment motivates the research presented in this thesis. Consider the usual test scenario in an RFID printer. The media path in the printer cavity may be regarded as some curved path. Seen from the RF perspective the vertical distance between the inlay and some structure which is not part of the media but which also conforms to the path, is very small. It can be assumed that this distance is also electrically small, in terms of the wavelength of the carrier wave energizing the inlay. Hence there is no loss in generality, when the media path is straightened out, in which the problem of profiling inlays is reduced to two dimensions in the xy -plane, as shown in Figure 1.4. The y -dimension follows the media path and the x -direction follows the width of the media path. Common media width dimensions are 2 in, 4 in and 6 in.

When an RFID inlay is in motion along the media path in a printer cavity, in which an RNF coupler is located at a fixed position along the media path, there will usually be one or several regions where the inlay may be programmed. These are regions with an RF coupling level between inlay and coupler reaching a certain threshold and above, where the transponder has a high enough bias to operate. Regions where the coupling is so low that no communication over the RFID protocol can be detected for any RF power level, in a fixed interval out from the interrogator, are known as NOTAG regions (Figure 1.4). The entire response from NOTAG to NOTAG region is known as the RF Window (RFW). This may consist of discontinuous sub regions with any type of response, provided there is a detection on the interrogator side. As the inlay enters the RFW, the mismatch becomes a function of power level,

due to the non-linear nature of the transponder. Within the RFW certain regions can be detected where both read and write communication is stable, denoted RF Communication Windows (RFCW).

If the coupler is a rigid structure, such as for example a set of transmission lines used for leakage field coupling, the shape of the RFW will be determined by the mutual interaction between the inlay and the coupler [4–6, Paper B]. This is an important observation. In a sense the combination of inlay, coupler and other objects of the printer exhibits a certain “profile” of programmability, which is unique for the particular inlay geometry being tested. As soon as the inlay geometry changes, the profile also changes. The term “RFID inlay profiling” is commonly used in the RFID printer community.

RFID profiling includes the whole component chain, such as interrogator transceiver, wireless channel with electromagnetic interaction between inlay antenna and printer cavity, and chip-nonlinearity. From the observation of the profile it is generally difficult to exactly determine the contributions of the different components to the profile shape. Furthermore, the testing is performed over the RFID protocol, where software parameters may also have an impact. It is concluded that, for sure, a well matched RNF coupler system will result in desirable properties, such as better continuity in the RFCW profile and wider RFCW regions at lower RF power levels, closer to the threshold.

1.4 Current RNF coupler technology

Conventionally, two types of RNF technologies are used to encode RFID inlays in RNF, which are, in principle, suitable for being fitted into printer cavities. The first type are static coupler designs which employ a rigid coupler circuit, such as a transmission line circuit on a printed circuit board (PCB). Since the circuit is rigid and inlay geometries generally have very high variability in form factor, the RF coupling behavior between coupler and inlay will also have a high variability. Hence, for each inlay type RFW profiles can be uniquely identified [7].

Apart from rigid coupler circuits, an alternative second type of RNF coupler technology are adaptive coupler designs with external control, also called semi-adaptive couplers [8–10]. In this technology, the coupler structure is split up into an array of a multiple of coupling elements. Each element is individually controlled by some external circuit and software. This means that for each type of inlay, regardless of its geometry, an adaptation can be performed in which a subset of coupling elements, electromagnetically conforming to the inlay geometry, is excited for optimum coupling. In the ideal case, optimum coupling regardless of inlay geometry can be achieved by having prior knowledge of which elements to activate. This information can only be obtained from profiling. Therefore, a scanning process of unknown inlay geometries is necessary. The information may then be stored in a memory and hence each inlay type needs to be profiled at least once. Clearly, for each new inlay type the process has to be repeated. Hence an adaptive coupler of said type is not operable as a stand alone component. It must be accompanied by a

software solution with necessary algorithms for the profiling process, required for external control of the elements to be activated. This possibly involves the whole printer system.

Regardless of which coupler type is considered, a single element coupler or an array configuration of multiple coupling elements, it is generally a non-optimized design, when the larger family of inlay geometries is taken into account. In the semi-adaptive case, a controlled excitation of certain groups of a multiple of coupling elements is needed to overcome the imperfection of the single element. Commonly, for both types of the above described conventional coupler types, there is a need of profiling, in order to adapt the coupling arrangement to a particular inlay, before an actual encoding can be performed. Either, for the static coupler type, the position of the inlay for optimum coupling must be known, or, for the semi-adaptive coupler solution, the inlay profile must be obtained and stored. If the resolution of the coupling element array is not high enough, inlay geometries may still exist which are not compatible with the coupler system. The resolution for future inlay types may furthermore be difficult to determine.

1.5 The research topics

The first step towards an optimal RNF coupler design, would be to first identify and characterize non-controllable parameters, which have a possible detrimental impact on the communication quality. Clearly, these parameters need to be taken into account in the design work. The most important parameters in this respect are the transponder RF front end and inlay antenna geometry, as previously discussed. The interface between the transponder RF front end and the inlay antenna port naturally divides up the problem into:

- A non-linear circuit related part
- A linear field theory related part

These two parts also define the structure of this thesis. The non-linear circuit part is concerned with the wired measurement, characterization and modeling of RFID transponders from different vendors, i.e., this part is not design related. Rather it deals with the study of existing designs. The characterized transponder chips are so small, in terms of the guided wavelength of a system supplying them with electrical power, that wavelength phenomena can be neglected. Rather, these components can be treated as pure electrical circuits with non-linear characteristics.

The field theoretic part is concerned with the design of efficient coupling structures, intended for RNF. This is a pure linear problem, but with strong dependency on wavelength. In this design work, inlay geometry is the non-controlled parameter. By considering the vast variation of geometries that exist, the challenge of designing efficient coupler technology for the larger family of inlays may seem rather daunting. It is however realized, by taking into account localized RNF coupling phenomena of the inlay, that still features common for all types of inlays may be identified, which enables an optimized design. This will be the primary focus in the second part of

this thesis. The term efficient should be interpreted as a strong electromagnetic interaction between inlay and coupler, yet still, being spatially selective. Embedded in this design problem is the electrical property of transponder response to shifted source impedance, which links back to the first part.

Generally speaking, transparency towards inlays is the primary objective in this thesis work. Inlays consist of geometries and transponder chips from varying vendors. Consequently, rather common electrical properties for transponder chips and inlay antennas are considered, without delving too much into any specific topology. The intention of the presented solution is to create a standard for reactive near field encoding of RFID tags, where no algorithms in software are needed, or any dependency on such a system. To the knowledge of the author, as of today, no such standard exists since there is no collaboration between competitors on the market and each competitor has individual solutions, where no solution conforms to the other; the RFID industry has not yet reached the maturity of creating such a standard.

1.6 Organization of thesis

This thesis is organized as follows. In Chapter 2 the electrical perspective of RFID profiling is explained, with fundamentals in measurement methods covered in Paper A and theoretic concepts, which are related to the research work behind this thesis. Chapter 3 starts with a general discussion around non-linearity, followed by mismatch theory needed for the definition of a figure of merit (FOM) being central for the work in Paper B. The central topic of Chapter 4 is highly efficient coupling elements including the presentation of the differential transmission line loop (DTLL), with material taken from Papers C and D, and balun theory covering work from Papers E and F. In the final Chapter 5, a number of the topics treated in the previous chapters are collected, where final coupler solutions with array implementations of DTLLs are discussed, with an exemplary case using the phase compensating concept developed in Paper G.

Chapter 2

Electrical Perspective of RFID Programming

The profiling process of inlays in the cavity of an RFID printer is an essential step to determine compatibility between inlays and the coupler system. It simply gives a yes and no criteria to, if certain inlay media can be used in the printer or not. It does not, however, give any more detailed information of the impact of different sub components in the communication link between transponder and interrogator. To obtain this information, a translation of the RFID profile into electrical parameters is needed. For the characterization of RFID inlays, as mentioned in Section 1.5, the interface between the RF frontend and the antenna port is natural. It divides the transponder-antenna system into a non-linear circuit part and a linear field theoretic part.

2.1 Measurement interfaces

In Section 1.3, the RFID-profile is discussed. An example of an RFW, resulting from a real test, is shown in Figure 2.1. With reference to Figure 1.4, for the case shown in Figure 2.1 the x -coordinate is fixed, but the RF power is swept within an interval. This is the typical test scenario since the x -directional inlay position is usually given by the customer specification. The abscissa, labeled y , indicates the position along the media path. The ordinate, labeled P_{AVS} , indicates the available output power from the interrogator. The different types of dots indicate the quality of communication, such as read only with empty blue circles, and full read and write performance with black filled circles. The functions $f_{RFW,RFCW}$ symbolize the yes ($f_{RFW,RFCW} = 1$) and no ($f_{RFW,RFCW} = 0$) criteria for reading and writing. An important observation is the dependency of profile on RF output power from the interrogator, where Figure 1.4 should be understood as the situation for a fixed power level.

From the profile in Figure 2.1, the interface between the two distinct types of phenomena discussed in Section 1.5 can be graphically illustrated. At one side of the interface, consider the interior of the RFW envelope. Certain phenomena, such as the offset between read and write thresholds of the transponder, and breakup of

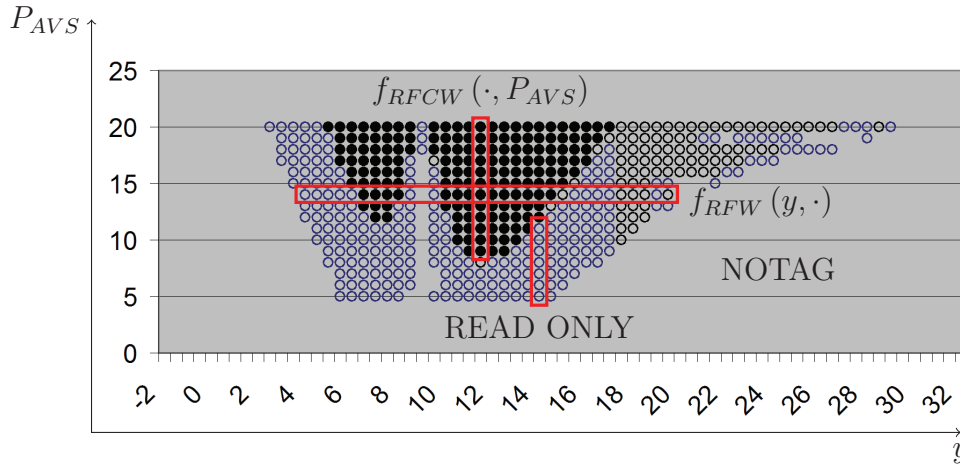


Figure 2.1: Example of RF window test profile carried out inside a printer cavity.

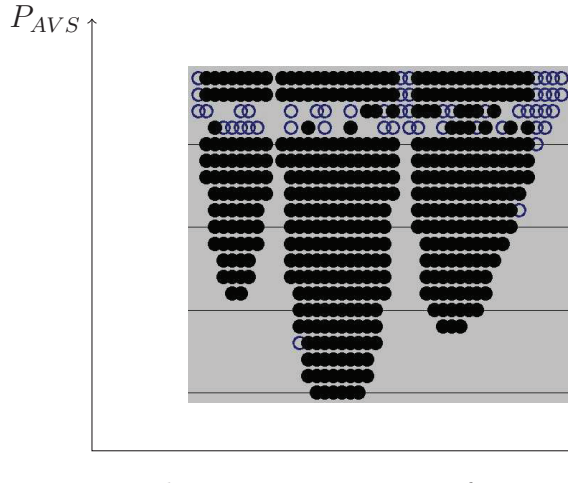


Figure 2.2: Broken up communication for excessive power levels.

communication for excessive power levels, such as the behavior shown in Figure 2.2, are observed. These are closely related to the non-linear characteristics of the transponder. In the linear case, a fixed offset between read and write power threshold is seen. The electrical characterization of these phenomena is preferably carried out with wired measurements, by a connection of instrumentation directly to the transponder chip terminals.

At the other side of the interface, consider the RFW envelope in Figure 2.1. It indicates the linear electromagnetic (EM) response of the coupler and inlay interaction, in a given cavity environment. The envelope can be understood as the spatial correspondence to a far field radiation pattern, but it is very important to realize that there is no, whatsoever, relation between the two since the reactive near field (RNF) behaviour is completely different from the far field propagating behavior, where certain approximations are allowed. This is a common misunderstanding in the community of automatic data collection (ADC). In this thesis a very important distinction between *antenna*, denoting a far or near field propagating device, and *coupler*, denoting a reactive near field device, is made, in which the term coupler will be used consistently.

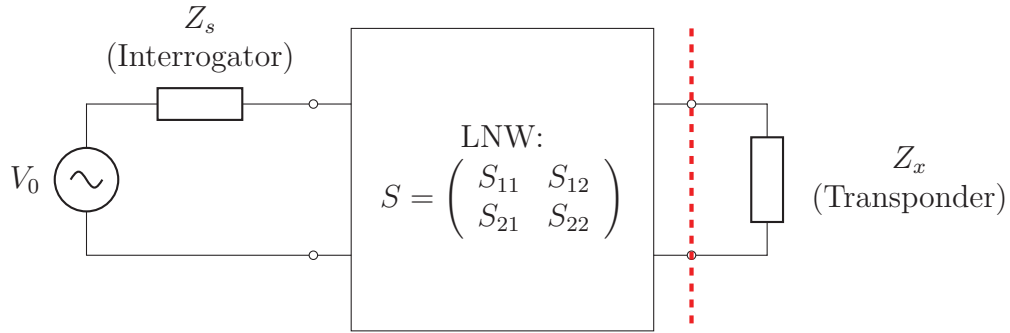


Figure 2.3: Block schematic representing the electromagnetic interaction between interrogator and transponder.

For a measured and simulated characterization, related to the research work of this thesis, Figures 2.1 and 2.2 are represented by the block schematic shown in Figure 2.3. Starting from the right of Figure 2.3, the impedance Z_x represents the non-linear circuit of the transponder chip RF front end, which is very small in terms of wavelength. The network LNW consists of a linear two-port S -parameter block, which represents the electromagnetic interaction, from the output of the interrogator to the transponder chip terminals. This interaction includes the coupler, inlay antenna and cavity environment, which from an electrical perspective can be considered as linear devices and hence the interaction may also be regarded as a linear channel, strongly dependent upon wavelength. The dashed line indicates the boundary between the two types of phenomena. The schematic in Figure 2.3 will be used as reference in the treatment to follow.

2.2 The wired interface

In wired electrical characterization of transponder chips, being the main topic of Chapter 3, the initial question is how a wired connection physically should be realized, which is flexible to a varying size factor of the transponder chip. Transponders from different vendors are generally different in size, but the electrical measurement method should be consistent, independent of vendor. Consistent here means that the measurement method should have no influence on certain electrical characteristics different chip types (different vendors) may have in common, for an accurate comparison.

2.2.1 Probe connection methods

In Paper A work is presented on bare wafer connection methods, with the purpose of finding a common connection method for transponder chips with different size factors. A dual probe connection, with differential excitation, is compared with the single probe connection, with a single ended excitation, as illustrated in Figure 2.4. The realization is shown in the bottom photo. In the left photo one of the probes

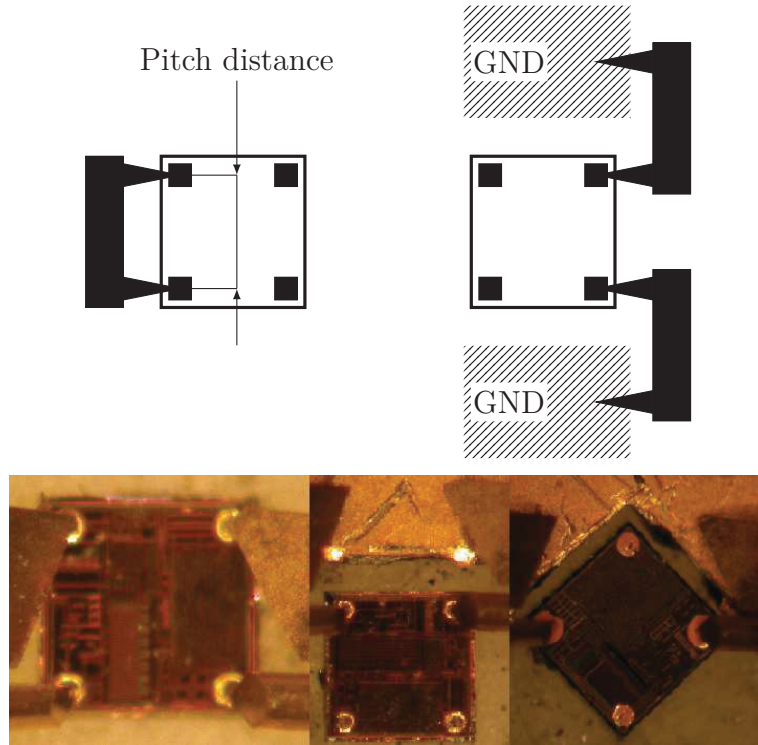


Figure 2.4: Top: Single probe connection (left) compared with dual probe connection (right) with common ground plane. Bottom: Realization.

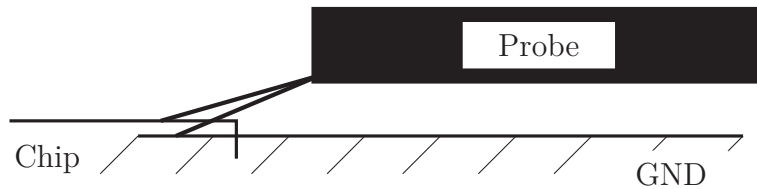


Figure 2.5: Illustration of vertical alignment (side view).

is used for mechanical support only. In the right photo an example of a larger size factor chip type is shown, where the distance between pads (diagonally aligned) is bigger than the pitch distance of the probe. Different transponder chip types have different distances between the connector pads and hence a single probe measurement method with fixed pitch distance between the probe tips would soon become useless, if the purpose is a comparison between a variety of chip types from different vendors. Typical pitch distances range between 25 and 1250 μm [11]. For the measurements, the 50A-GS-400-DP miniature coaxial Picoprobe from GGB Industries with CS-14 calibration substrate is used [11]. To verify the equivalence between the dual probe connection and the single probe connection, a chip type having a size factor suitable for both connection methods, is chosen as reference.

The vertical thicknesses of the chips also vary for different vendors. The situation is illustrated in Figure 2.5. The wafer thickness of the transponder chips are measured and typical values range from 70 to 150 μm . Hence, big differences are seen. From the more simple method, presented in Paper A, a more robust method being principally

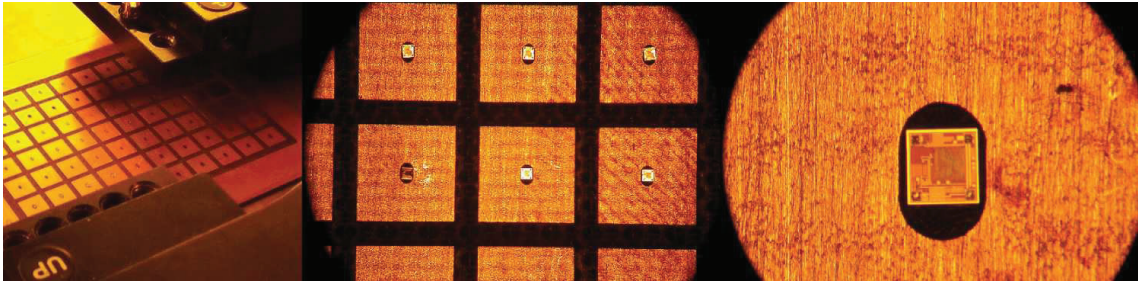


Figure 2.6: Substrate with seven-by-ten transponder chip array of which 6×5 is used.

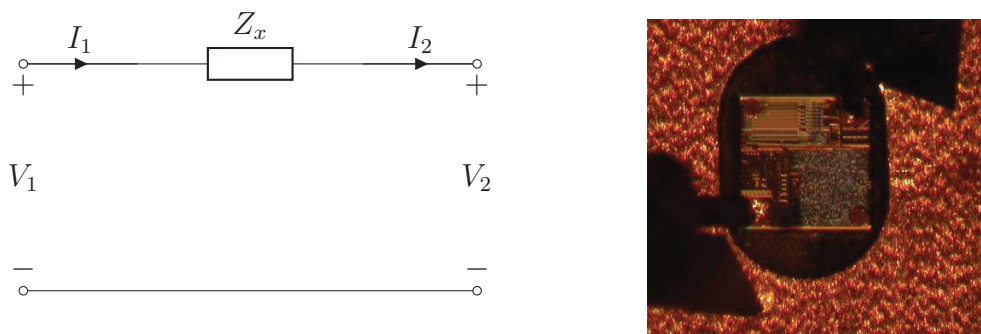


Figure 2.7: Left: General topology for DUT. Right: Dual probe connection.

the same, with a substrate comprising a 6 chip type by 5 individual array of pads, is used for the probed measurements of Paper B. Photos of the arrangement are shown in Fig. 2.6. Each pad consists of a quadratic ground plane with a milled hole in the middle. The holes have diameters providing some margin to the chip dimensions, which roughly vary from 700 to 900 microns in diameter. They are milled to an approximate depth corresponding to the wafer thicknesses, which vary from 70 to 150 microns. The flexibility of the probe tips in combination with a loose placement of the chips proves to work well for the electrical connection. It is additionally recommended to use a probe station with theta alignment, which is also a necessary requirement for the chip types having the biggest difference between wafer thickness and substrate ground. The dual probe connection is used consistently for all measurements. Note that the unmatched single ended and differential methods both provide a 100Ω source impedance from the two-port topology, as shown in Figure 2.7.

2.2.2 Electrical verification of probe connection

As the results in Paper A show, the one-port single ended and two-port differential measurement data agree well. This is also seen from carrying out several measurements on the same individual, where the obtained impedance value is stable. In the case of the reference type no significant differences could be seen between the single and dual probe connection. Mechanically, the dual probe connection has stable electrical characteristics, when lowering and lifting the probe tips a repeatable number of times, showing the usefulness for wired non-linear characterization.

2.3 The linear channel

A coupler can be seen as being part of a linear channel, describing the intermediate environment between the transponder RF frontend and the antenna port of the interrogator, with one of the main challenges being the highly efficient electromagnetically isolated communication with a single inlay in a dense environment of several. Two main aspects exist on the programming of RFID inlays in the RNF. One is the spatial selection, mainly in two dimensions, by means of electromagnetic phase manipulation. This problem is also evident from the discussion in Chapter 1. The other aspect is the coupling efficiency of a single coupling element, in an array arrangement of multiple elements.

The channel represented by LNW in Figure 2.3 may be thought of as incorporating also spatial selectivity, in the sense that if the inlay is located anywhere within an active area of the coupling arrangement, a regulatory functionality assures excitation of the transponder. Depending on the level of efficiency the LNW also incorporates resistive losses, being equivalent to any internal losses and outward radiation. Given this representation, a theoretical tool set traditionally used in amplifier theory is provided for a general analysis, without consideration needed to any specific coupler architecture [12]. In the coupler design process, being described in more detail in Chapter 4 and 5, specifics are treated. Comments on some important parameters from the tool set are, however, appropriate to mention at this point.

2.3.1 Gain definitions

The power transfer from the interrogator to the transponder may generally be described by the transducer gain, defined as [13]

$$G_t = \frac{\text{power delivered to the load}}{\text{power available from the source}} \quad (2.1)$$

which in terms of S -parameters is given as

$$G_t = \frac{P_L}{P_{AVS}} = \frac{(1 - |\Gamma_s|^2) |S_{21}|^2 (1 - |\Gamma_x|^2)}{|(1 - S_{11}\Gamma_s)(1 - S_{22}\Gamma_x) - S_{12}S_{21}\Gamma_s\Gamma_x|^2}. \quad (2.2)$$

Transducer gain takes into account mismatch between the interrogator and the LNW, as well as between the transponder and the LNW.

Matching of the input at the interrogator side implies $\Gamma_{in} = \Gamma_s^*$, where

$$\Gamma_{in} = S_{11} + \frac{S_{12}S_{21}\Gamma_x}{1 - S_{22}\Gamma_x} \quad (2.3)$$

which is the definition of power gain. The power gain, or operating power gain, is defined as

$$G_p = \frac{\text{power delivered to the load}}{\text{power delivered to the network}} \quad (2.4)$$

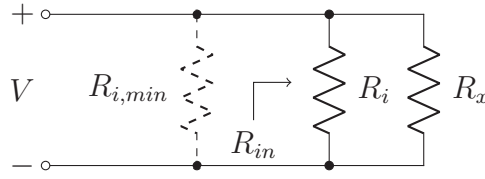


Figure 2.8: Circuit topology based on power gain, after phase compensation of LNW in Figure 2.3.

which in terms of S -parameters is given as

$$G_p = \frac{|S_{21}|^2 (1 - |\Gamma_x|^2)}{|1 - S_{22}\Gamma_x|^2 - |S_{11}(1 - S_{22}\Gamma_x) + S_{12}S_{21}\Gamma_x|^2} \quad (2.5)$$

when the conjugate of (2.3) is substituted into (2.2).

Power gain, calculated in a coupling circuit would tell how high coupling can possibly be achieved since the input is perfectly matched, and any power not delivered to the load is dissipated in the channel. Hence power gain is a good measure of efficiency. It turns out that in a realistic case, high power gain is often accompanied with bandwidth limitations, a high Q -value. Some form of resistance is needed to achieve an acceptable operational bandwidth.

2.3.2 Q -value reduction

In the case of transponder chips, a wired two port measurement of the LNW is difficult, or even impossible to carry out. The obvious reason is the connection interface between the inlay antenna and the transponder chip, which is not a standard interface. Analysis of potential coupling efficiency and internal losses are done with finite element (FEM) software, on which any realizations are based. At a particular frequency, if a value of power gain is available, internal losses may be analyzed by phase compensating the input of the LNW in Figure 2.3 and measuring the input resistance, R_{in} . With reference to Figure 2.8, let the internal losses be represented by a resistance R_i . Since power gain restricts the source resistance to be $R_s = R_{in}$, the power delivered to the load is

$$G_p P_{AVS} = \frac{G_p |V_s|^2}{8R_{in}} = P_{AVS} - \frac{|V_s|^2}{8R_i} = P_{AVS} \left(1 - \frac{R_{in}}{R_i}\right) \iff \frac{1}{R_i} = \frac{1 - G_p}{R_{in}}. \quad (2.6)$$

For a high Q circuit R_i has a high value (parallel topology).

Assume that a back down of delivered power is acceptable to a value denoted $P_{x,min}$, where $G_p \geq P_{x,min}/P_{AVS}$. When increased bandwidth is needed, this back down may be realized by added resistance ($R_{i,min}$) at the input, shown dashed in Figure 2.8, which results in increased bandwidth. The modification of 2.6 then becomes

$$\frac{1}{R_{i,min}} + \frac{1}{R_i} = (1 - G_{p,bd}) \left(\frac{1}{R_{i,min}} + \frac{1}{R_{in}} \right). \quad (2.7)$$

where $G_{p,bd}$ is the new value of power gain, when $R_{i,min}$ is added. From the topology in Figure 2.8

$$\frac{1}{R_{in}} = \frac{1}{R_i} + \frac{1}{R_x}. \quad (2.8)$$

Further, denoting the quotient $G_{p,bd}/G_p$ in dB by $\Delta G_{p,bd}$, (2.6) may be combined with (2.7) to yield

$$R_{i,min} = \frac{R_{in}}{10^{-\Delta G_{p,bd}/10} - 1}. \quad (2.9)$$

Rather high values of back down, such as $\Delta G_{p,bd} = -15$ dB, still result in useful coupling. For such high values, $R_{i,min} \approx R_{in} = Z_s$. Assuming this approximation, the error can be calculated by considering the actual power transfer in terms of transducer gain. It is known from (2.6) that $R_x = R_{in}/G_p$. Further, using (2.9) some algebraic manipulation finally yields

$$G_t = \frac{\frac{4 \cdot 10^{-\Delta G_{p,bd}/10}}{10^{-\Delta G_{p,bd}/10} - 1}}{\left(2 + \frac{1}{10^{-\Delta G_{p,bd}/10} - 1}\right)^2} G_{p,bd}. \quad (2.10)$$

For example, a back down of $\Delta G_{p,bd} = -15$ dB gives $G_t = 0.997G_{p,bd}$, a very small error. Hence it is concluded that the Z_s value adjustment can be done for $R_{i,min}$.

2.3.3 Circle theory

Circle theory for bilinear mappings in the complex plane is a well developed subject and used frequently in this thesis [12, 14]. Properties of passive loads and mismatch are of interest here. A short review of the general theory is given.

A circle of radius r and with center located at a point C in the complex plane can in compact and expanded form, respectively, be described as

$$|z - C| = r \quad |z|^2 - zC^* - z^*C = r^2 - |C|^2. \quad (2.11)$$

A bilinear mapping from the z -plane to the w -plane is of the form

$$w = \frac{az + b}{cz + d} \quad (ad - bc \neq 0). \quad (2.12)$$

Expanding (2.12), with the restriction $|w| = \alpha$, a constant, will lead to the same form as (2.11), in this case with radius and center, respectively given as

$$C = \frac{\alpha^2 c^* d - a^* b}{|a|^2 - \alpha^2 |c|^2} \quad r = \frac{\alpha |ad - bc|}{\left| |a|^2 - \alpha^2 |c|^2 \right|}. \quad (2.13)$$

The circle represented in the w -plane has its center at the origin. In the case when the center is located at a point w_0 the small ruse is used according to

$$w - w_0 = \frac{az + b}{cz + d} \iff w = \frac{(a - cw_0)z + b - dw_0}{cz + d} \quad (2.14)$$

where in this case the old a and b are replaced by $a - cw_0$ and $b - dw_0$, respectively upon which (2.13) may be used. It is concluded that the mapping of one circle, $\{C_a, r_a\}$ in the z -plane, into another, $\{C_b, r_b\}$ in the w -plane, by means of the bilinear mapping (2.12) will be

$$C_a = \frac{r_b^2 c^* d - (a - cC_b)^* (b - dC_b)}{|a - cC_b|^2 - r_b^2 |c|^2} \quad r_a = \frac{r_b |ad - bc|}{\left| |a - cC_b|^2 - r_b^2 |c|^2 \right|} \quad (2.15)$$

2.4 Summary of tool set

The connection methods explained in Section 2.2 along with the quantities covered in Sections 2.3.1–2.3.3 form a complete tool set for the measurement and theory of the topics treated in the remainder of this thesis. A one-port treatment of the the transponder RF front end follows in the next chapter, which in the subsequent chapters is extended to a two-port treatment, when the wireless RNF interface of coupler and inlay interaction is considered.

Chapter 3

Transponder characterization

Probed connection methods towards transponder chips are investigated in Paper A and discussed in Section 2.2, in which the importance of an electrically stable connection, combined with the flexibility of switching between individuals and different size factors, are addressed. With the questions of *how* to measure and how to connect answered, in this chapter follows a two part treatment of *what* to measure, with material taken from Paper B. The first part will be a discussion around non-linearity in general and cautions to be taken, when carrying out measurements with linear vector network analyzers (VNA). In the second part a measurement method will be presented, providing the possibility of measuring complex impedance of RFID transponder chips within a pulse. A figure of merit (FOM) theory is presented and the chapter is concluded with measurement results. Initially, a review is done of reported work in design and characterization of RFID transponders.

3.1 A review of reported work

Most research on RFID transponders reported today concerns the design and characterization of the RF frontend in discrete fixed source environments, rather than considering source impedance as a continuous free variable. The nominal operation of an RFID inlay takes place in such an environment. Hence this is no great surprise.

A distinction of environments, where the source has less or more impact, is well defined by the definition of RNF, propagating near field and far field [15, 16]. Of highest importance for an inlay is the performance of operation in the far field. The design and optimization of transponders is a big research topic [17–20]. Another extensive research topic treats the measurement and characterization of the transponder, by means of wired measurements. The fixed source impedance measurement of linear state transponders, using S -parameters, can be seen as a basic method [21, 22]. Still this is an important measurement, since mismatch performance is of the highest importance at the threshold level, where the transponder is in its linear state. A more advanced method consists of probed measurements of RFID straps with a source-pull system, introducing the concept of shifted source impedance for matching purposes. In another method source impedance shift is introduced by the mutual interaction of antennas [23]. Research on non-linear characterization

with measurements of harmonic content is also reported [24]. A more enhanced non-linear characterization method is the capturing of wave form data [25]. No generalization is possible for a full characterization, but in this case certain fixed topologies need to be considered [26].

Another aspect on transponder characterization is the stimuli. Interrogator functionality, in particular the generation of a wake up signal, can be realized using a vector signal generator, as one exemplary method [27]. Another method is to integrate a commercial interrogator or an RFID tester in the measurement system [21].

The definition of a FOM is an important component in this thesis. One reported method, defining a FOM, takes into consideration not only the forward link in an interrogator and inlay system, but also the reverse link [28]. In other words an S -parameter network is defined, where however de-tuning effects from the inlay antenna on the interrogator antenna is approximated as negligible. Hence the mismatch condition, due to RNF effects is not considered, other than that resulting from load compression.

The concept of arbitrary source impedance in RFID transponder performance evaluation is novel. From the literature study of reported work on the design and characterization of transponders a new field is identified, where an inlay is operated in an RNF environment which strongly deviates from the nominal case. This means that the design is a fixed parameter but knowledge is needed of the performance in the altered environment.

3.2 General non-linear behavior

The operation of an RFID tag in the reactive near field, such as in an RFID enabled printer cavity, is significantly different from far field or even propagating near field conditions [4–6]. The antenna port of an RFID inlay can be regarded as a complex source impedance ($Z_s = R_s + jX_s$) presented towards the RFID transponder. In an altered reactive near field (RNF), such as a printer cavity, this impedance no longer consists of the antenna itself. Rather all objects with electromagnetic interaction surrounding the transponder are included. Hence, the assumption of fixed source impedance will generally not hold [16]. It rather changes continuously when the inlay moves along the media path and is difficult to predict. It may even be regarded as a free variable.

In addition to a shifting source impedance, non-linearity in the transponder is an inevitable component, which cannot be overlooked. Even for relatively low drive levels non-linearity has a strong impact. The mismatch factor (also denoted M) at the interface between the source and a load ($Z_l = R_l + jX_l$) is defined as

$$\tau = \frac{4R_s R_x}{|Z_s + Z_x|^2}. \quad (3.1)$$

In Paper A, the mismatch factor as function of delivered power for two different transponder chips is measured, shown in Figure 3.1. Since impedance data is initially available as function of available power, the available power is first mapped to

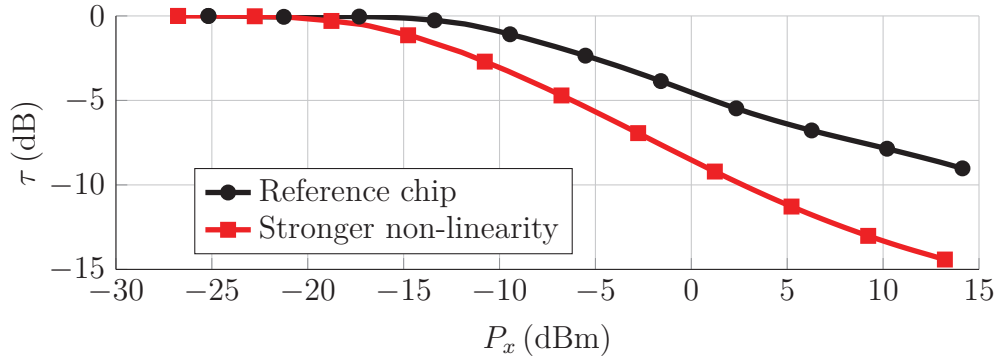


Figure 3.1: Different degrees of non-linearity in impedance.

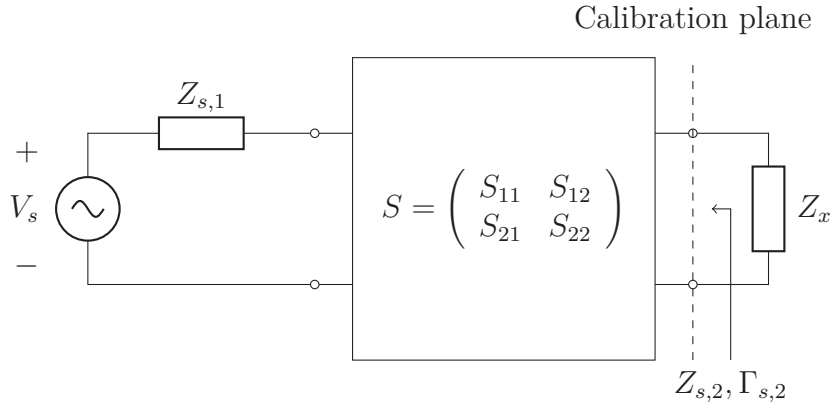


Figure 3.2: Shift of source impedance by means of a two-port transformation.

delivered power as $P_x = \tau P_{AVS}$ and then (3.1) is used. P_x will denote the delivered power to the transponder. Generally, from the definition of available power

$$P_{AVS} = \frac{|V_s|^2}{8\text{Re}\{Z_s\}} \quad (3.2)$$

a set of available power values in one impedance system can be mapped to an equivalent set of available power values in a different impedance system, given as

$$P_{AVS,2}(\text{dBm}) = P_{AVS,1}(\text{dBm}) + 10 \log_{10} \left(\frac{\text{Re}\{Z_{s,1}\}}{\text{Re}\{Z_{s,2}\}} \right). \quad (3.3)$$

If a shift in source impedance is represented by a two-port transformation, as shown in Figure 3.2, the S -parameters are added to the equation. In this case, consider the source impedance $Z_{s,2}$ as seen at the output of the two-port. It is given as [12]

$$Z_{s,2} = Z_0 \frac{1 + \Gamma_{s,2}}{1 - \Gamma_{s,2}} \quad \Gamma_{s,2} = S_{22} + \frac{S_{12}S_{21}\Gamma_{s,1}}{1 - S_{11}\Gamma_{s,1}} \quad \Gamma_{s,1} = \frac{Z_{s,1} - Z_0}{Z_{s,1} + Z_0}. \quad (3.4)$$

The following load-pull, or more specifically source-pull, analysis is of a more theoretical nature. Instead of using a discrete set of source impedance values, in the measurement of load impedance with a VNA, the source impedance is treated as a continuous variable and measured load impedance is considered as function of

delivered power. The mismatch will tell how optimized the power transfer to the transponder is. However, no external optimization for power transfer, by shift of source impedance, is considered, as in the case of transistor source-pull. Performance is rather based on non-linearity impact on mismatch. The arbitrary source impedance is represented by a function average over a certain continuous region in the Smith chart. The key point, and difference to conventional source-pull analysis, is the non-existing knowledge of source impedance. The detailed definitions for this analysis are presented in Section 3.5.

From the RFID perspective, adding a source with free variable impedance puts entirely new conditions on the characterization and performance evaluation of transponders, as compared to the conventional design process of the inlay antenna and transponder RF frontend for the application in far field, or propagating near field. Two environmental facts have been identified: A varying source impedance and non-linearity. What has been established so far is the equivalence between shifted source impedance and mismatch, when referring to the measured impedance as function of delivered power. A straight forward analysis can be performed of how the mismatch factor varies for different source impedances. But is it really this straight forward? The answer is in general, no. A hidden problem is the non-linearity, arriving at the following statement:

The measured impedance at the fundamental frequency, as referenced to a single tone excitation of a non-linear device, depends on the source impedance for any fixed delivered power.

This statement needs some elaboration. To this end consider two cases in measuring the complex impedance of a highly reactive load being in its linear state. This could be done for instance with a linear vector network analyzer (VNA). In the first case let a calibration be done in the standard Z_0 system. In the latter case let a lossless and reciprocal two-port be inserted, matching the load to 50Ω , and then perform a calibration at the output of the two-port. The situation is illustrated in Figure. 3.3. The calibration at the output of the two-port matching network is not recommended and also not considered in practice. It only serves as a theoretic example. Neglecting any inaccuracies, measurement of the linear state impedance in both cases would yield the same result. However, as soon as the drive level is increased to the non-linear state two different results are obtained, even for the same delivered power. The reason is that the voltage/current time domain solutions for the load in the two cases are different, since the source impedance is part of the equation. Or, from a frequency domain perspective harmonics resulting from the non-linearity will add components at the fundamental frequency. Clearly, the equivalent source impedance, as presented at the output of the two-port in the second case, is different (conjugate of device impedance in the linear state) as compared to the first case (Z_0 -system). Consequently, the extracted fundamental Fourier coefficients are different in the two cases, yielding different values of impedance. Note that different complex values of voltage and current can still result in the same delivered power. The fundamental question that comes to mind is what is actually measured.

Note that the phenomena of different measured impedance values in the two cases occurs, despite the fact that calibrations have been carried out. It is concluded

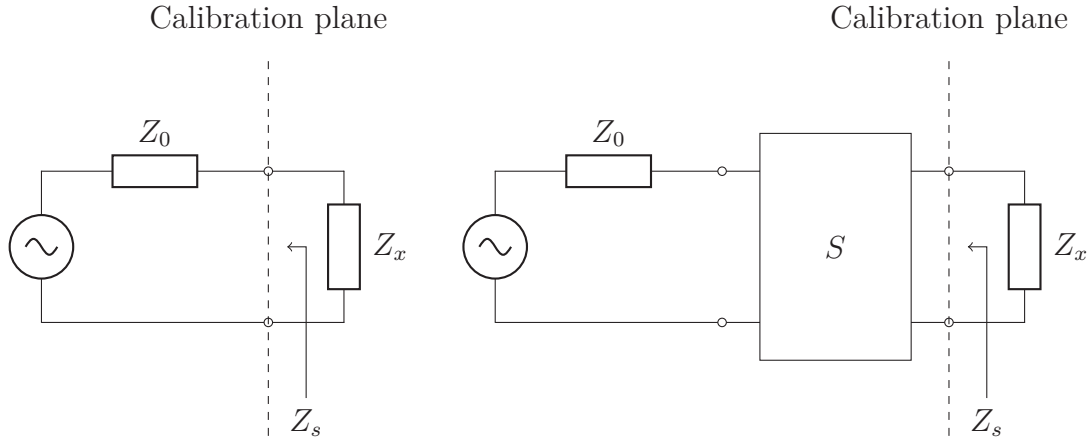


Figure 3.3: Shifted source impedance impact on the measured impedance of a non-linear load.

from this example, that it is important to know the physical environment that the non-linear device is connected to. Any calibration will not change this environment, since this is a calculated correction yielding correct results for linear devices only. The physical environment, or in other words the presented source impedance, would be obtained by measuring the output impedance of the VNA with for instance another calibrated VNA. Fortunately, the output return loss of a VNA is rather high. Furthermore, any embedding network can be separately characterized. If these conditions are fulfilled, useful results in non-linear characterization may be obtained with a linear VNA, as to the point of knowing what is actually measured. Still the question remains how meaningful measurements of non-linear devices with a linear VNA can be carried out when the source impedance is considered to be a variable quantity.

As a comparison, in source-pull analysis of a transistor, in general iteration of source impedance is needed for optimized power transfer, and there is also a need of terminations at the harmonic frequencies. In the case of an RFID transponder, the termination at harmonic frequencies is not considered, from a claimed approximation treated in the next section.

3.3 The approximation

After discussing the general behavior of a non-linearity, now consider the restriction where a fixed delivered power yields the same measured impedance, independent of source impedance. The treatment will then be limited to a certain type of devices and cannot be generalized further. In this case the RF frontend of RFID transponders is considered.

Two main observations in the measurement of RFID transponders are discussed in Paper B. These are first the drastic change from a linear state (fixed measured impedance) to the non-linear state (impedance path traced out in the Smith chart) during a sweep of source power. This suggests a close to ideal clipping behavior from a limiter. The subject of ideal strong non-linearity, in the case of transistors, is

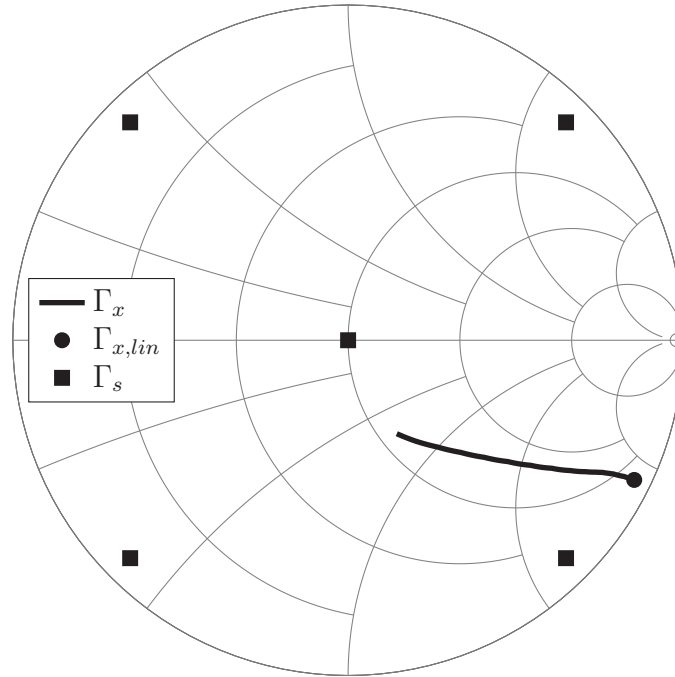


Figure 3.4: An example of the measured impedance versus swept source power.

exploited in literature [29]. Secondly, the measured impedance as function of delivered power remains unchanged when compared for two different source impedances. A further observation is the shift towards a lower imaginary part in the non-linear state, as seen in Figure 3.4.

The Smith chart is intuitive in explaining the independency of load impedance on source impedance for fixed delivered power conditions. The square markers in Figure 3.4 indicate different choices of source impedance, some of them towards extreme values. Assume the illustrated non-linear impedance trace, when initially measured in a 50Ω system (center point source impedance). Every point along the trace corresponds to some delivered power. Provided that the available powers of the other source points are adjusted in such way, as to deliver the same delivered power, the claimed approximation will hold when the impedance trace remains unchanged.

3.4 Verification of source independency

To verify the validity of the approximation a transponder impedance as function of delivered power, being independent of the source environment, two distinct source impedances are chosen in a measurement. It shall be emphasized that the approximation is based on only two distinct values of source impedance, the unmatched 100Ω system and the close to conjugate match, with details found in Paper B. No attempt of rigorous modelling is made here, but rather to explain common behavior among RFID transponder chips. Modeling and design of specific transponder RF frontends is an extensive research topic [17–19, 30, 31]. However, as

Table 3.1: Maximum unmatched to unmatched impedance deviation.
Re: Real Part. Im: Imaginary Part.

Type	$\max(\Delta(Z_{xL}))$ (Ω)	P_{xL} (dBm)	$P_{xL,min}$ (dBm)	$P_{xL,max}$ (dBm)
A	12 (Im)	10	-21	10
B	-11 (Im)	10	-27	10
C	-13 (Im)	-14	-28	10
D	-15 (Im)	-5	-28	8
E	15 (Re)	7	-34	9
F	-23 (Im)	8	-33	8

Table 3.2: Maximum unmatched to matched impedance variance.
Re: Real Part. Im: Imaginary Part.

Type	$\max(\text{Var}(Z_{xL}))$ (Ω^2)	P_{xL} (dBm)	$P_{xL,min}$ (dBm)	$P_{xL,max}$ (dBm)
A	42 (Re)	-2	-21	10
B	2 (Re)	10	-27	10
C	5 (Im)	-19	-28	10
D	25 (Im)	-25	-28	8
E	50 (Im)	-16	-34	9
F	5 (Im)	-31	-33	8

of today no measured knowledge based on a larger set of source impedances exists. A general theoretical treatment on non-linearity and related mathematical concepts are found in the textbooks by Maas, Abramowitz and Cripps [29, 32, 33].

In the verification method presented here, the delivered power is calculated from knowledge of the source impedance. Data is taken from the power swept impedance measurement of the transponder at low impedance state (index L). Six different transponder types, labeled Type A–F are considered. The results will partly tell how the unmatched to matched condition deviation develops along delivered power, partly give information on the individual variation. A summary of maximum unmatched to matched impedance deviation and variance is given in Table 3.1 and Table 3.2, respectively.

A general expectation is that the approximation of impedance independency on delivered power loses validity for high power levels. The highest impedance deviation is seen for Type F and the same behaviour is also seen for Type A, B and E from the values in Table 3.1. No particular trend could be seen over delivered power for

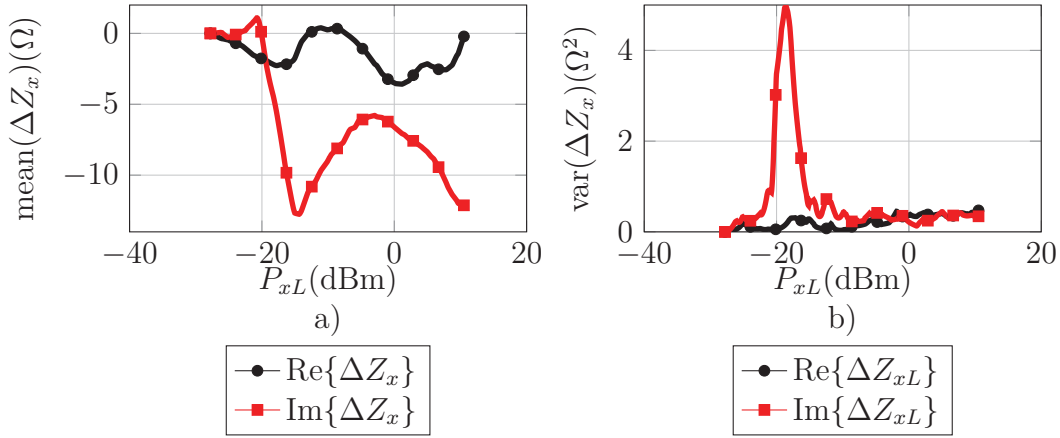


Figure 3.5: Source shift impact Type C. $Z_S = 100 \Omega$ and $Z_S = 92 + j164 \Omega$.
a) Mean deviation. b) Variance.

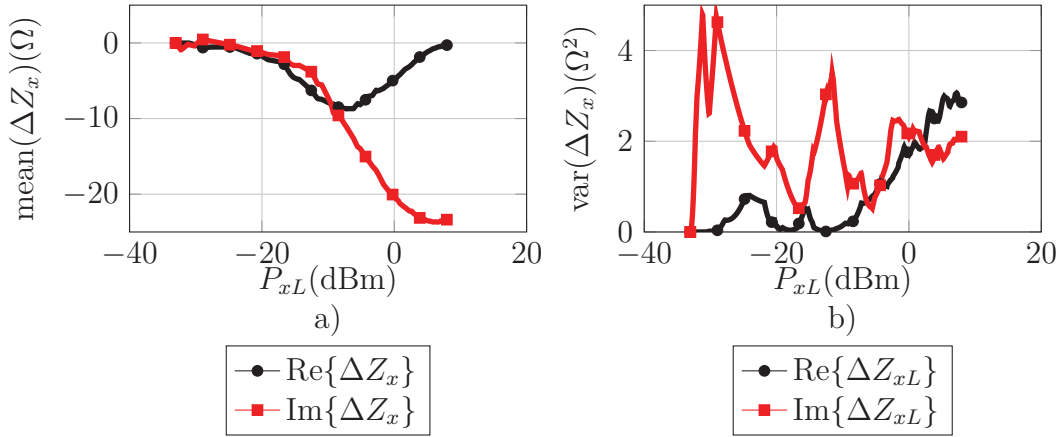


Figure 3.6: Source shift impact Type F. $Z_S = 100 \Omega$ and $Z_S = 92 + j164 \Omega$.
a) Mean deviation. b) Variance.

Type C and Type D. Power swept data for Type C and F are plotted for comparison in Figures 3.5 and 3.6, respectively. For deviation between unmatched and matched state along power, the left hand plots are considered. For individual variation, the right hands plots are considered. Further information on power swept data for the remaining types are found in Paper B.

Generally, the levels within the first 10 dB after transponder activation are considered to be within acceptable limits for all types. This is about -20 to -15 dBm of delivered power, depending on transponder type. Relatively speaking, for Type C and Type D, the deviation is small in imaginary part, since the reactance has its highest values in this power interval.

From a real life testing perspective rather the low end of the power interval, above threshold of activation, is of interest. The conclusion is that the approximation of source impedance independency holds. It is also concluded that averaging will give a good representative for the calculation of FOM, treated in the next section.

3.5 Figure of merit calculation

After the discussion in Sections 3.2-3.4, the central assumption arrived at is:

The measured impedance at the fundamental frequency, for a fixed delivered power, is independent of the source impedance.

Based on this assumption, in Paper B mismatch theory is used to provide a tool set, from which a FOM can be derived. The theory is developed in the next subsections.

3.5.1 Mismatch theory for source impedance shift

The delivered power to the transponder is given as

$$P_{xL} = MP_{AVS} = \frac{4R_s R_{xL}}{|Z_s + Z_{xL}|^2} P_{AVS} = \frac{(1 - |\Gamma_s|^2)(1 - |\Gamma_{xL}|^2)}{|1 - \Gamma_s \Gamma_{xL}|^2} P_{AVS} \quad (3.5)$$

where (3.1) is used, which is expressed in terms of reflection coefficients [12]. Here Γ_s and Γ_{xL} are the source and transponder reflection coefficients, respectively. The conversion between impedance and reflection coefficient is

$$\Gamma_s = \frac{Z_s - Z_0}{Z_s + Z_0} \quad \Gamma_{xL} = \frac{Z_{xL} - Z_0}{Z_{xL} + Z_0}. \quad (3.6)$$

The index L has been added since, in general, the pulsed low state impedance is considered. The modulation and RFID protocol are described in Appendix A.

Consider now the mismatch in (3.5), as referred to the Γ_s -plane, where M is a constant. The expression for M can be rearranged into the equation for a circle in the Γ_s -plane for constant M , see 2.11 in Section 2.3.3. The Γ_s -values yielding a constant mismatch factor M for a fixed Γ_{xL} are found on a circle with center C_M and radius r_M , respectively given as

$$C_M = \frac{M\Gamma_{xL}^*}{1 - (1 - M)|\Gamma_{xL}|^2} \quad r_M = \frac{\sqrt{1 - M}(1 - |\Gamma_{xL}|^2)}{1 - (1 - M)|\Gamma_{xL}|^2}. \quad (3.7)$$

The terms impedance and reflection coefficients will be used interchangeably for Γ and Z , respectively. The power swept non-linear impedance path, as discussed in Section 3.3, is now complemented with its conjugate for reference to source impedance, shown in Figure 3.7. The power sweep starts at threshold of backscatter modulation ($\Gamma_{xL,th}^*$, $P_{xL,th}$), indicated by the circle marker located at the outer rim of the Smith chart. An offset point ($\Gamma_{xL,offset}^*$, $P_{xL,offset}$) along the power sweep is indicated by the square marker. Note that since a non-linearity is considered the impedance is only valid for a certain delivered power, therefore mentioned explicitly. Further an arbitrarily chosen source impedance, denoted Γ_s , is indicated by the asterisk.

Let $\{M, \Gamma_{xL}\}$ in (3.7) be replaced by $\{M_{L,th}, \Gamma_{xL,th}\}$ and $\{M_{L,offset}, \Gamma_{xL,offset}\}$, respectively representing the threshold and offset case. The corresponding mismatch circles are also plotted in Figure 3.7. The solid circle illustrates the mismatch between

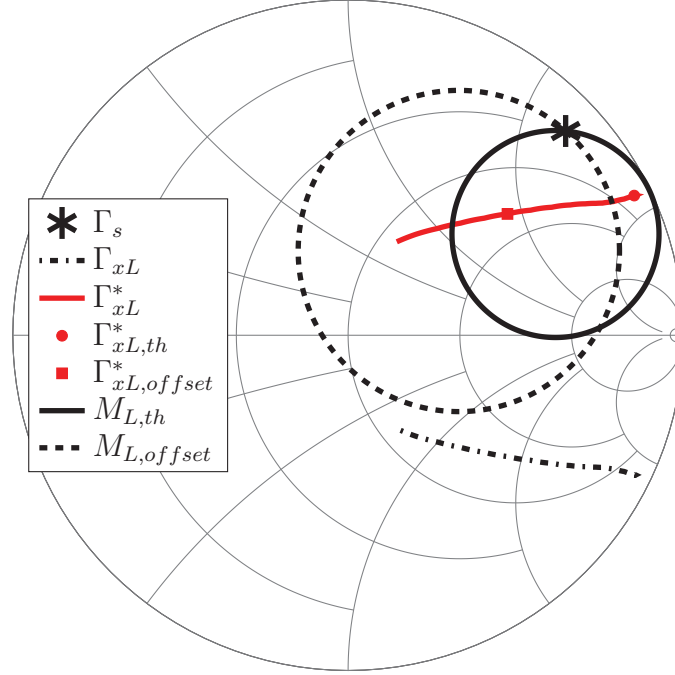


Figure 3.7: Mismatch circles for a non-linear load excited by a source (asterisk). Solid circle: Threshold mismatch. Dashed circle: Offset mismatch.

source Γ_s and load $\Gamma_{xL,th}$. The dashed circle illustrates the mismatch between source Γ_s and load $\Gamma_{xL,offset}$. It is clear that the mismatch values, generally, are different in the two cases. For a linear load these two circles would align.

The mismatch quotient, denoted k_M , is defined as

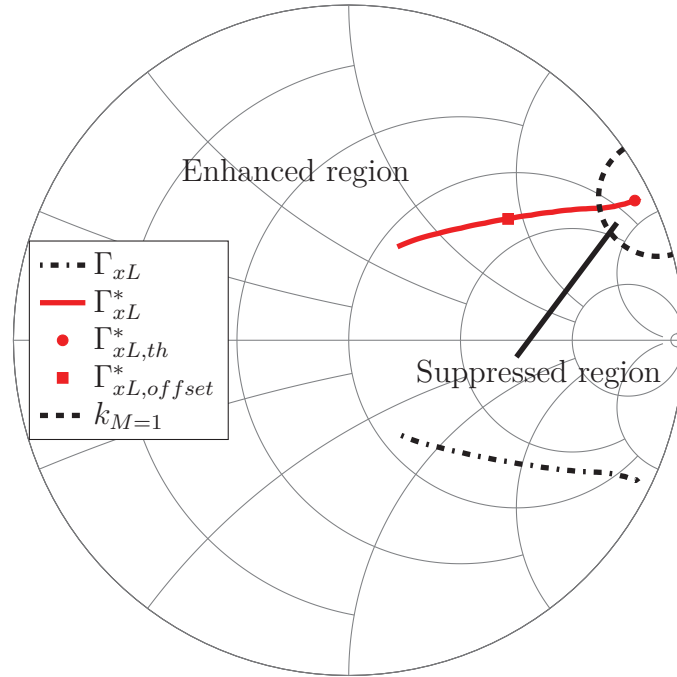
$$k_M \equiv \frac{M_{L,offset}}{M_{L,th}} = \frac{(1 - |\Gamma_{xL,offset}|^2) |1 - \Gamma_s \Gamma_{xL,th}|^2}{(1 - |\Gamma_{xL,th}|^2) |1 - \Gamma_s \Gamma_{xL,offset}|^2}. \quad (3.8)$$

It indicates the non-linear impact on the available power ratio between threshold and offset state. For a linear load $k_M = 1$ and k_M will be bounded when $|\Gamma_{xL,th}| < 1$, $|\Gamma_{xL,offset}| < 1$ and $|\Gamma_s| \leq 1$. Depending on where in the Smith chart the source is located, k_M can have values both below and above unity for a non-linear load. If k_M is constrained to unity, manipulation of (3.8) yields

$$\left| \frac{\Gamma_{xL,th} \Gamma_s - 1}{\Gamma_{xL,offset} \Gamma_s - 1} \right| = \sqrt{\frac{1 - |\Gamma_{xL,th}|^2}{1 - |\Gamma_{xL,offset}|^2}} \quad (3.9)$$

which is recognized as a bilinear mapping yielding a circle in the Γ_s -plane, as shown dashed in Fig. 3.8. Using the notations in Section 2.3.3, the center and radius are given as

$$C_{k_M=1} = \frac{\alpha^2 c^* d - a^* b}{|a|^2 - \alpha^2 |c|^2} \quad r_{k_M=1} = \frac{\alpha |ad - bc|}{\left| |a|^2 - \alpha^2 |c|^2 \right|} \quad (3.10)$$

Figure 3.8: Unity mismatch quotient circle ($k_M = 1$) drawn dashed.

where the terms are identified as

$$\begin{aligned}
 a &= \Gamma_{xL,th} & b &= -1 & c &= \Gamma_{xL,offset} & d &= -1 \\
 \alpha &= \sqrt{\frac{1 - |\Gamma_{xL,th}|^2}{1 - |\Gamma_{xL,offset}|^2}}.
 \end{aligned} \tag{3.11}$$

The circle boundary will divide the Smith chart into two distinct regions, where Γ_s can reside. The region where $k_M < 1$ will be called the suppressed region, denoted Ω_s . In Ω_s the mismatch condition yields a non-linear growth of available power for increased delivered power, as compared to the linear case. Correspondingly, the region where $k_M > 1$ will be called the enhanced region, denoted Ω_e . In Ω_e the non-linearity yields a reduction in needed offset available power for increased delivered power, as compared to the linear case. In other words, the load is pushed towards a better mismatch condition.

3.5.2 The $|\Delta\Gamma|$ -value

The mismatch theory developed in the previous section is suitable for measured data taken from a linear VNA. One more quantity, needed for the definition of FOM, is the $|\Delta\Gamma|$ -value. The communication between the transponder is half duplex, meaning that the broadcast from the interrogator is followed by a reply from the targeted transponder, in that particular order. The communication can never occur simultaneously (full duplex). The response from the transponder is based on modulation of the input impedance at the RF frontend. The modulation consists of the shift between two distinct values, low and high state. The low state is equivalent

to the absorbing or scavenging mode. The high state is basically a drastic shift of the impedance imaginary part. An example of the pulsed impedance, measured by the VNA in pulse profile mode, is shown in Figure 3.9.

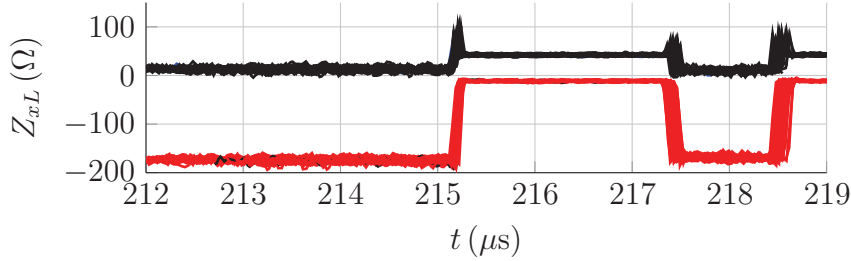


Figure 3.9: Overlaid sweep samples of the pulsed impedance, as measured by the VNA.

Based on the pulsed impedance data, the magnitude of the difference in reflection coefficient between high and low state can be calculated. Accordingly, it is defined as [34]

$$|\Delta\Gamma| \equiv \left| \frac{Z_{xH} - Z_s^*}{Z_{xH} + Z_s} - \frac{Z_{xL} - Z_s^*}{Z_{xL} + Z_s} \right|. \quad (3.12)$$

The $|\Delta\Gamma|$ -value is bounded for all possible values of source impedance, with a maximum value of $|\Delta\Gamma| = 2$ when the state switches between 0 and ∞ . This is very important for the definition of FOM.

3.5.3 Figure of merit

The quantities for the definition of FOM have been derived. These are the mismatch quotient k_M from (3.8) and the $|\Delta\Gamma|$ -value from (3.12). Clearly, both these quantities, depend on the source impedance and are well defined functions over the entire Smith chart. The idea is now to define a FOM-function operating on the Smith chart, comparing the threshold state with the offset state. From the previous mismatch theory it was concluded that the suppressed region, defined by the unity mismatch quotient condition, contains the source impedance values where the mismatch condition yields a non-linear growth of available power for increased delivered power, as compared to the linear case. For stronger non-linearities k_M decreases.

An increase in the $|\Delta\Gamma|$ -value yields a higher quality in backscatter response from the transponder. Taking both the threshold and offset value into account, the obvious choice would be to take the product. The quotient, for instance $|\Delta\Gamma_{offset}/\Delta\Gamma_{th}|^2$, would be undefined for $|\Delta\Gamma| = 0$, which is true if $Z_{xL} \approx Z_{xH}$, or $Z_s \rightarrow \infty$. The FOM function is now composed as

$$f_{FOM}(\Delta P, r, \varphi) = |\Delta\Gamma_{th}(\Delta P, r, \varphi) \Delta\Gamma_{offset}(\Delta P, r, \varphi)|^2 k_M(\Delta P, r, \varphi) \quad (3.13)$$

where $P_{xL,offset} = P_{xL,th} + \Delta P$. (r, φ) are the polar coordinates, i.e., $\Gamma_s = r e^{j\varphi}$. f_{FOM} expresses an estimate on offset flexibility, i.e., the strength of non-linearity, weighted by the strength of backscatter modulation. Different alternatives are possible for

comparison, by setting one or several of the quantities $\Delta\Gamma_{th}$, $\Delta\Gamma_{offset}$ or k_M to unity. Only the suppressed region (Ω_s) is considered, where an increased value of both k_M and $|\Delta\Gamma|$ indicates a better performance.

For an estimate on the entire region, the final FOM is calculated as the function average according to

$$I_{FOM}(\Delta P) = \frac{1}{A} \int_{\varphi_1}^{\varphi_2} \int_{r_1}^1 f_{FOM}(\Delta P, r, \varphi) r dr d\varphi \quad (3.14)$$

where A is the area of the region of integration. Since f_{FOM} is bounded on the entire region of integration, it is valid. The boundary of integration is given by the intersection between the unity mismatch quotient circle (3.10)–(3.11) and the Smith chart. Denote the intersection points $z_{is1,2} = (x \mp jy) e^{j \arg(C_{k_M=1})}$, which from the circle definition give the set of equations

$$\begin{aligned} x^2 + y^2 &= 1 \\ (x - |C_{k_M=1}|)^2 + y^2 &= r_{k_M=1}^2. \end{aligned} \quad (3.15)$$

Manipulation and solving for (x, y) yields

$$\begin{aligned} z_{is1,2} &= \left(\frac{|C_{k_M=1}|^2 - r_{k_M=1}^2 + 1}{2|C_{k_M=1}|} \right. \\ &\quad \left. \mp j \frac{\sqrt{4|C_{k_M=1}|^2 - (|C_{k_M=1}|^2 - r_{k_M=1}^2 + 1)^2}}{2|C_{k_M=1}|} \right) \\ &\quad \times e^{j \arg(C_{k_M=1})} \end{aligned} \quad (3.16)$$

where the boundary is given by

$$\begin{aligned} \varphi_1 &= \arg z_{is1} \leq \varphi \leq \arg z_{is2} = \varphi_2 \\ r_1 &= |C_{k_M=1} + r_{k_M=1} e^{j\theta}| \leq r \leq 1 \\ \theta &= \pi + \varphi + \arcsin \left(\frac{|C_{k_M=1}|}{r_{k_M=1}} \sin(\arg(C_{k_M=1}) - \varphi) \right). \end{aligned} \quad (3.17)$$

In summary the described procedure will give an estimate on mismatch roughness under a changed source environment from the conjugate state, when the delivered power needs to be adjusted to a higher value. In other words the FOM will tell how flexible the transponder response is to a shifted source impedance. It also takes into account backscatter modulation, by including the $|\Delta\Gamma|$ -value. The offset point may represent a state of higher delivered power for added functionality in the transponder, in particular, when writing to the transponder memory, as compared to only reading from it. Higher power levels are needed for writing and hence the FOM becomes a critical performance parameter in an altered reactive near field surrounding the RFID tag, leading to a shift in source impedance.

3.6 Measurement system

The core implementation of the measurement system is the mimicking of the RFID wake-up signal, as described in Section A.2, combined with the electrical measurement of complex impedance within a pulse of the back scattered reply from the transponder. The realization of such a setup may be done in many different ways. One alternative is to use a vector signal generator with the VNA and external pulse modulators, which are directly connected to the VNA [27].

After inventory of the different possibilities it was found that the many options available in instruments provided by Rohde & Schwarz[®] (R&S) would enable a compact setup, consisting of only two instruments [35]. These are the ZVA (VNA) and ZVAX extension unit (EU). The big memory available for long recording times enables the entire wake-up signal to be generated as one single pulse profile, including the back scatter response from the transponder. A graphical user interface (GUI), see Appendix B, is programmed for communication between the instruments and MATLAB on the PC host, by means of SCPI commands over a GPIB connection [36]. Virtually, all commands controlling the instruments are accessible. When the ZVA and ZVAX are connected together they present a common programming interface towards MATLAB.

A bench diagram of the complete setup is shown in Figure 3.10. The purpose of the EU is to add extra components into the RF path. This is possible from the direct access at the VNA ports. The EU contains several paths, with harmonic filters, pulse modulators and combiners. The application in Paper B only uses the pulse modulator for one port. The possibility of differential pulse modulation is investigated, but unsuccessful to implement. However, for unmodulated measurements of transponder impedance the true differential mode (TDM) option in the VNA is used. The characterized transponder chips are from different vendors, with several individuals of each, where the device under test (DUT) connection methods described in Section 2.2.1 are used. Tuners from Maury Microwave are inserted between the VNA ports and the probe connection, in order to shift the source impedance presented towards the transponder [37].

In summary the setup enables the following measurement combinations:

- Single ended (one-port) unmodulated impedance without source shift
- Differential (two-port) unmodulated impedance without source shift
- Single ended (one-port) unmodulated impedance with source shift
- Differential (two-port) unmodulated impedance with source shift
- Single ended (one-port) modulated impedance without source shift
- Single ended (one-port) modulated impedance with source shift

Despite the possibilities listed the source shift is done single ended for an approximate conjugate match of the transponder RF frontend, which is highly reactive.

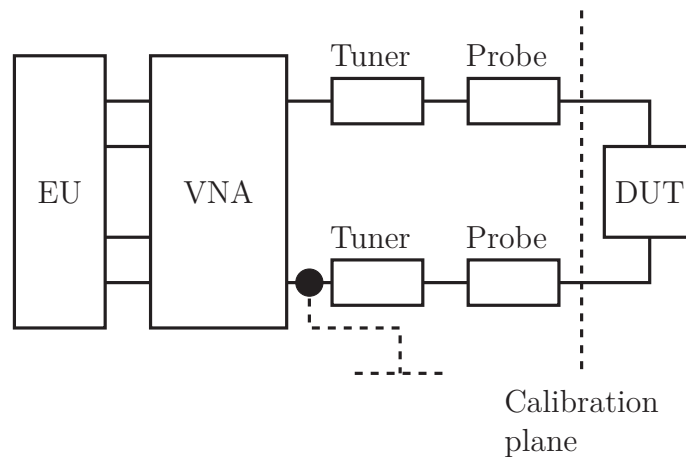
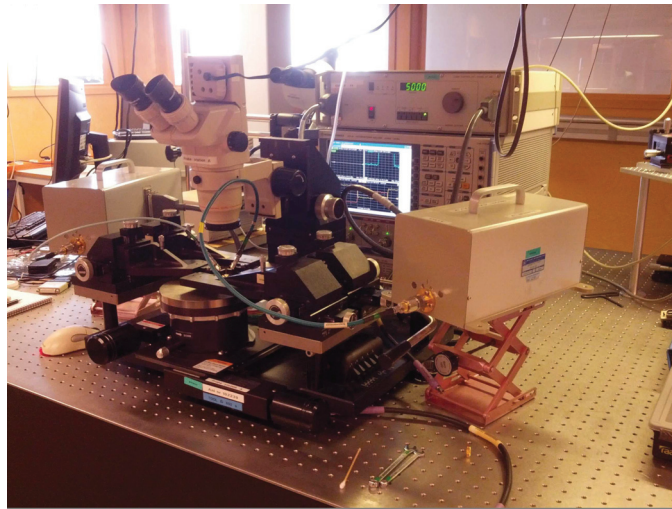


Figure 3.10: Top: Measurement system including ZVA24, ZVAX, probe station, and tuners with control box. Bottom: Bench diagram. The calibration plane is valid when the tuners are set to $50\ \Omega$ only. For source shift pre-characterization with de-embedding is done.

This was accomplished by short circuiting one of the tuners, which is indicated by the dashed ground connection in Figure 3.10.

The frequency characteristics of the transponder chip are rather broadband over the UHF RFID band [2] and the same pulsed behaviour is expected across the band so a modulation frequency in the middle of the band at 915 MHz is chosen. This frequency was also chosen for the matched measurement. A frequency sweep is only performed for the unmodulated unmatched condition in TDM.

3.7 Measured FOM

3.7.1 Averaging

The measured transponder types, Type A–F, with 5 individuals of each, form a test matrix as explained in Section 2.2.1. Type A–C are from the same vendor, but

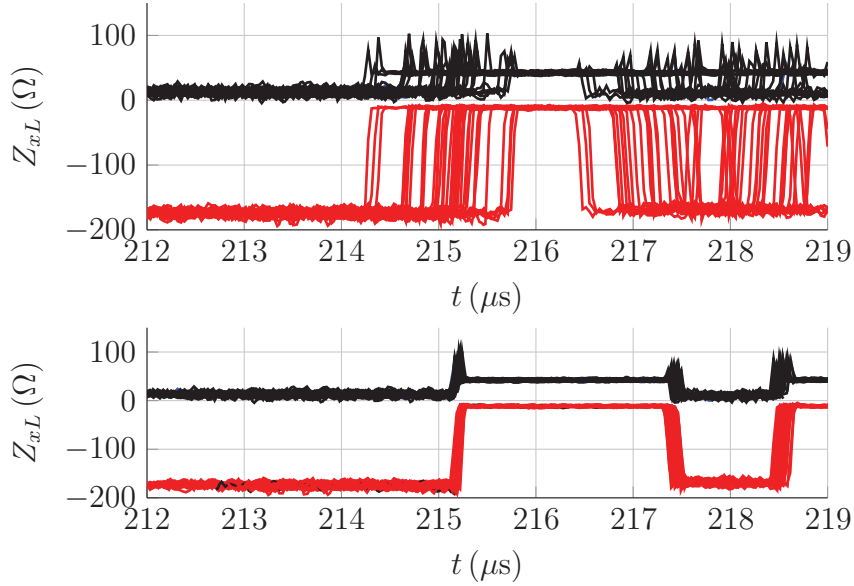


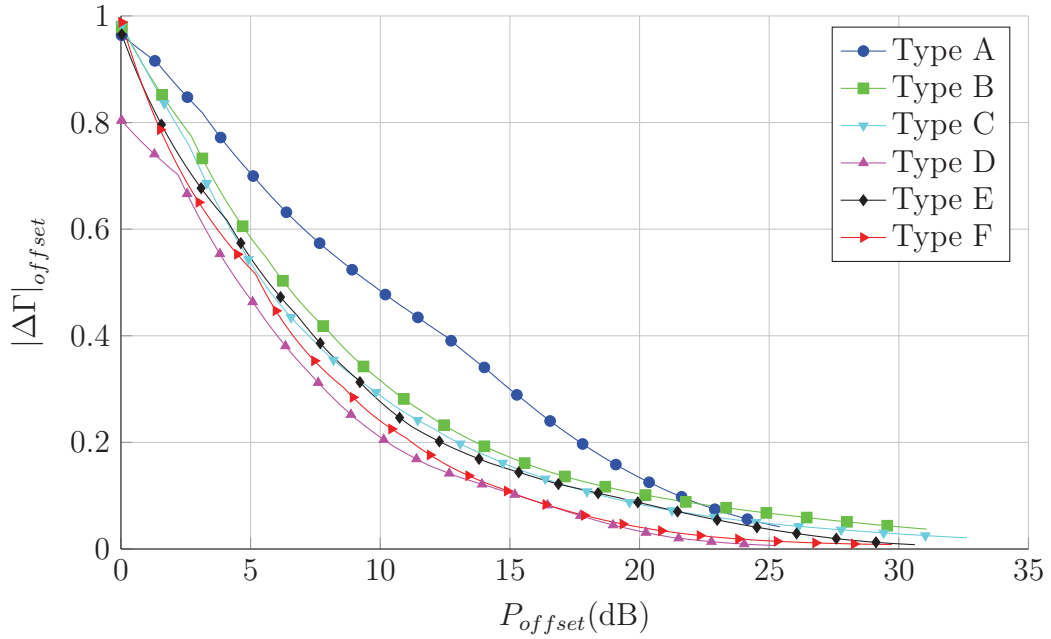
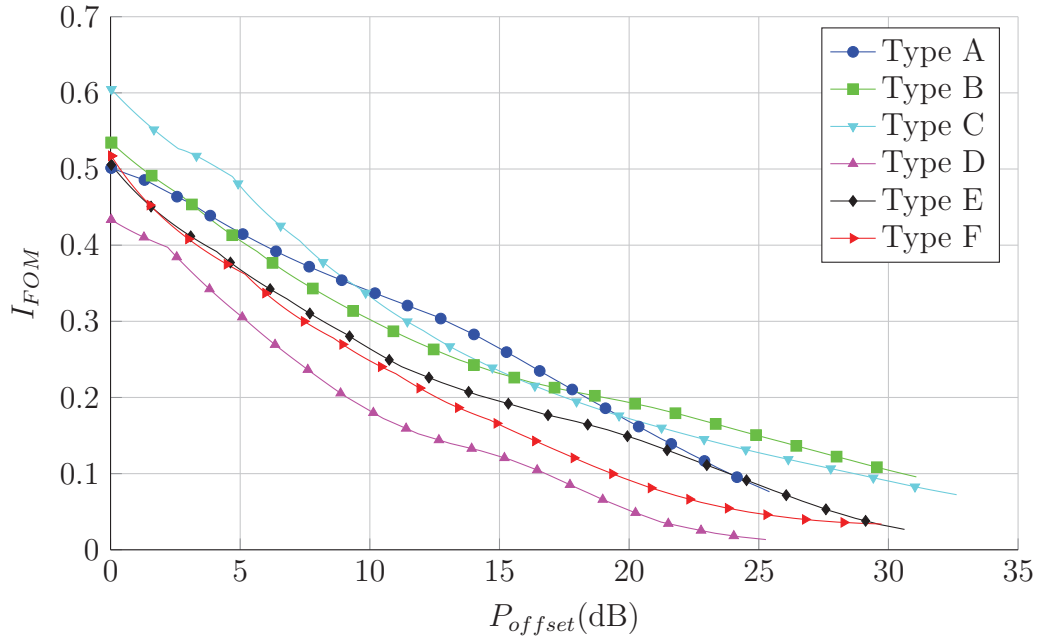
Figure 3.11: Sweep and sample sorting of pulse profile. Top: Before sorting. Bottom: After sorting. Impedance real and imaginary parts are distinguished being strictly positive and negative, respectively.

of different versions. The same holds for Type D and Type E. From repeatability measurements over individuals, with mean and variance calculation, it is concluded that an average over individuals is a good representative for the real life sample and is being used in the FOM evaluation. More details on the repeatability measurements are found in Paper B. It is explained in Appendix A.3 that the commands included in the VNA pulse profile and backscatter response from the transponder define a single sweep. The wake up sequence and time window for response detection is cycled periodically. Since the delay between trigger and response is random for each sweep, a post processing of the data is required to enable averaging. It basically consists of adding time offsets to the backscatter response sweeps, illustrated in Figure 3.11. After sorting an average can be calculated for the low and high pulse state. High state is defined as the high value of the imaginary part (negative values), i.e., after the switch from the absorbing state (low state) to a close to zero value. A sorting algorithm has been implemented and available as one of the features in the post analysis GUI. The algorithm is described in the Appendix B.

3.7.2 FOM results

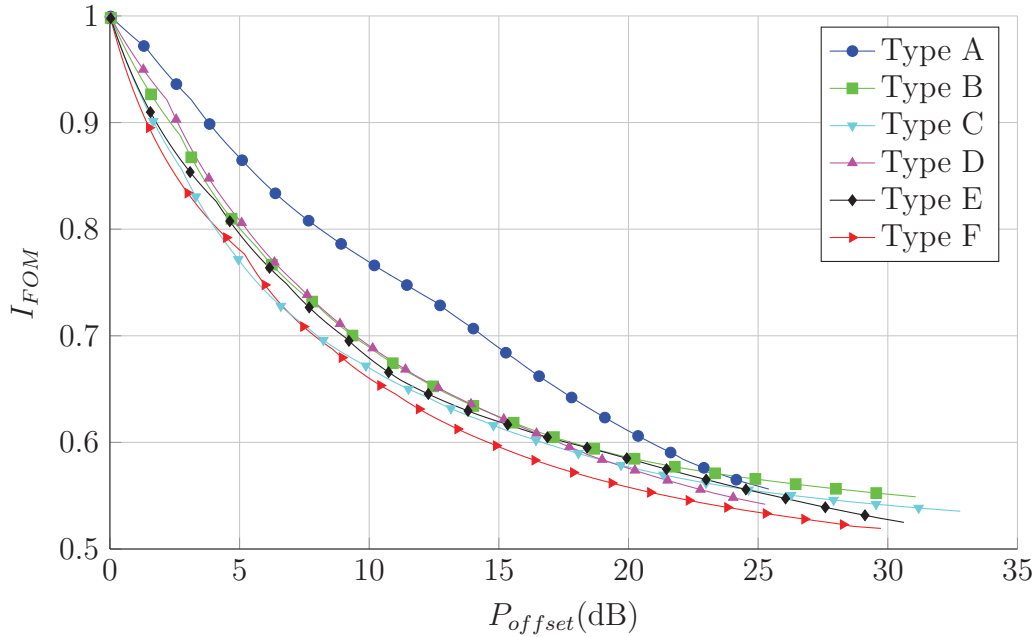
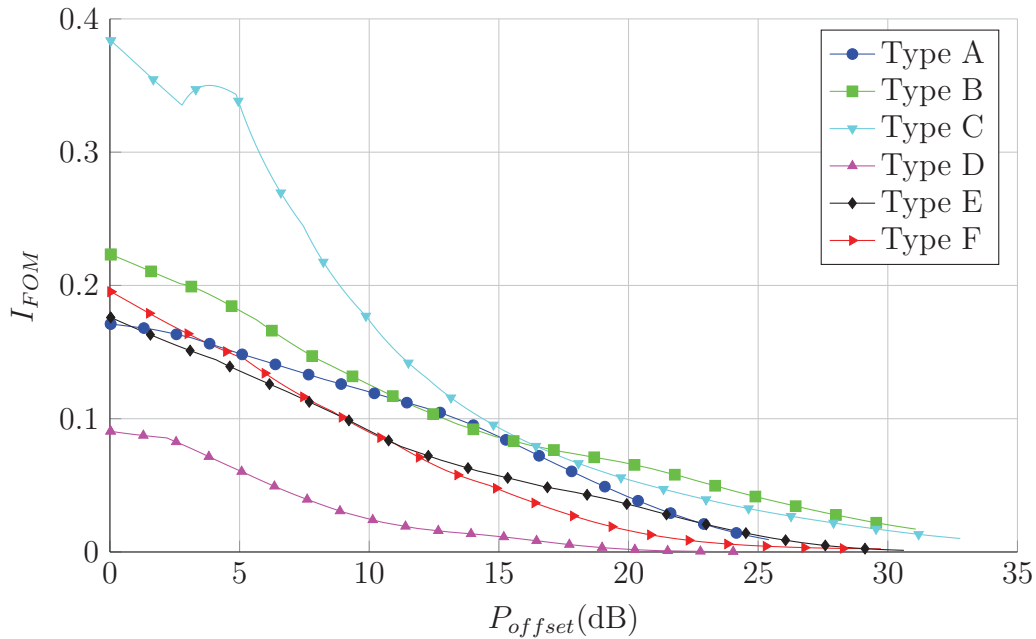
In the calculation of FOM, both the mismatch quotient k_M and the $|\Delta\Gamma|$ -value, as defined in Section 3.5.1–3.5.2, are taken into account. The power sweep consists of an offset of delivered power from the threshold of response. The $|\Delta\Gamma|$ -value and k_M are first treated separately and then combined for the final FOM.

Initially, the $|\Delta\Gamma|$ -value is calculated over swept offset of delivered power, when the source impedance is fixed to a conjugate of the measured impedance at threshold ($\Gamma_{xL,th}^*$), shown in Figure 3.12, which represents the far field case with an antenna conjugately matched to the transponder. This situation is not commonly found

Figure 3.12: Power sweep of $|\Delta\Gamma|$ for fixed source impedance $\Gamma_s = \Gamma_{xL,th}^*$.Figure 3.13: Power sweep of $|\Delta\Gamma|$ as function average.

inside an RFID printer, but the results give useful information of the performance in an RFID system. From the results Type A supersedes the remaining types, where Type D, an older chip version has the lowest maximum, i.e., in the vicinity of threshold response. The remaining types show similar performance.

Next, the $|\Delta\Gamma|$ -value is considered as function average over the suppressed region, with $f_{FOM} = |\Delta\Gamma_{offset}|$ and $|\Delta\Gamma_{th}| = k_M = 1$ in (3.13). This case represents the situation when the source Γ_s is located anywhere in the suppressed regions, as compared to the fixed case illustrated in Figure 3.12. It is plotted in Figure 3.13. A

Figure 3.14: FOM sweep without $\Delta\Gamma$.Figure 3.15: FOM sweep with $\Delta\Gamma$.

more conservative value of the maximum value is now seen. Type D also has a more significant lower $|\Delta\Gamma|$ -value over the power sweep.

Finally, I_{FOM} is calculated without and with weighting of $|\Delta\Gamma|$, respectively, shown in Figures 3.14 and 3.15. The results without $|\Delta\Gamma|$ in Figure 3.14 are similar to the fixed source impedance case in Figure 3.12, but it is seen how the mismatch condition for Type D is moved to better performance.

The results in Figure 3.15, including both $|\Delta\Gamma|$ and k_M , are interesting. It can be observed that $|\Delta\Gamma|$ and k_M interact to give bigger differences in performance between

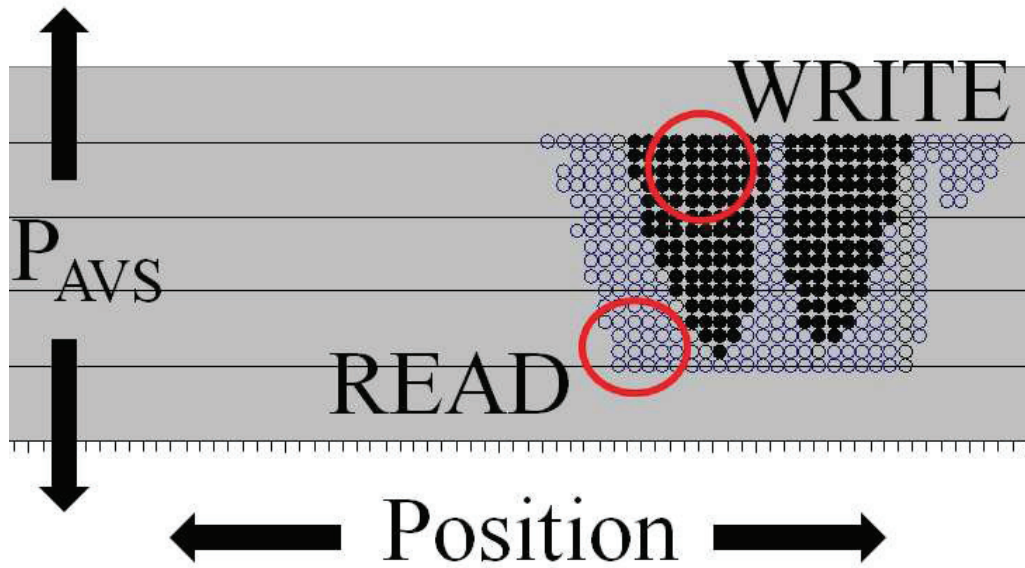


Figure 3.16: An example of RFID profiling with big offset between read and write. Empty circles indicate read only. Full circles indicate full read and write compatibility.

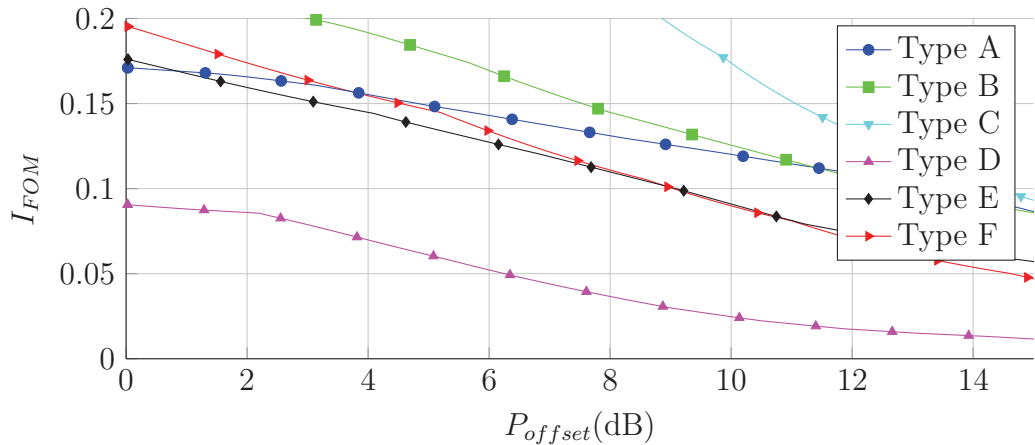


Figure 3.17: FOM sweep with $\Delta\Gamma$ zoomed over low power offset region.

the different transponder types, as compared to when they are treated separately. Type C exceeds the remaining types in performance, in the lower half of power offset. Type A, B and C are from the same vendor, of which Type C is the latest released product. For Type D a big difference between excluding and including $\Delta\Gamma$ is seen.

Another observation is the agreement between the FOM calculations and behavior in RFID profiling, as described in Section 2.1. Figure 3.16 shows an example of RFID profiling with big offset between read and write threshold, a different example from that shown in Figure 2.1. This means that the drive power has to be increased substantially to enable programming of the transponder as compared to only reading information from it. One probable explanation for this behavior is that non-linearity has an impact. In particular, a big offset between read and write has been seen for Type E and F in RFID profiling. In Figure 3.17 a zoomed in region of Figure 3.15 is shown. It is seen at approximately 1 and 4 dB power offset, respectively, how

Type E and F transition from higher to lower values of performance as compared to Type A, although this is not as evident for Type E. Type A is mentioned as reference here since during RFID profiling in particular Type A, E and F were compared.

Type D, which is from the same vendor as for Type C, but an older version, has also shown deviating performance in RFID profiling. Higher drive levels are needed for any type of response, but at this threshold immediate read and write compatibility is achieved. This is also confirmed in Figure 3.14, showing mismatch performance only, whereas a degraded performance is shown, when all FOM quantities are included, in Figures 3.15 and 3.17.

3.8 Conclusions FOM characterization

The developed FOM will most importantly give electrical information on performance related to the required adjustment in available power, needed for an arbitrary source, to go from an initial read response to full write compatibility in the transponder. The results show deviating performance between different transponder types, commercially available on the market. A high FOM yields higher flexibility to a change of source impedance, i.e., for a high FOM the mismatch condition does not change drastically during the offset adjustment, independent of the source environment. In other words a reliable reading and writing to the transponder chip can be achieved. It can also be done at low drive power levels. This is another requirement to achieve sufficient electromagnetic isolation in a dense tag environment, such as commonly found in a printer cavity.

Chapter 4

Programming of RFID inlays in the reactive near field

After a treatment of methods for non-linear characterization of RFID transponders, with focus on understanding their part in phenomena occurring in the RFID profiling process, a turn will now be made towards a more field theoretic topic; reactive near field (RNF) coupler technology for the programming of RFID inlays is considered. The transmission line loop and differential feeding concepts are treated, a critical combination needed for utilization of highly efficient coupling interaction with the current inductive loop of inlays.

4.1 Mutual interaction between inlays

In an initial investigation, the reactive near field mutual interaction in terms of power gain, as defined in Section 2.3.1, between two RFID inlay antennas located above and close to a common ground plane is investigated with finite element (FEM) simulations. The antennas are confined in parallel planes 1 mm apart. With reference to Fig. 4.1, one of the inlay antennas, which can be referred to as a stationary coupler geometry (CG) is located 1 mm above the ground plane, with an intermediate FR4 substrate. The port of the second inlay antenna, which may be referred to as a moving inlay geometry (IG), is terminated in a known load, roughly modeling a typical linear state value of RFID transponder impedance. The reference ports for the calculation of power gain are the antenna ports of the CG and IG, respectively. A strong mismatch, due to the close presence of the ground plane is expected, and hence a limit in the efficiency that can be achieved. Inlays are far field, or at least propagating near field, tuned devices; as such a ground plane located within a fraction of the wavelength acts as a two dimensional shield against radiation. However, in the simulation, and contrary to what is expected, very high levels of power gain are observed.

Note that weak coupling, in terms of power gain, where a perfectly matched source is assumed, will imply that higher Ohmic losses are dissipated in the materials of the coupling structure (inlays, ground plane and dielectric), as compared to the power transferred to the transponder. This is confirmed from far field simulations, showing very low levels of radiation, due to the ground plane. Assuming a lossless

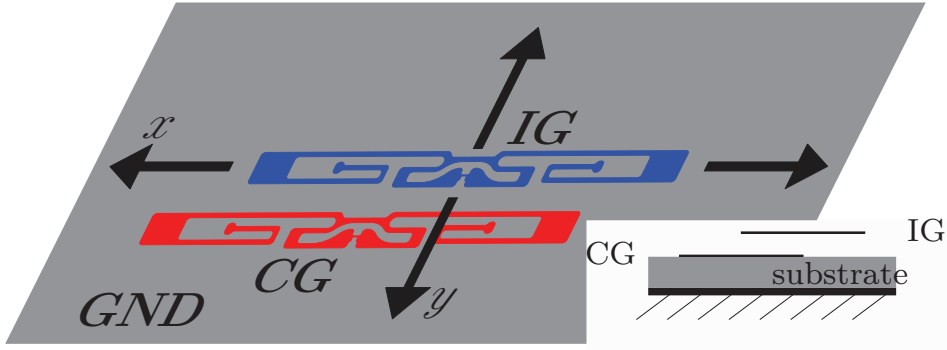


Figure 4.1: Illustration of relative inlay motion with mutual interaction.

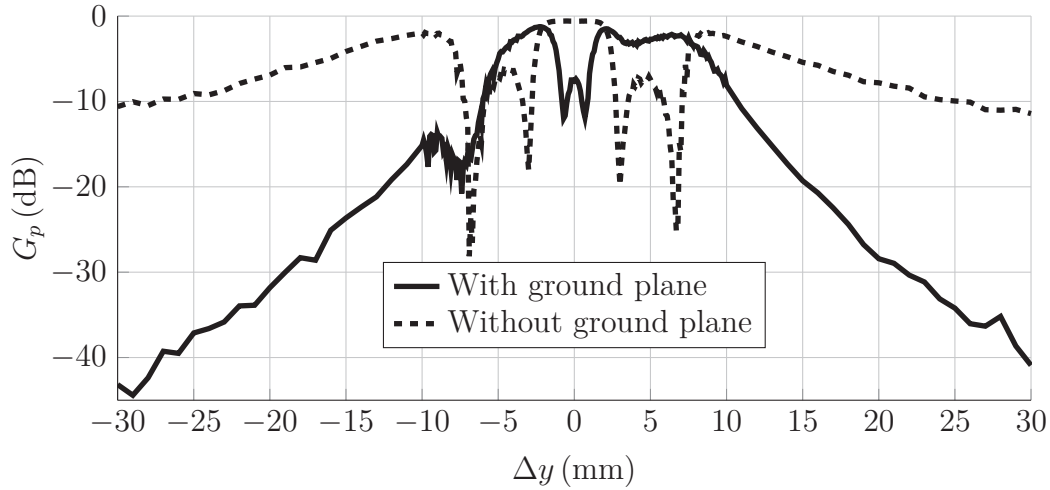


Figure 4.2: Simulated power gain of inlay to inlay interaction.

structure, the power gain will always be equal to unity, independent of the relative inlay position. An interesting fact, however, when observing the power gain as function of the spatial location for the lossy structure, is the drastic increase of power gain when the inlay inductive loops are aligned. This is evident from Fig. 4.2, where a motion in y -direction is considered, with $\Delta x = 0$. When $\Delta y = 0$, the inlays are perfectly aligned. For denotation purposes, the term *radiator* is used to distinguish the radiating geometry from the *inductive loop* geometry, identified as the closed metallic curve (or loop) connected to the transponder chip. The term *inlay antenna* is used to denote the entire geometry of the inlay.

After closer inspection around the origin, localized phenomena are seen, due to the influence of the reactive near field interaction between the radiators upon the direct loop to loop interaction, possibly in a destructive way, which may hence lead to reduced power gain. In a further simulation experiment the radiator is removed from the CG, as shown in Fig. 4.3. The resulting power gain is plotted in Fig. 4.4. Locally, around the origin, a changed behavior of the power gain is seen. Nodes are still distinguished, which are clarified by the embedded position indications. What is important, however, is the power gain at the origin. It has a close to unit power transfer. Clearly, the inlay under consideration exhibits strong reactive near

field interaction from the inductive loop. This is the idea behind the differential transmission line loop (DTLL), to be used as highly efficient coupling element.

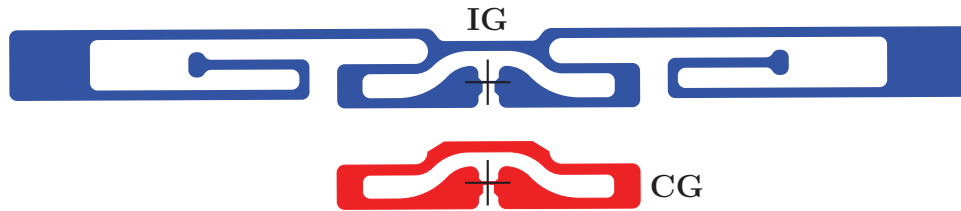


Figure 4.3: Removal of radiator.

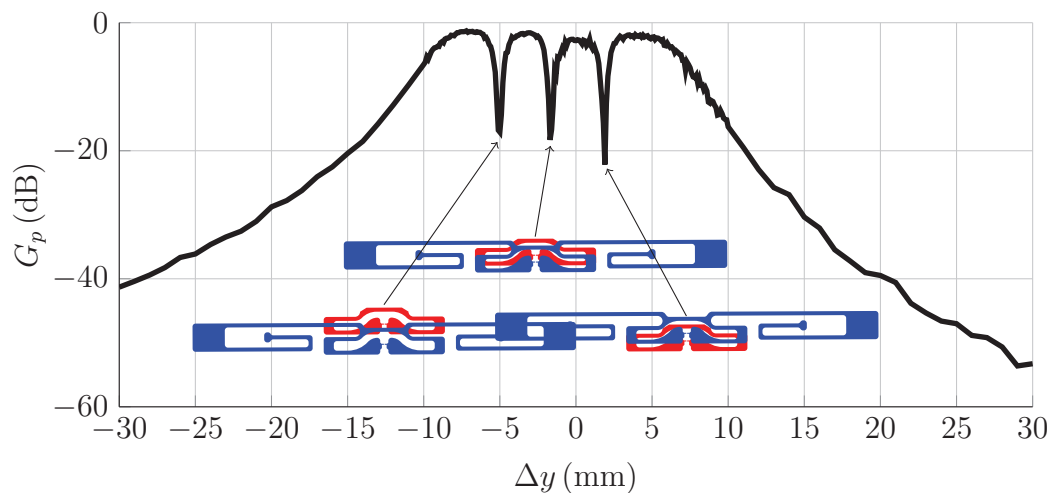


Figure 4.4: Simulated power gain between CG and IG without radiator.

4.2 The differential transmission line loop

The DTLL is a transmission line (TL), having both ends fed by a differential one port, may be analyzed by general traveling wave analysis. The last letter L here stems from the fact that in any realization, a meaningful differential excitation would imply having the terminals of the line located close together, hence forming a loop. At this point a remark is at hand. The use of the terms *CG* and *DTLL*, used interchangeably, may seem confusing. Actually, for an ideal balun transformation, from a single ended source environment to the differential input of the CG, the term DTLL is fully equivalent to the term CG, whereas for any practical realization the balun transformation is non-ideal. In the latter case, the CG denotes only the loop geometry of the DTLL, in which the balun is separated from the CG.

The DTLL geometry (or CG) is not a uniform structure. As transmission lines, microstrip lines are considered in the present work, due to the single ground plane and multi layer stackup, including the IG. Generally, given a uniform transmission

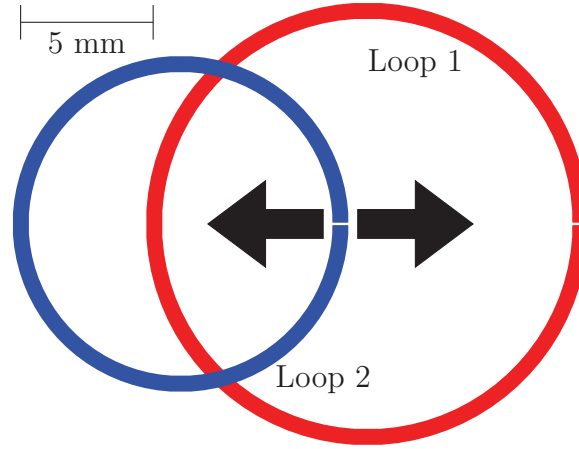


Figure 4.5: Simplified DTLT geometry with CG and IG represented by circles.

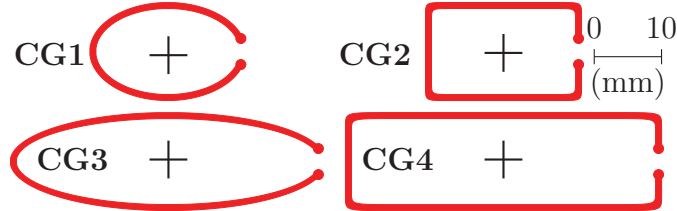


Figure 4.6: Super elliptical CG design variations used in measurements.

line with physical length l , propagation constant γ and characteristic impedance Z_c , the conditions for a differential excitation are

$$\begin{cases} V^+ + V^- = V \\ V^+ e^{-\gamma l} + V^- e^{\gamma l} = -V. \end{cases} \quad (4.1)$$

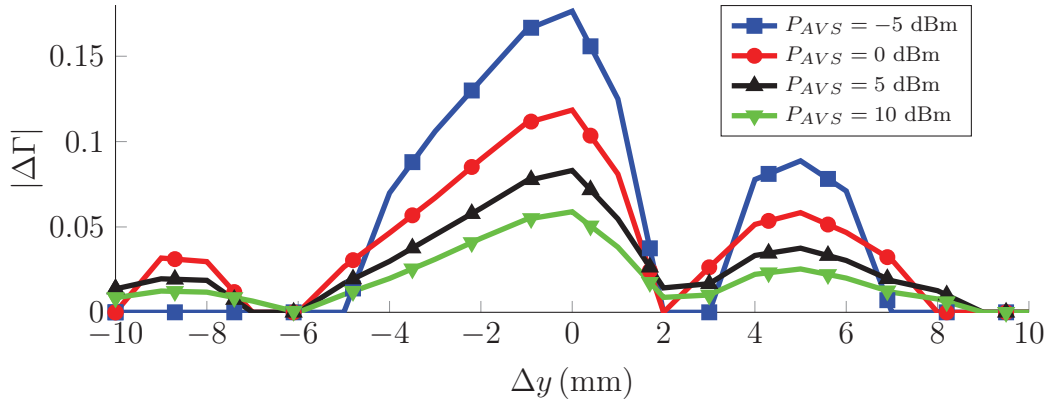
From (4.1) and the characteristic impedance $Z_c = V^+/I^+ = V^-/I^-$, a low loss approximation valid at UHF, the differential input impedance is obtained as

$$Z_{DM} = 2Z_c \tanh\left(\frac{\gamma l}{2}\right). \quad (4.2)$$

As shown in Papers C and D, for reasonable loops curvatures this calculation agrees well with the input and output Z -parameters ($Z_{11,22}$), when the reactive near field interaction of two CGs is considered. An example of a simplified geometry, with the CG and IG represented by circles, is illustrated in Fig. 4.5. Other shapes are possible as well, as those shown in Fig. 4.6, which are based on the super ellipse equation, given as

$$\left|\frac{x}{a}\right|^m + \left|\frac{y}{b}\right|^n = 1. \quad (4.3)$$

Generally, any closed curve equation can be used, as long as the curvature is not too strong, disqualifying the use of transmission line equations.

Figure 4.7: Measured compression impact on $|\Delta\Gamma|$.

4.2.1 The broadside coupling problem

From the interaction between the CG and the IG in the reactive near field, a broadside coupling problem can be identified. If in addition the CG and IG are confined in non-homogeneous media, such as the embedded stackup illustration in Fig. 4.1, with the fact that finite and non-uniform structures are considered, a less trivial problem is presented with no complete treatment found in literature. Historically, a popular research topic is uniform lines, on which literature is found for various configurations, such as coplanar [38], open [39, 40] and broadside [41–45]. In work reporting on the non-uniform case, the dimension in the direction of propagation is still of infinite extent [46]. In this situation, it is of interest to investigate if certain approximations can be found, which are valid for the present work.

Firstly, it is noted that the loop lengths considered in the present work are always limited in length, as to present an input impedance having inductive reactance. For the uniform differentially excited line, this implies that the electrical length is limited to half of the guided wave length. The reason of this restriction is that no zero crossings of the line current are allowed, which would imply reduced coupling due to destructive interference from the EM field not being uniform over the loop surface any longer.

Secondly, as mentioned previously, when the two-port mutual interaction of both loops are considered, the input and output $Z_{11,22}$ -parameters may be modeled as the input impedance given by (4.2). This is an important result, since in a coupler design the circuit may then be optimized for the unloaded state with respect to input return loss, where it is known that coupling tends to increase in the loaded state. By using the Q -value reduction, described in Section 2.3.2, further flexibility of matching in both the unloaded and loaded state is provided simultaneously, utilizing the low threshold power of transponder operation. Note that this is actually a preferred situation, since the backscatter response is then maximized, as discussed in Section 3.5.1 (no load compression). Further measurements on compression behavior are carried out in Paper D, where the change of the $|\Delta\Gamma|$ -value (3.12) is observed at the input of the DTLL (with balun realization) for different port power levels, as shown in Fig. 4.7. In this case the interaction between CG1 in Fig. 4.6 and the inlay in Fig. 4.3 is measured.

For a full specification of the two-port interaction between the CG and the IG, the mutual impedance parameters are also needed. It turns out that analytic treatment is also possible for this case. In Paper C, a model for this interaction is developed. The Biot-Savart law (BS) is used to approximate the more general radiation integral (RI), where both integrals are given as

$$\mathbf{H}_{\text{BS}}(\mathbf{r}) = \frac{1}{4\pi} \int_{S'} \frac{\mathbf{J}(\mathbf{r}') \times \mathbf{a}_R(\mathbf{r}') dS'}{R^2} \quad (4.4)$$

$$\mathbf{H}_{\text{RI}}(\mathbf{r}) = \frac{1}{4\pi} \int_{S'} \left(\frac{jk}{R} + \frac{1}{R^2} \right) e^{-jkR} \mathbf{J}(\mathbf{r}') \times \mathbf{a}_R(\mathbf{r}') dS'.$$

From calculations it is concluded that also a thin wire approximation holds. The currents along the CG and IG are calculated as

$$I_{1,2}(x) = \frac{V}{Z_{c1,2}} \frac{\cosh(\gamma(l_{1,2} - x)) + \cosh(\gamma x)}{\sinh(\gamma l_{1,2})} \quad (4.5)$$

from manipulation of (4.1). When the Biot-Savart integral in (4.4) is combined with (4.5), under given curve equations describing the CG and the IG, the fundamental result arrived at are the closed form expressions for the mutual impedance parameters, according to

$$Z_{21} = \frac{j\omega\mu}{4\pi I_{10}} \int_{S_2} \int_{s(0)}^{s(1)} I(s') \frac{\dot{\mathbf{C}}(s') \times (\mathbf{r} - \mathbf{C}(s'))}{\|\mathbf{r} - \mathbf{C}(s')\|^3} ds' \cdot d\mathbf{S} = Z_{12}. \quad (4.6)$$

In (4.6), \mathbf{C} is a re-parametrization by arc-length. Further details are given in Paper C, where a good agreement is found between the model and FEM simulated data.

In summary the model is valid, when the CG and IG loop lengths have a restriction in electrical lengths to about $0.32\lambda_g$, and under the assumption that the current distribution on either one of the loops is not affected by the presence of the current distribution on the other loop, when it is in the open circuited state.

4.2.2 Balun transformation

From a single ended source system, such as the coaxial antenna port of an interrogator, a balun transformation is required for the differential excitation in the CG. In the analysis so far, an ideal balun transformation has been assumed. In the work of Paper D, the DTLL realization has a real to real balun transformation, following the design rules of previous work, which is shown in [47]. Hence a phase compensation is needed to resonate the inductive reactance of the CG, located at the output of the balun. A resistor, for Q -value reduction, is further shunted with the capacitor. A photo of the realization, with circuit schematic is shown in Fig. 4.8. The balun shows satisfactory performance for the DTLL demonstrator, with further details on measured data found in Paper D.

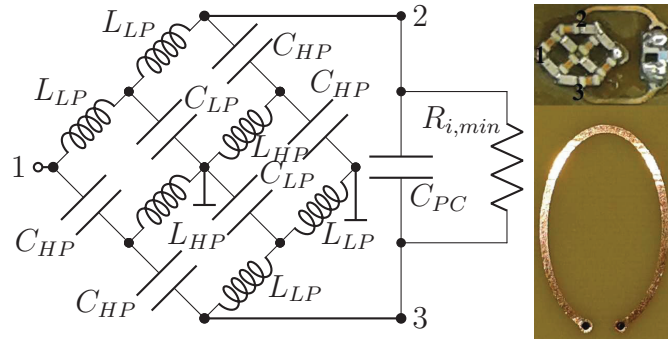


Figure 4.8: Left: Circuit topology of component side, including balun, phase compensation, and Q -value reduction ($R_{i,min}$). Right: Realization of component side (top) and loop side (bottom).

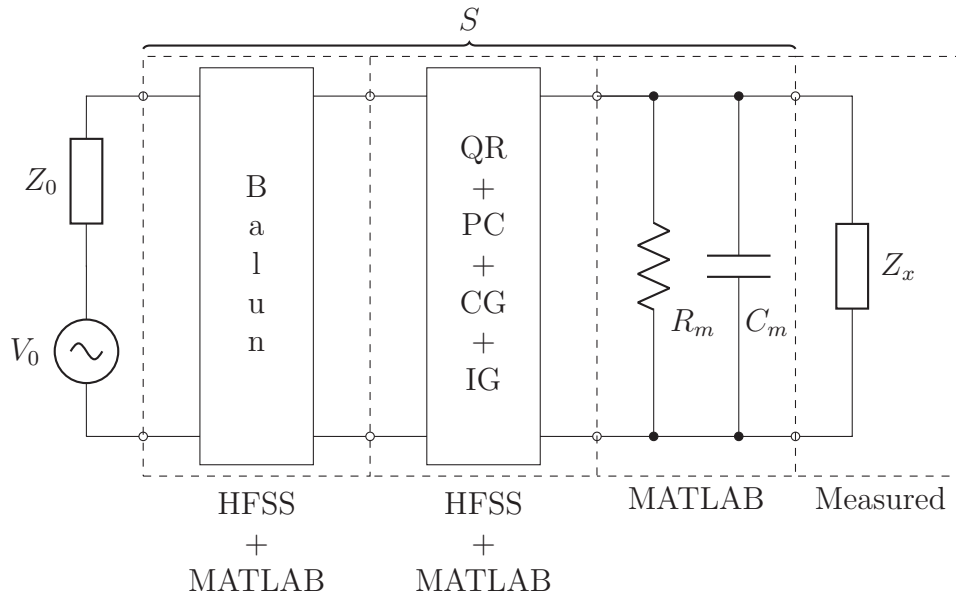


Figure 4.9: S -parameter representation of interaction between DTLL and IG.

4.2.3 Predicted and measured results

The different components of the DTLL have been covered and a complete block schematic is shown in Fig. 4.9. The linear channel was discussed in Section 2.3, which is represented by the S -parameter block in Fig. 4.9. It contains the source, which in Paper D is the interrogator antenna port, having an impedance of 50Ω . Further the lumped realization of the balun is included, with Q -value reduction (QR) and phase compensation (PC). The electromagnetic interaction is then comprised of the CG and IG, as previously discussed. Since commercially available inlays are considered, mounting parasitics need to be taken into account, represented by the shunt connection $R_m || C_p$ [48]. Finally, the bare wafer transponder RF front end is represented by Z_x , with measured data taken from Paper B.

Since data are known from probed $\Delta\Gamma$ -value measurements of the transponder RF frontend impedance (Paper B), and a combined simulation using HFSS (FEM)

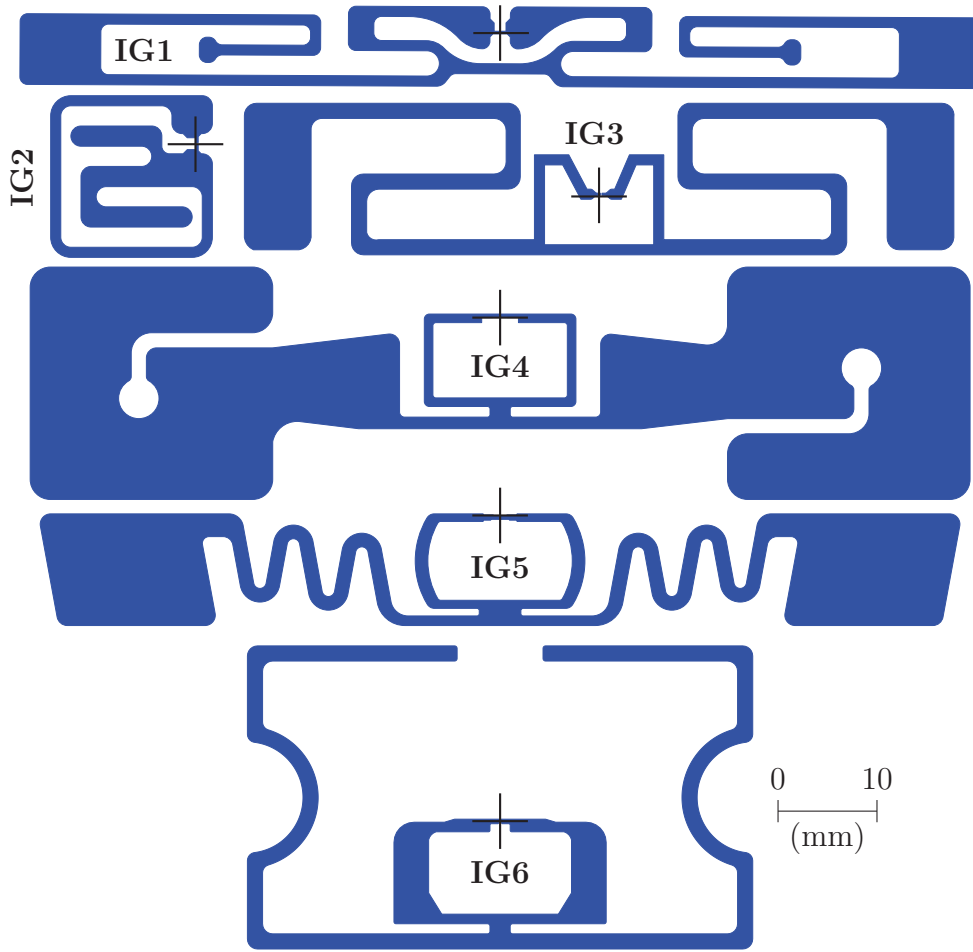


Figure 4.10: Chosen inlay geometries (IGs) for validation.

and MATLAB (node analysis), a prediction for the measured $\Delta\Gamma$ -value at the input of the DTLL (antenna port interface) is possible. Power gain (G_p) is used as reference for the interaction between the CG and IG. Hence it is of interest to find a relation between the power gain and the $\Delta\Gamma$ -value at the input of the DTLL. By combining (2.3) and (2.5) with low and high pulse impedance data from the transponder chip measurements, the $\Delta\Gamma$ -value at the DTLL input can be written

$$|\Delta\Gamma_{in}| = \frac{(1 - |\Gamma_{inL}|^2) |1 - S_{22}\Gamma_{xL}|}{(1 - |\Gamma_{xL}|^2) |1 - S_{22}\Gamma_{xH}|} |\Delta\Gamma_x| G_{pL}. \quad (4.7)$$

For the measurements CG1 (Fig. 4.6) and six different commercially available IGs, illustrated in Fig. 4.10, are chosen. The measurement setup is shown in Fig. 4.11. The instrumentation in this setup is identical to the one used for transponder characterization, described in Section 3.6, but with added xy -motion control. The same MATLAB application is used, where additional code is added for the motion control. Note that the same type of data is captured as in the transponder characterization, but the measurement reference plane is moved to the input of the DTLL instead,

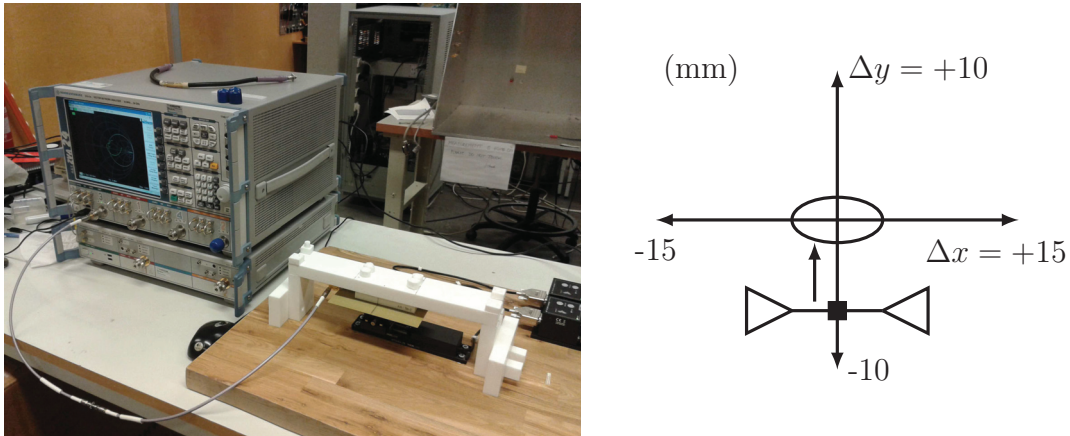


Figure 4.11: Left: Measurement setup. Right: Relative motion sequence.

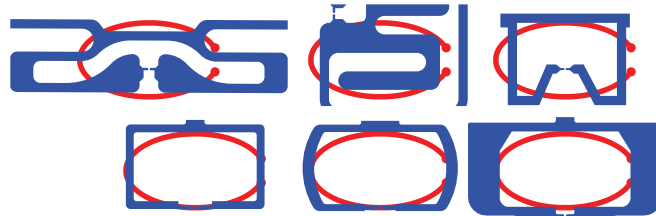


Figure 4.12: Relative positions of peak $|\Delta\Gamma|$.

which hence includes the wireless interaction between the CG and IG over spatial sweep. The motion sweep is illustrated in the right of Fig. 4.11.

In Fig. 4.13 on page 48 the simulated and calculated (predicted) spatial y -sweep of the $|\Delta\Gamma|$ -value at the DTLL input is compared with measured data. The reason for choosing the y -direction is to better distinguish the loop to loop interaction, which is otherwise more difficult due to TL coupling with the radiator, as seen from the orientations in Fig. 4.10. Intuitively, when looking more closely at the geometries in Fig. 4.10, it is expected that strong interaction would occur when the CG is aligned with the inductive loop of the inlays. This is also the obtained result, when observing the relative positions of maximum $|\Delta\Gamma|$, as shown in Fig. 4.12. The drastic change from a value of zero in Fig. 4.13 clearly shows a spatially selective behavior.

In the prediction (4.7), the non-linear transponder chip impedance is re-calculated, by transforming the probed transponder measurement data from the probed source environment to the actual impedance, corresponding to the source environment given in Fig. 4.9 [49]. Hence non-linearity is taken into account. Yet still, after closer observation, it is seen that the measured results deviate from the simulations for cases a)–b). The transponder types for these IGs are from the same vendor. Good agreement is seen for cases c)–f), which are also from the same vendor, but on which the parasitic model in the present work is based. The agreement indeed suggests the same bonding process [48]. There is no available data for the parasitic model of cases a)–b).

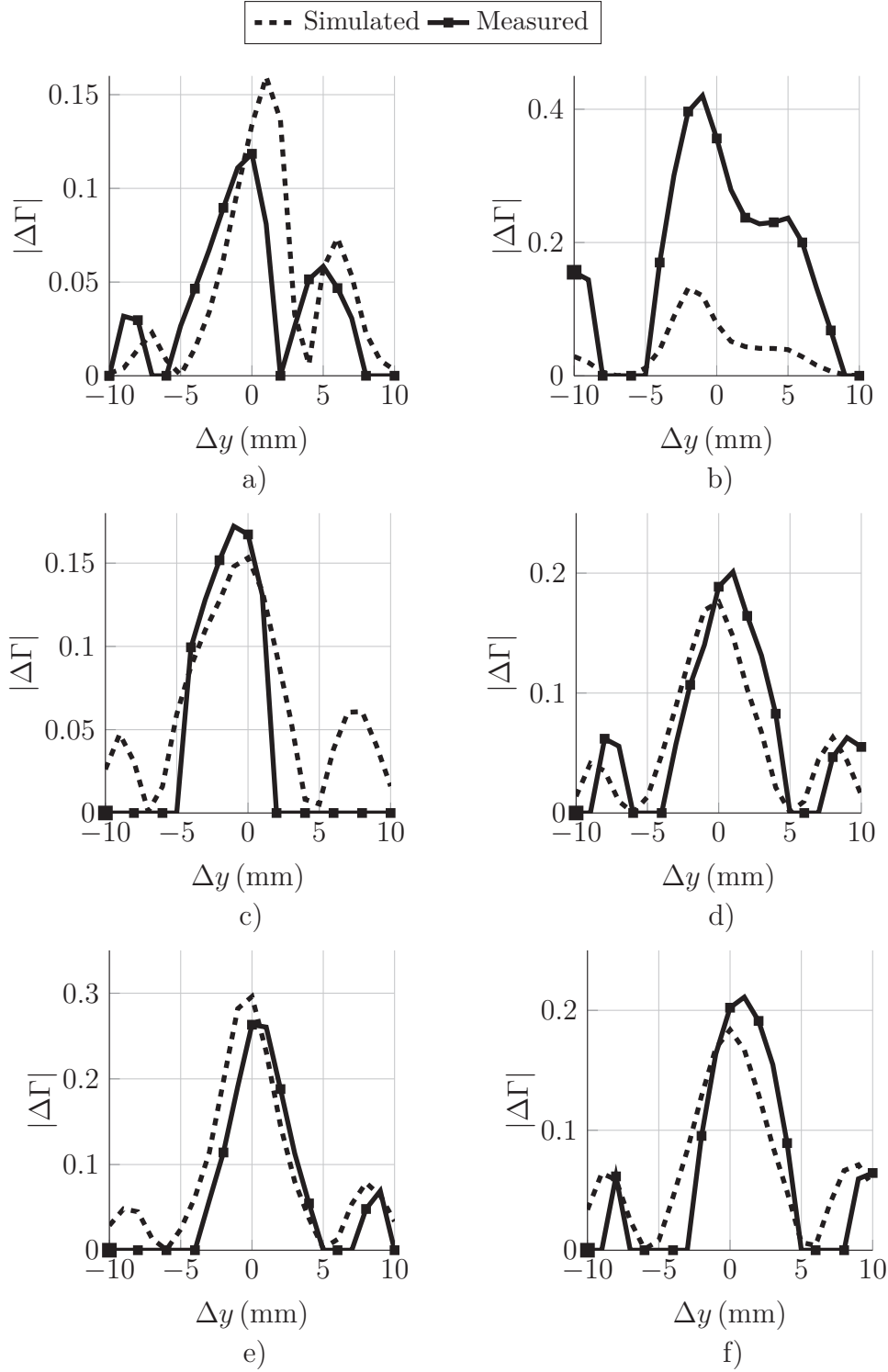


Figure 4.13: Simulated and measured $|\Delta\Gamma|$ for CG1. a) IG1. b) IG2. c) IG3. d) IG4. e) IG5. f) IG6.

Table 4.1: Simulated Peak Power Gain (page 50).

IG	$G_{p,max}$ (dB)	IG	$G_{p,max}$ (dB)
IG1	-0.6	IG4	-0.3
IG2	-1.4	IG5	-0.3
IG3	-0.4	IG6	-0.4

As reference for the simulations in Fig. 4.13, the linear power gain corresponding to the interaction between CG1 and IG1–IG6 is plotted in Fig. 4.14 on page 50, with the peak values explicitly listed in Table 4.1. It is seen that in all cases the peak values are close to unity. This data is an important reference since it reveals what can be achieved in the best case, with a high performance balun transformation and minimum non-linear impact from the transponder. Any internal losses, such as resistive and radiation will decrease the power gain, hence making it a good indicator for efficiency, in this case with values above 80%. It is concluded that the DTLL is a good candidate for highly efficient coupling elements, which furthermore are compatible with a variation in inlay geometry.

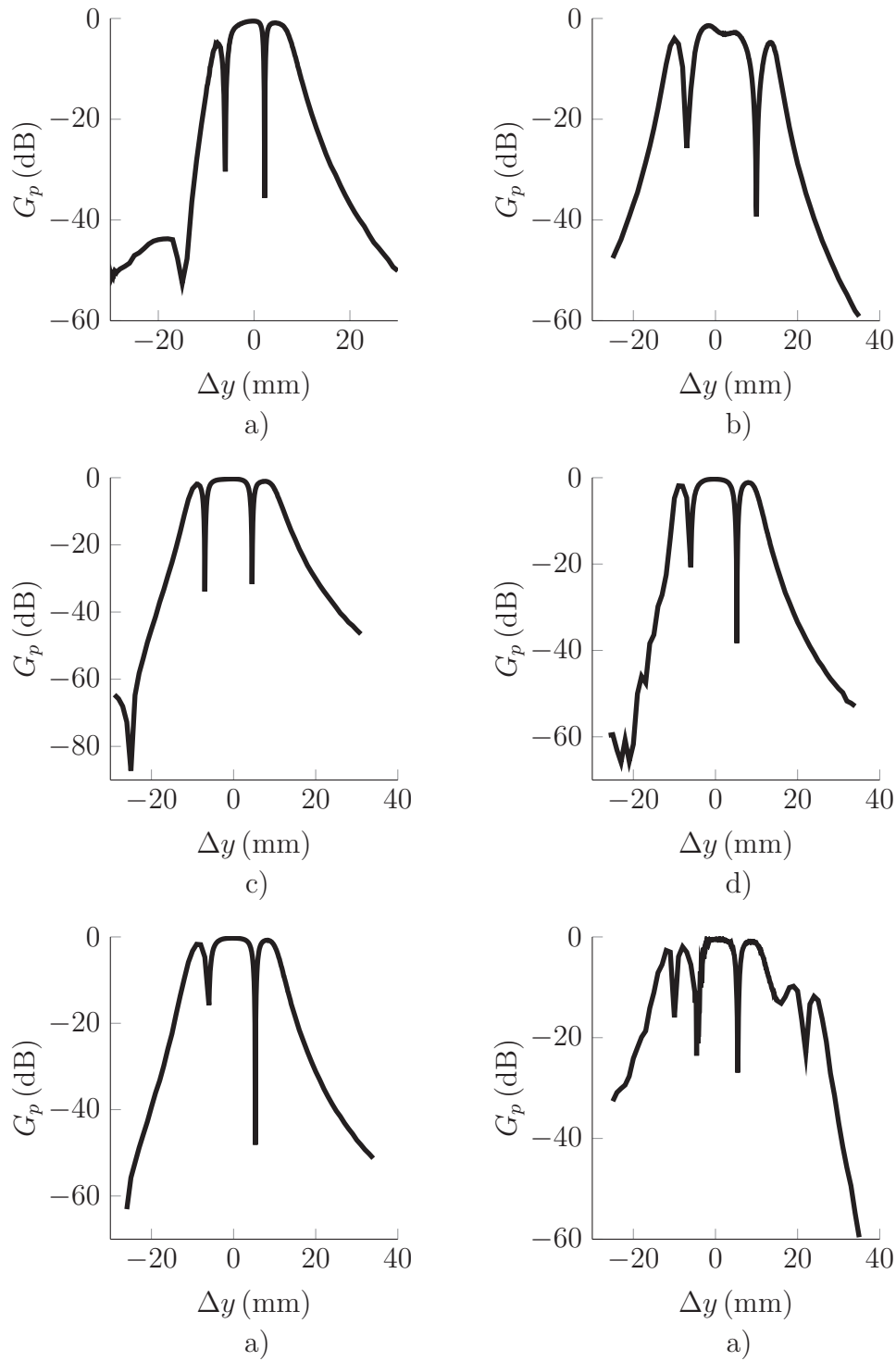


Figure 4.14: Simulated spatial sweep of power gain for CG1. a) IG1. b) IG2. c) IG3. d) IG4. e) IG5. f) IG6.

4.3 Balun concepts

A critical component in the DTLL is the balun transformation, with feed signal conversion from a single ended system to the differential input of the CG [50, 51]. For the demonstrator in Paper D, design rules in previous work, for a lumped realization, is followed [47]. The concept of this work is wide band real to real impedance transformation. It is of interest to know if more compact designs, still in lumped form, can be achieved for an all over more compact design of the DTLL, with higher efficiency by minimizing the losses in the balun, when the DTLL is regarded as a coupling element. This is the starting point for separate work on baluns presented in Papers E and F, in which lumped baluns with inherent complex impedance transformation are considered. The direct complex transformation enables the direct matching between complex impedance references and hence more compact designs may be achieved. The critical factor, however, arising here is the operational bandwidths than can be maintained.

4.3.1 Reported work on balun transformation

Considering, in particular, baluns with complex impedance transformation, as compared to real to real transformation, doubtlessly, real to real transformation has been the most dominating research topic [52–54]. In a common configuration, these baluns then need external matching circuitry acting as interface between the complex and real impedance environment [55, 56].

Little work is found on baluns with inherent complex impedance transformation. Usually, these baluns comprise distributed components in one way or the other [57–61]. In Papers E and F, specifically the lumped concept with inherent complex impedance transformation is treated. The foundation for the considered topologies is the real to real impedance transforming out-of-phase-compensated-power-splitter [62], which is also used in the DTLL demonstrator [47, Paper D]. The topology is shown in Fig. 4.15. A modification of this topology enables complex impedance transformation.

4.3.2 Modification for complex impedance transformation

With reference Fig. 4.15, certain modifications are possible in this original topology when a reactive load is considered, by letting part of the load reactance at the operating frequency replace certain internal balun components, which consequently may be removed. The motivation behind this replacement is a simplification of the node analysis. In other words the reactance of the balun is adjusted in accordance to the values of the load impedances, to fulfill the properties required for the circuit to act as a balun. Accordingly, for an inductive load a reduction of internal inductance may be achieved by removal of L_{HP} (node 5 and 6). Correspondingly, for a capacitive load C_{LP} is removed (node 4 and 7). Note that the removal of these particular components, in the respective cases, is the only possibility to remove internal inductance and simultaneously keep the power splitting possibility and duality of the balun. In the inductive case the remaining series connections of capacitors C_{HP1} and C_{HP2}

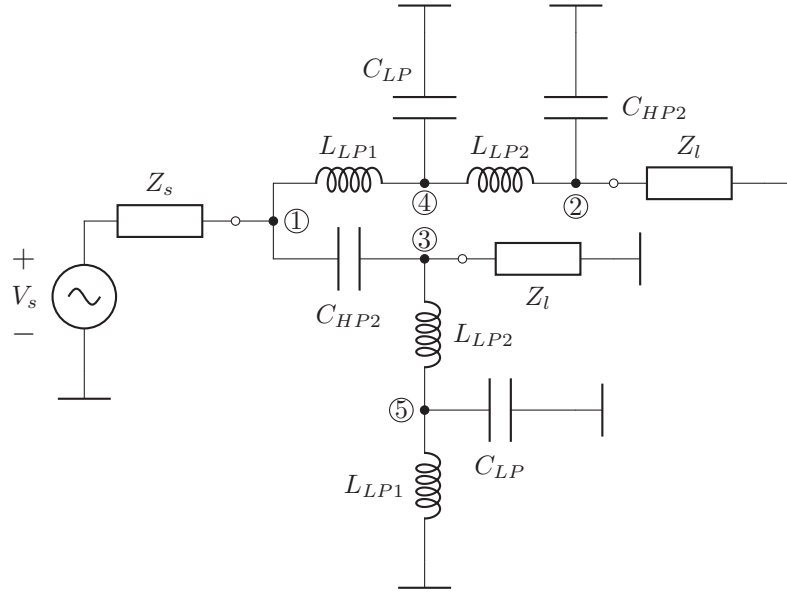


Figure 4.16: LP topology.

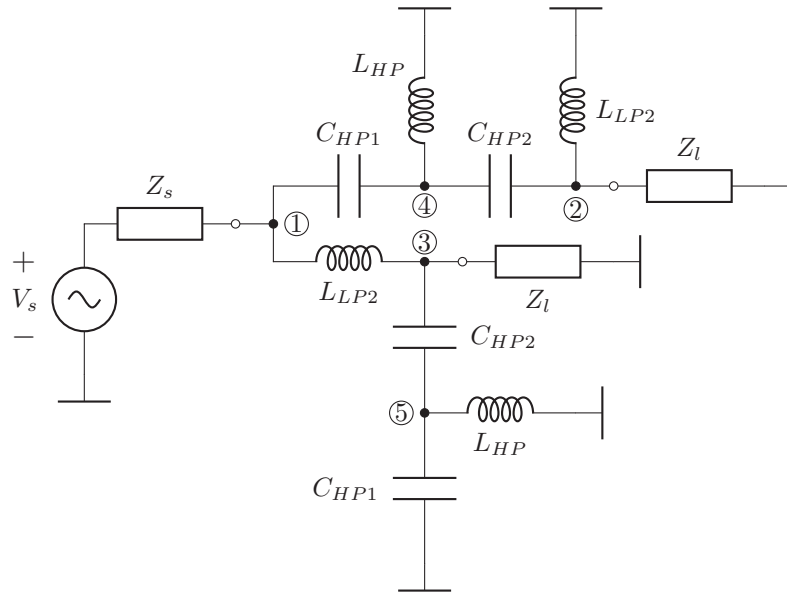


Figure 4.17: HP topology.

Correspondingly, for the HP topology C_{HP2} is chosen as free variable, leading to

$$L_{LP2} = \frac{1}{n_{LHP}^2 \omega_0^2 C_{HP2}} \quad L_{HP} = \frac{2 - n_{LHP}^2}{\omega_0^2 C_{HP2}} \quad C_{HP1} = \frac{n_{LHP}^2 C_{HP2}}{2 - n_{LHP}^2}. \quad (4.9)$$

In both topologies, free variables are in the sense that $n_{LP,LHP} \in (0, \sqrt{2})$ must hold for physical component values. The resulting balance parameters, shown in Fig. 4.18, become

$$b_{23,LP} = -\frac{1}{\bar{\omega}^2} \frac{1}{2 - \bar{\omega}^2} \quad b_{23,HP} = \frac{1 - 2\bar{\omega}^2}{\bar{\omega}^4}. \quad (4.10)$$

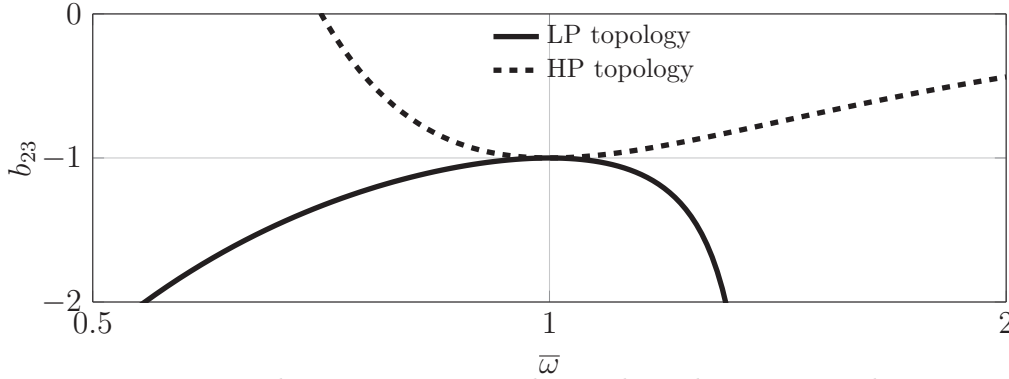


Figure 4.18: Balance parameter with vanishing derivative condition.

An important conclusion, except the independency of the balance parameters, is that their bandwidths neither become better nor worse than these fixed relations, and hence they put a limit on the total operational bandwidth. The LP (BW_{LP}) and HP (BW_{HP}) bandwidths, for a given maximum value of accepted amplitude imbalance in dB (AIB), may be calculated numerically from the solutions of

$$\begin{aligned} (2 + BW_{LP}^2) (8 - (2 + BW_{LP}^2)^2) &= 16 \times 10^{-\frac{AIB}{20}} && \text{(LP topology)} \\ \frac{8(2 - BW_{HP}^2)^2 - 16}{(2 - BW_{HP}^2)^4} &= 10^{-\frac{AIB}{20}} && \text{(HP topology)}. \end{aligned} \quad (4.11)$$

The last condition for the full determination of the component values is return loss, which is here specified at the operating frequency for given values of source ($Y_s = G_s + jB_s$) and load ($Y_l = G_l + jB_l$) admittances. The finite intervals $n_{LP,LHP} \in (0, \sqrt{2})$ will imply that a conjugate match at the input for an arbitrary choice of source and load impedance is not possible. For any practical implementation, the availability of component values is furthermore limited. A more realistic requirement would be that of best achievable return loss, rather than a conjugate match. By using the arrangement in (4.8)–(4.9) and carrying out the node analysis for the circuits in Figs. 4.16 and 4.17, the input reflection coefficient, in terms power waves, may be expressed as [34]

$$\begin{aligned} \Gamma_{in} &= \frac{V_1}{V_s} \left(Y_s + \frac{Y_s^2}{Y_s^*} \right) - \frac{Y_s}{Y_s^*} \Big|_{\omega=\omega_0} \\ &= \frac{\Delta_{11}}{\Delta} \left(Y_s + \frac{Y_s^2}{Y_s^*} \right) - \frac{Y_s}{Y_s^*} \Big|_{\omega=\omega_0} \\ &= \frac{1}{a - \frac{b^2 f + c^2 d}{df - e^2}} \left(Y_s + \frac{Y_s^2}{Y_s^*} \right) - \frac{Y_s}{Y_s^*} \Big|_{\omega=\omega_0} \end{aligned} \quad (4.12)$$

where Δ_{ij} is the ij :th cofactor of the nodal admittance matrix (\mathbf{Y}) and $\Delta = \det(\mathbf{Y})$.

The nodal admittance matrix elements are explicitly given as

$$\begin{aligned}
 a &= Y_s + \frac{1}{j\omega L_{LP1}} + j\omega C_{HP2} & b &= -j\omega C_{HP2} \\
 c &= -\frac{1}{j\omega L_{LP1}} & d &= Y_l + \frac{1}{j\omega L_{LP2}} + j\omega C_{HP2} \\
 e &= -\frac{1}{j\omega L_{LP2}} & f &= \frac{1}{j\omega L_{LP1}} + \frac{1}{j\omega L_{LP2}} + j\omega C_{LP}
 \end{aligned} \tag{4.13}$$

for the LP topology, and

$$\begin{aligned}
 a &= Y_s + \frac{1}{j\omega L_{LP2}} + j\omega C_{HP1} & b &= -\frac{1}{j\omega L_{LP2}} \\
 c &= -j\omega C_{HP1} & d &= Y_l + \frac{1}{j\omega L_{LP2}} + j\omega C_{HP2} \\
 e &= -j\omega C_{HP2} & f &= j\omega C_{HP1} + j\omega C_{HP2} + \frac{1}{j\omega L_{HP}}
 \end{aligned} \tag{4.14}$$

for the HP topology. By substituting (4.8)–(4.9) into (4.12)–(4.14), the input reflection coefficient is defined according to

$$\Gamma_{in} : (C_{LP}, n_{LP}) \rightarrow \mathbb{C}, \quad (C_{LP}, n_{LP}) \in (0, \infty) \times (0, \sqrt{2}) \tag{4.15}$$

for the LP topology and

$$\begin{aligned}
 \Gamma_{in} &: (C_{HP2}, n_{LHP}) \rightarrow \mathbb{C}, \\
 &(C_{HP2}, n_{LHP}) \in (0, \infty) \times (0, \sqrt{2})
 \end{aligned} \tag{4.16}$$

for the HP topology. The task is now to minimize Γ_{in} with respect to (C_{LP}, n_{LP}) or (C_{HP2}, n_{LHP}) , depending on topology, to determine their values. The remaining component values are then obtained from (4.8) or (4.9). Further details on the derivations and a design procedure are found in Paper F.

4.3.4 Experimental validation with demonstrators

For experimental validation, a number of design cases are considered, shown in Fig. 4.19. The operating frequency is chosen to 925 MHz. A photo of the LP realization is shown in in Fig. 4.20. The same layout is used for all design cases and both the LP and HP topologies, with further photos shown in Paper F. FEM simulations are needed for the optimization of component values in the realizations at UHF, since parasitics from the layout have a strong impact.

The parameter of highest importance is the balance parameters and these results are presented here. Further data, such as statistical analysis with respect to component tolerances and measured data of return and transmission loss are found in Paper F. The amplitude and phase imbalance for all design cases are plotted in Figs. 4.21–4.22 (page 57). The results show that an amplitude imbalance of better than ± 1 dB and a phase balance of better than $\pm 5^\circ$ over a 20% bandwidth is achieved. These results also agree with predictions from Monte Carlo simulations.

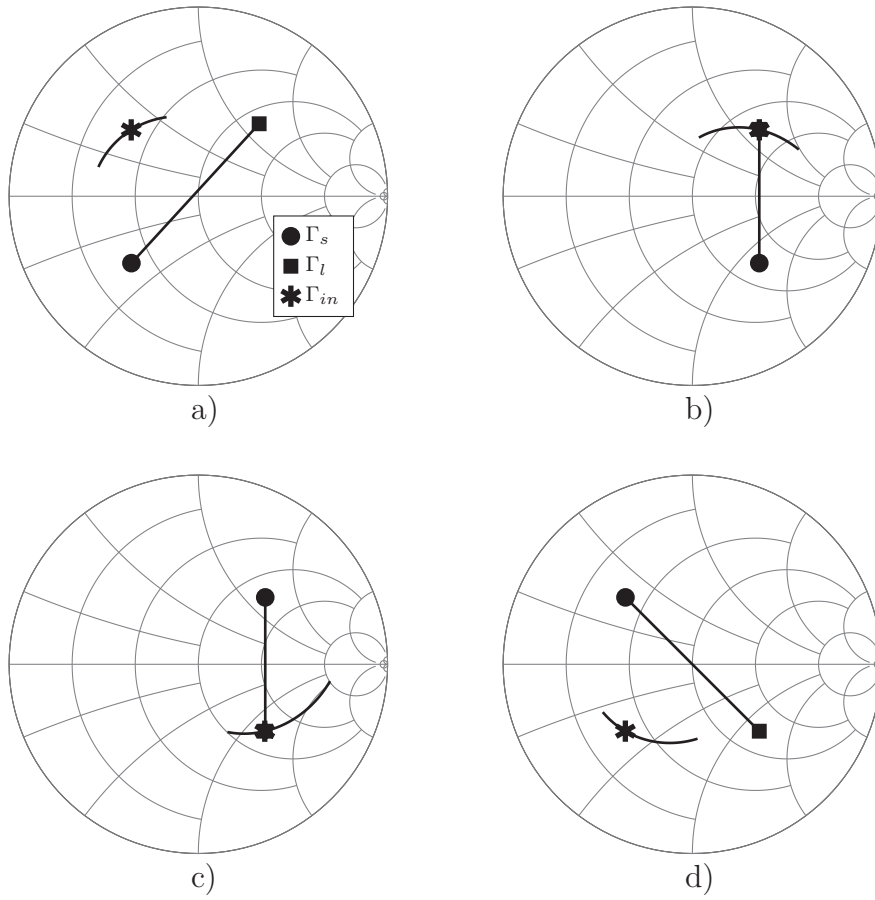


Figure 4.19: Chosen design cases. a) Case 1 and b) Case 2 with LP topology. c) Case 3 and d) Case 4 with HP topology.

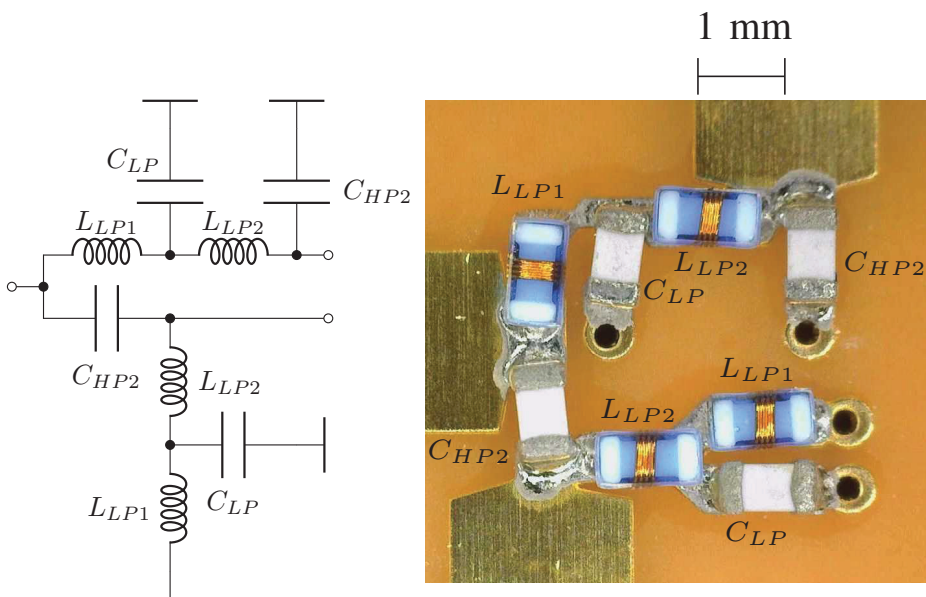


Figure 4.20: Realization of LP topology.

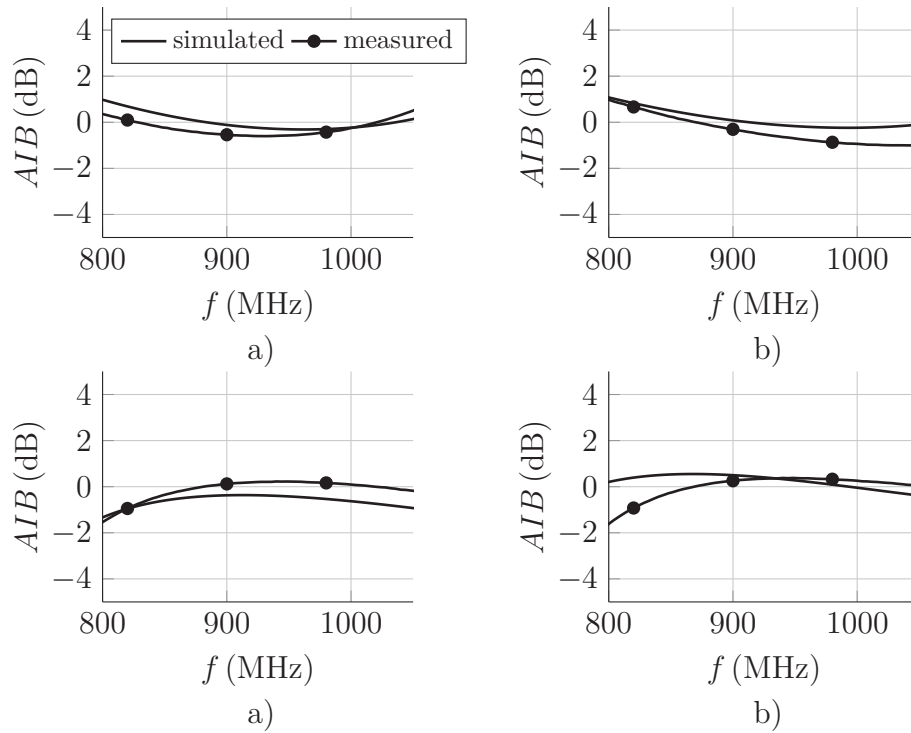


Figure 4.21: Simulated and measured amplitude imbalance. a) Case 1. b) Case 2. c) Case 3. d) Case 4.

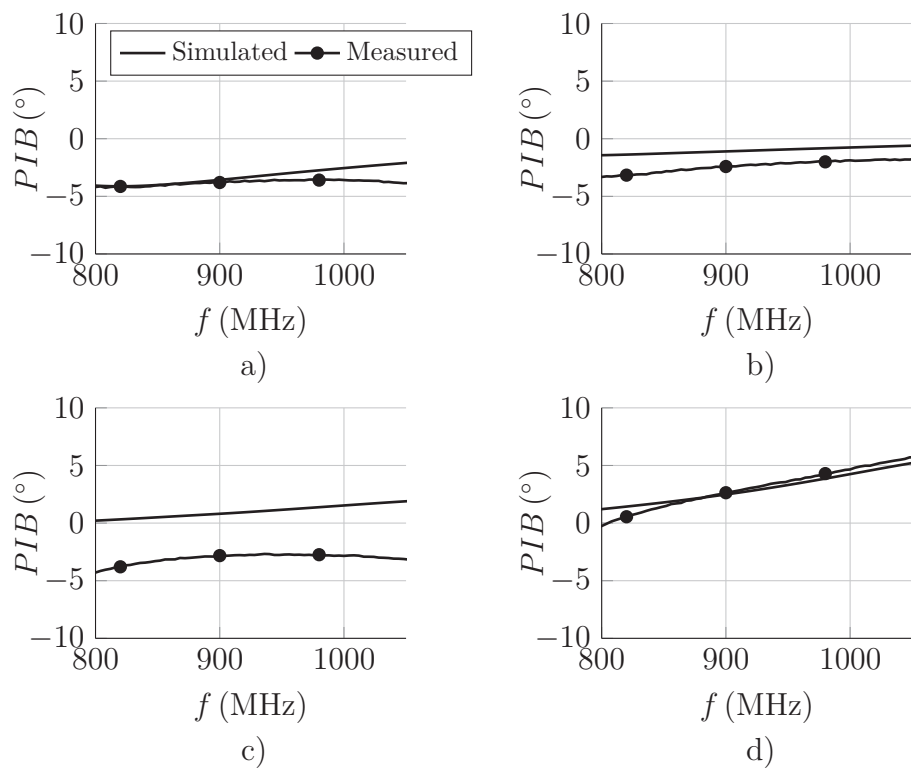


Figure 4.22: Simulated and measured phase imbalance. a) Case 1. b) Case 2. c) Case 3. d) Case 4.

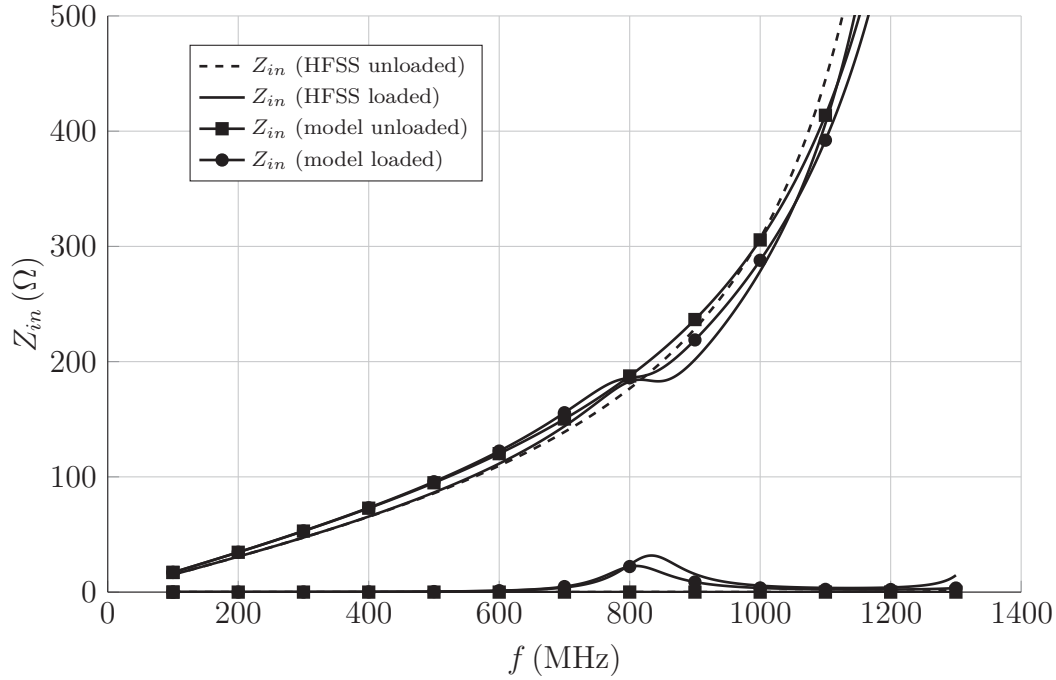


Figure 4.23: Simulated and modeled total input impedance.

4.3.5 Discussion on balun transformation for DTLL

For the considered design cases, the presented theory on lumped baluns with inherent complex impedance transformation in Sections 4.3.2–4.3.4 shows satisfactory balance performance over roughly a 20% bandwidth. Of interest in the remaining part of this thesis, is the particular load impedance given by the differential input port of the CG and IG interaction, as discussed in Section 4.2. The high values of simulated power gain reappears for all the considered loop geometries, also the more theoretical lossless case considered in Paper C (Fig. 4.5), with a chosen transponder impedance representing a typical commercially available value. This particular case gives a good indication of the behavior in the unloaded state, as compared to the loaded state. The modeled and simulated total input impedance of the CG and IG interaction is plotted in Fig. 4.23. It is observed that, despite a power gain close to unity in the loaded state with the most notable change arising in the real part, it still remains high- Q . Note that an impedance with this character, topologically, has the same local frequency behavior for the reactance, independent of the reactive component being in series or shunt configuration. To clarify, let an impedance with inductive character consist of a resistance (R_s) in series with an inductance (L), denoted $Z = R_s + j\omega L$, where $\omega L \gg R_s$. The admittance will then be

$$Y = \frac{1}{Z} = \frac{R_s - j\omega L}{R_s^2 + \omega^2 L^2} \stackrel{\omega L \gg R_s}{\approx} \frac{R_s}{\omega^2 L^2} + \frac{1}{j\omega L}. \quad (4.17)$$

which shows that the same inductance value is found both in the series and shunt topologies.

The Q -value reduction at the output of the balun in Paper D is not the only possibility of broadening operational bandwidth. This raises an interesting point. Assume that the DTLL is regarded as a coupling element, amongst several, and the balun transformation transforms the high- Q input impedance of the CG and IG interaction to yet another inductive high- Q impedance value, seen at the input of the balun, without any Q -value reduction. The reason why an inductive input impedance of the DTLL is considered will be explained in the next chapter. In this situation, if the DTLL is shunted onto a feeding transmission line (TL), which is terminated, the source environment being presented towards the DTLL could then also represent a Q -value reduction. It is then clear, from the low threshold values of transponders, that several DTLLs may be shunted onto the feeding TL, hence forming an array, provided the input impedance of each DTLL does not have a too strong loading impact. Further help on matching the array input impedance to the system input (interrogator output) may be provided by proper choice of the termination impedance, which then has a value depending upon the number of DTLL elements. The next and final chapter will be devoted to this subject.

Chapter 5

Discussion: Implementation of DTLL in sensitive array applications

In this final chapter the perspective is lifted to a discussion on adaptivity for a complete coupler solution, in which the contribution of each paper summarized in the previous chapters play a part. Firstly, the work on transponder characterization shows low threshold powers of operation, being a common property for all types of RFID transponders. An operation as close as possible to the threshold power is further preferred, in order to avoid compression being detrimental to the communication quality. Secondly, the DTLL coupling element in interaction with the inlay exhibits spatial selectivity and very high coupling efficiency, above 80% (power gain values close to unity). The combination of these two major results, low transponder threshold powers and the highly efficient coupling element, can be utilized to form an array of several DTLLs with satisfactory input return loss bandwidth of the coupler array. Coupling properties may be further enhanced by phase manipulation of the feeding signal along which the DTLL elements are shunted. A short theory on this topic follows, after which some concluding remarks pertaining to the complete coupler solution are made.

5.1 Conceptual idea

The main idea behind the self adaptive principle is to connect a plural of DTLL coupling elements in an array by a terminated transmission line (TL), segmented into several phase shifting (PS) elements, such as the element illustrated in Fig. 5.1. Generally, any type of phase shifter may be used, determined by the application and desired coupling characteristics of the array. One type of phase shifter is phase compensation (PC), which is needed for a homogeneous electromagnetic field along the array. The lossless theory for short segments is treated in Paper G. Another type is the 180° phase shifter, which may be simply realized by a half wavelength TL.

The shunt admittance Y_{DTLL} in Fig. 5.1 represents the input of the DTLL, consisting of the balun which is loaded by the differential TL loop (CG). As discussed

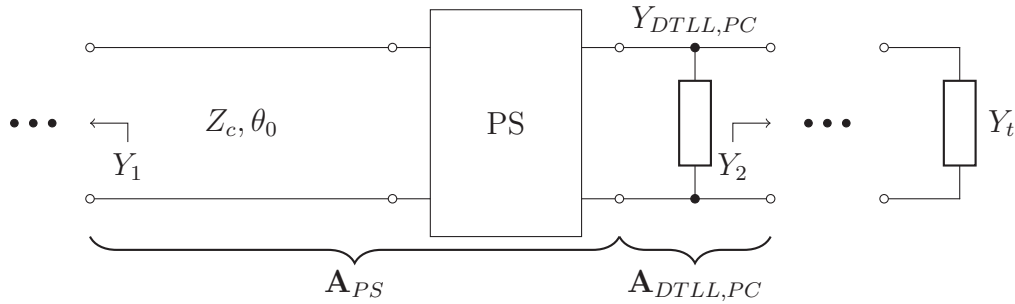


Figure 5.1: Representation of phase shifted DTLL element.

in Section 4.3.5, the loop admittance will always be located within the angular interval $[0, \pi/2]$ of the Smith chart, with an amplitude in reflection coefficient close to unity. An interesting property of the balun impedance transformation of the LP topology, treated in Paper F, is the approximate radial shift towards 50Ω , when the loop is in the loaded state, which occurs in the presence of the inlay. This shift is small, due to the high- Q nature of the loaded loop and may be described by adding a high value shunt resistance to the input admittance of the balun. A numerical investigation, using the design rules of Paper F, shows that reasonable component values may be used for the balun realization when the source and load admittances are conjugate values of each other, with some angular distance from the $\Gamma = 1$ point. Extreme component values are approached for $\Gamma = 1$. This implies that the transformed single ended inductive input impedance of the balun is close to the differential loop impedance loading the balun. Consider next a phase compensation of the balun input impedance, indicated by the added index PC , to the $\Gamma = 1$ point. The resulting input impedance of the balun is a high resistance value, which shifts towards 50Ω in the loaded state. The reason for the phase compensation is to avoid any additional phase shift to that provided by the PS element. Strictly seen, this only holds at the operating frequency, but yet still the frequency shift is small when the input impedance of the balun is reasonably close to the $\Gamma = 1$ point.

The array is terminated by an admittance (Y_t), after the last element. The value of the terminating admittance is nominally chosen to the 50Ω system impedance, but may deviate from this value to compensate for the non-ideal phase compensation that arises due to the loaded state, to achieve acceptable input return loss of the coupler array.

5.2 Predictive model

With reference to Fig. 5.1, the combined network of the phase shifter and the DTLL may be described by the cascade $ABCD$ -matrix $\mathbf{A} = \mathbf{A}_{PS}\mathbf{A}_{DTLL,PC}$, where \mathbf{A}_{PS} and $\mathbf{A}_{DTLL,PC}$ represent the phase shifted TL segment and DTLL, respectively. For the evaluation of the source environment presented towards element i , the composite

$ABCD$ -matrices up to and after this element are given as

$$\mathbf{B}_i = \mathbf{A}^{i-1} \mathbf{A}_{PS} \quad \mathbf{C}_i = \mathbf{A}^{N-i}. \quad (5.1)$$

By evaluating the composite $ABCD$ -matrix $\mathbf{D}_i = \mathbf{B}_i \mathbf{C}_i$, representing element i loaded with the remaining elements unloaded, the total input admittance of the coupler array is given as

$$Y_{in,i} = \frac{d_{i,21} + Y_t d_{i,22}}{d_{i,11} + Y_t d_{i,12}} \quad (5.2)$$

which can be rearranged for the terminating admittance giving a matched condition at the input as

$$Y_{t,m} = \frac{Y_0 d_{i,11} - d_{i,21}}{d_{i,22} - Y_0 d_{i,12}}. \quad (5.3)$$

In a prediction the balun transformation is chosen as the ideal lossless model. Furthermore, only one DTLL-element at a time in the array is assumed to be loaded. This implies that, given the source environment represented by $Y_{s,i}$, the mismatch in the reference plane represents the coupling between the array and the inlay transponder, provided a highly efficient coupling element with a power gain close to unity is used. A compact way of describing the performance, is to evaluate the mismatch circles, for a given required coupling, in the $\Gamma_{s,i}$ -plane of the Smith chart for each loaded DTLL separately, using the circle theory given in Section 2.3.3. If $\Gamma_{s,i}$ is located inside the mismatch circle for each case, and simultaneously the input reflection coefficient Γ_{in} , given by (5.2), fulfills required values of magnitude and bandwidth, the required operating performance of the coupler array is satisfied.

5.3 Example using a phase compensated line

To clarify the preceding theory, an example using phase compensation as the PS element is considered. The topology is shown in Fig. 5.2, where the more general network of phase compensation is used, as compared to the short segment approximation in Paper G. The $ABCD$ -matrix of the phase compensated TL element is given as

$$\mathbf{A}_{PC} = \begin{pmatrix} (1 + ZY) \cos \theta + jZ_c Y \sin \theta & (Z(1 + ZY) + Z) \cos \theta + jZ_c(1 + ZY) \sin \theta \\ Y \cos \theta + j(1 + ZY) \frac{\sin \theta}{Z_c} & (1 + ZY) \cos \theta + j(Z(1 + ZY) + Z) \frac{\sin \theta}{Z_c} \end{pmatrix} \quad (5.4)$$

with

$$\begin{aligned} Z &= \frac{1}{j\omega C_{PC}} & C_{PC} &= \frac{\sin \theta_0}{\omega_0 Z_c (1 - \cos \theta_0)} \\ Y &= \frac{1}{j\omega L_{PC}} & L_{PC} &= \frac{Z_c}{\omega_0 \sin \theta_0}. \end{aligned} \quad (5.5)$$

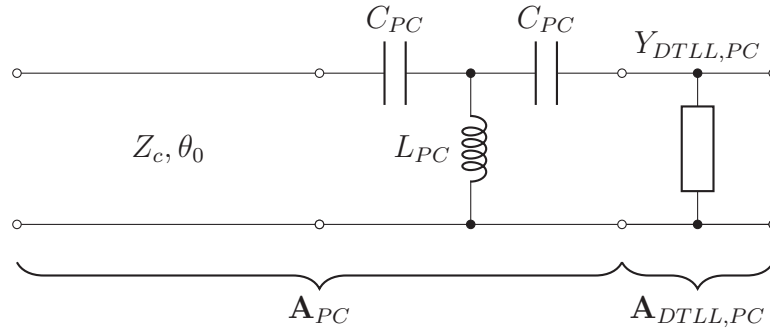


Figure 5.2: Representation of phase compensated DTLL element.

The phase angle is frequency dependent and given as $\theta = \sqrt{\varepsilon_{eff}}l\omega/c$, where ε_{eff} and l are the effective dielectric constant and physical length of the TL. c is the speed of light.

An array of 9 super elliptic DTLL elements is considered. For a realistic frequency dependent load, the material parameters are chosen for a loop TL characteristic impedance of 88Ω , with a loop length of 74 mm and 0.63 dB/m loss. For these values (4.2) is used. A maximum allowed mismatch of 15 dB is chosen. For an input power of 5 dBm from the interrogator this would correspond to -10 dB transponder input power for the used lossless approximation.

By carrying out the necessary nodal analysis of the balun, the resulting situation is shown in Fig. 5.3. The black dashed curve indicates the original state of the unloaded loop impedance locus over the frequency band 825–1025 MHz. The operating frequency, here chosen as 925 MHz, is indicated by the circle marker. From EM simulations of the CG to IG interaction between the DTLL and inlay, a shunt resistance of 1000Ω is a common value, which is transformed by the balun to the solid black curve. As clearly seen, the balun transformation has a strong impact on the bandwidth performance. The blue set of curves are the stacked data of the presented source impedance values for each individual element, given by (5.1). As seen, all of the loci reside within the 15 dB mismatch circles margin, indicated in gray. It is hence concluded that the coupling performance is satisfactory. Finally, the input reflection coefficients of the coupler array, for each separately loaded element, is plotted in red, with dB-values given in Fig. 5.4. An input match of better than 10 dB over a 5% bandwidth is predicted. The calculation of the terminating admittance, according to (5.3), gives no improvement in this example.

In summary, the model gives a good estimate of the limitations in performance of the coupler. As compared to the work in Paper G, showing wide band performance in return loss, the balun loading clearly, both in the unloaded and loaded state, has a dominating impact on bandwidth.

5.4 Concluding remarks

The presented predictive model serves as an initial estimation. As discussed in Paper F, parasitics in the balun layout have a strong impact, hence making the

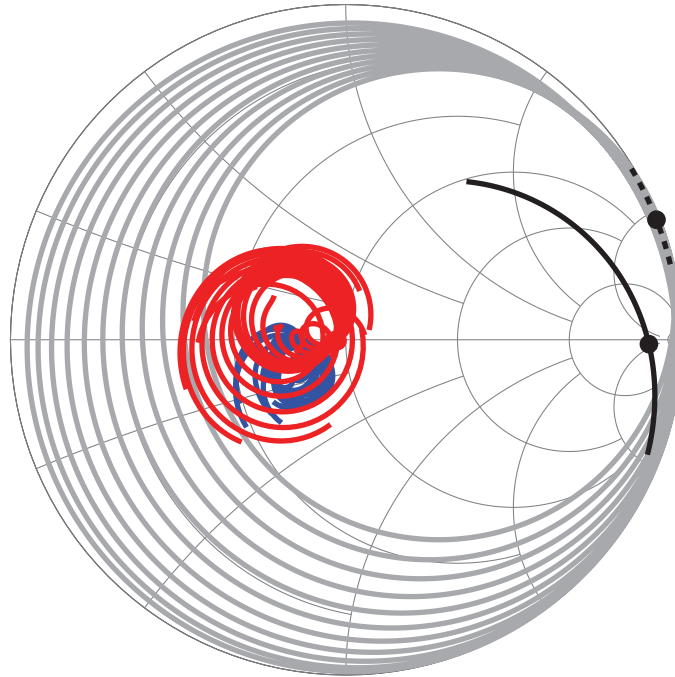


Figure 5.3: Predictive model. Black dashed: Unloaded loop (CG) input impedance. Black solid: Phase compensated balun transformed state. Blue: Stacked data of presented source impedance towards each individual element. Red: Coupler array input impedance for each respective element in loaded state. Gray circles: 15 dB mismatch circles in the $\Gamma_{s,i}$ -plane.

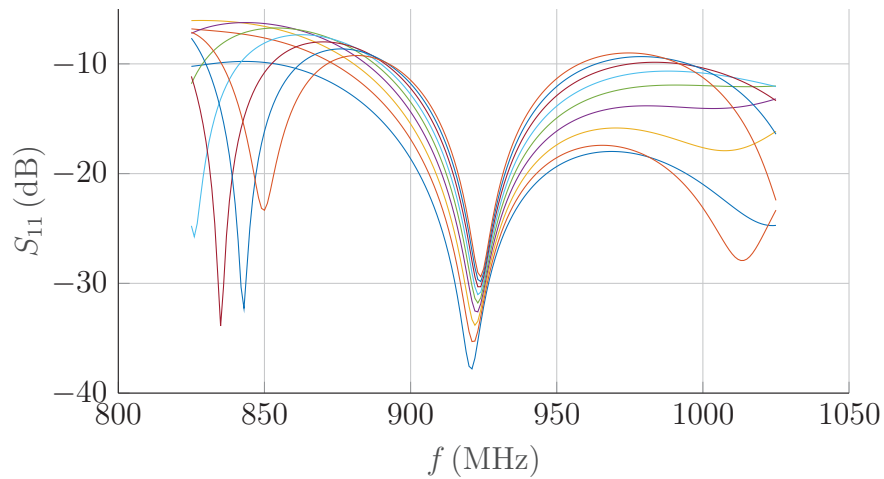


Figure 5.4: Return loss prediction (red curves in Fig. 5.3).

balun a critical component. However, for the presently considered cases of complex impedance transformation, the EM optimized design for the required component values agrees quite well with the ideal lumped circuit model. The advantage of the present analysis is the independency of any particular loop geometry, making it easy to use.

The exact spatial distribution and geometry of the loops in the array is heavily depending upon design criteria. The insensitivity of the DTLL array input impedance

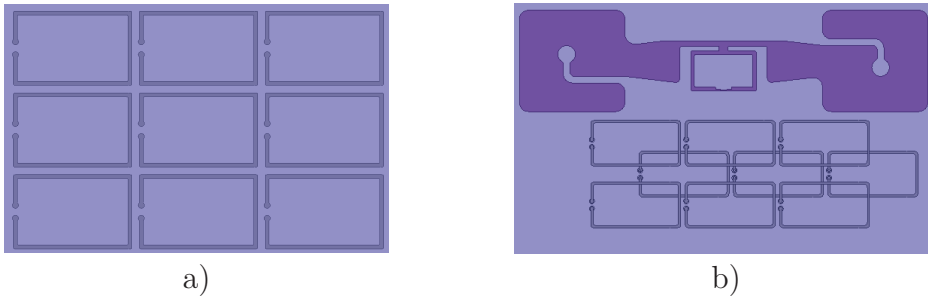


Figure 5.5: Example of 2D loop arrays. a) Coplanar array. b) Multi layer array with middle row located 0.1 mm beneath the top and bottom rows.

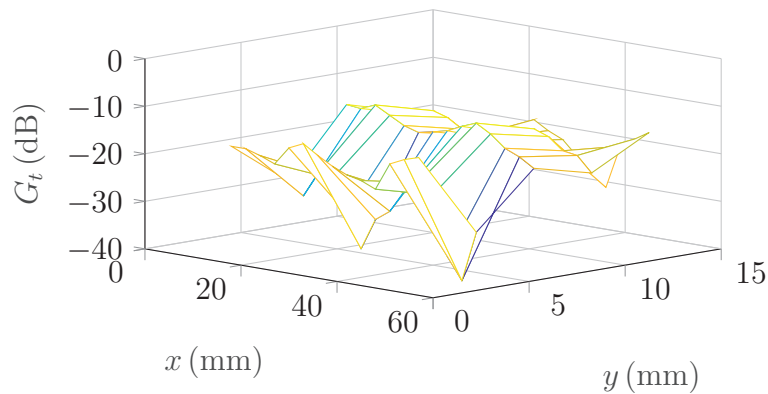


Figure 5.6: EM simulated 2D spatial sweep of coupling at 925 MHz for the CG and IG combination of Fig. 5.5 b).

to the geometrical shaping of the loop (CG) array is a highly interesting property, but expected from the electromagnetically constrained TL behaviour of the DTLL CG. Since high efficiency is concluded on element basis, in a sense this insensitivity also establishes adaptivity. This is due to the fact that wherever the inlay is located within the loop array, highly efficient coupling is established, provided a loop element is present. As concluded in Paper D, the DTLL is a versatile component suitable for highly efficient coupling towards the larger family of inlay geometries (IGs). Furthermore, any loop along the array will suffice, as concluded from the previous analysis.

The possibilities of loop geometry shaping and positioning is currently ongoing design work. Two examples of a three by three element array are shown in Fig. 5.5. The major task is the distribution of the loops in such a way, as to minimize the number of coupling nodes. In Fig. 5.5 b) loops in different layers are considered, which show interesting properties. A spatial plot of the HFSS EM simulated coupling, in terms of the transducer gain (2.2) at 925 MHz, for the CG and IG configuration in Fig. 5.5 b) is shown in Fig. 5.6. The grid resolution is 3 mm. Nodes in coupling are distinguished, but outside the nodes high coupling, up to values of 10 dB, is seen. The balun transformation in this simulation is ideal, since a lumped port excitation is used for the loops in HFSS, which however still gives a valid result at the single frequency.

Chapter 6

Conclusions and future work

A first part of this thesis is the development of FOM theory for RFID transponder chips. The purpose is to find a rigid characterization method and performance measure on transponders, from the black box perspective. Focus is put on common behaviour among the entire family of transponders. The characterization method is used successfully in a predictive model used for highly efficient coupling elements, being the second major part of the thesis.

The differential transmission loop (DTLL) as candidate for highly efficient reactive near field (RNF) coupling towards RFID inlays is explored and a proof of concept is established. The DTLL has promising performance, with coupling efficiencies above 80%. This is demonstrated for several inlay geometries, in which the inductive loop is exploited. This is a fundamental result since these reactive near field properties are common for the larger family of inlay geometries, making the DTLL as suitable candidate for adaptive programming of inlays in the reactive near field. In particular, the transmission line (TL) behavior of the differential loop leads to input impedance properties of array implementations, being independent of loop geometry shaping and positing, which is very attractive from the design perspective.

Balun concepts with inherent complex impedance transformation, based on a modification of the out-of-phase-power-splitter, proves to be a suitable low loss and compact size candidate for the differential excitation of the DTLL. For the simplified topology a balance operating bandwidth of 20% is demonstrated, which fulfills the requirements for operation in RFID applications. For the considered topology, the shift of impedance transformation from the unloaded to load state has attractive properties, in particular when DTLL array configurations are considered.

Future work can be divided into design work, being an industry related part and further research in academia. Loop shaping and positioning in DTLL sensitive array implementations will be concerned with optimization, to minimize coupling nodes over the spatial regions of interest. This is seen as industry related design work. Regulatory circuit concepts, for the on/off switching of coupling array subsets, and fabrication methods are also included in this work. The coupler technology enables a scalable platform applicable to virtually any mechanical environment, which is a requirement from the industry.

From the academic perspective, the properties of non-linear RFID transponder

behavior treated in this thesis suggests a theoretical model, based on clipping behavior, which is common for all types of transponders. Further research is suggested to develop this model.

From yet another academic perspective, the concept of lumped complex impedance transforming baluns is a novel topic with little reported work. As concluded in the present thesis work, complex impedance transformation is highly sensitive to parasitic effects, as seen from the fabricated demonstrators. Further suggested research on this topic consists of integration methods, for a behavior closer to the ideal lumped circuit and for applications at higher frequencies than those considered in the present work.

Appendix A

A short review of the RFID protocol

The measurement of transponder impedance within a pulse relies on the triggering of a wake-up signal with certain timing properties, which are specified in the GS1 Class-1 Generation-2 RFID protocol specification, shortly named Gen2 [2]. The wake up signal is implemented in the measurement system as a pulse profile. In this appendix a short review of critical parameters is made for the reader to get more familiar with what is implemented in the measurement system. The theory described in this section along with terms and their numeric values are extracted from Gen2. The electrical requirements on the RF envelope transient conditions, such as rise time, settling time, overshoot, undershoot etc. are not covered. These are parameters not being critical since data is always captured within a pulse, i.e., no transient conditions are present. For further details the reader is referred to the Gen2 specification.

A.1 Baseband

The basic reference for timing is the type A reference interval, T_{ari} , which is the $Data_0$ length. This means that all other timing parameters have the T_{ari} value as basic building block along with tolerances. Since timing parameters are not fixed but rather reside within intervals information initially needs to be transferred to the transponder. This would be equivalent with the situation where a passive inlay in a non-energized state enters an RF energizing field. This is done by the Query command which initiates an inventory round. The Query command is pre-pended with a preamble, which contains the timing information. Values of the timing parameters are summarized in Table A.1.

The envelope of the Preamble is shown in Fig. A.1. Also shown in Fig. A.1 are the $Data_0$ and $Data_1$ symbols.

High levels represent carrier wave (CW) on and low levels CW off. The difference is essentially the duration of CW on. The pulse width (PW) is the duration of CW

Table A.1: Baseband timing parameters.

Parameter	Min	Max	Unit
$Tari$	6.25	25	μs
$Data_1$	1.5	2	$Tari$
Del (Delimiter)	11.875	13.125	μs
$RTCAL$	2.5	3	$Tari$
$TRCAL$	1.1	3	$RTCAL$

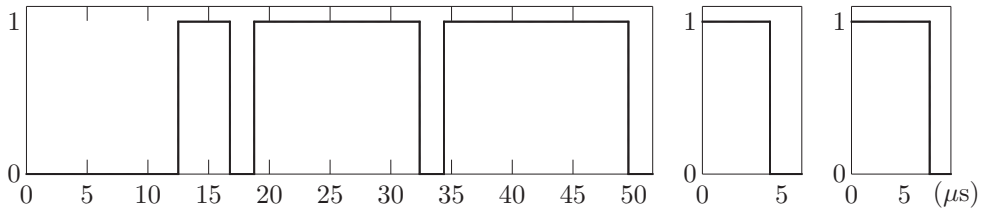


Figure A.1: Base band symbols. Left: Preamble. Right: Data0 and data1 symbols.

off after the transition from high to low. It is required to reside within the interval

$$PW \in [\max(0.265Tari, 2), 0.525Tari]. \quad (A.1)$$

Note that the $RTCAL$ length is always the sum of $Data_0$ ($= 1 Tari$) and $Data_1$ lengths. The Preamble consists of the Del , $Data_0$, $RTCAL$ and $TRCAL$ in sequence. The transponder measures the length of $RTCAL$ and divides it by two. This pivot is then used as decision criteria for subsequent symbols being $Data_0$:s or $Data_1$:s.

A.2 Wake-up signal

Gen2 specifies the command structure for reading and writing operations to the transponder chip. These sub commands are the building blocks of all higher level commands implemented in any interrogator conforming to the specification. Since Paper B focuses on the measurement of low and high level impedance states in the transponder, only the least necessary sub commands are implemented in order to trigger the transponder. The command which will be used is the Query command:

$$\underbrace{1000}_1 | \underbrace{0}_2 | \underbrace{00}_3 | \underbrace{0}_4 | \underbrace{0}_5 | \underbrace{00}_6 | \underbrace{0}_7 | \underbrace{0000}_8 | \underbrace{10111}_9. \quad (A.2)$$

The different groups are explained in Table A.2.

The initial signaling from interrogator to transponder consists of the Query command pre-pended by the preamble explained in Section A.1. In this command sequence all the data needed for the transponder to set up the backscatter signal is contained. The transponder will always give a reply, provided the transponder is allowed to respond. In a multi transponder environment, an anti collision algorithm

Table A.2: The Query command.

Group	Value (binary)	Meaning
1	1000	command name
2	0	$DR = \frac{64}{3}$ (divide ratio)
3	00	$M = 1$ (FM0)
4	0	no pilot tone
5	0	sel:all
6	0	session: S0
7	0	target: A
8	0	$Q = 0$
9	10111	CRC-5

is implemented determining in what order each transponder, one at a time, will respond. Only one at a time can respond or a fault occurs. The Q -value is used for the anti collision algorithm. Basically a high value corresponds to a big population of inlays. In the measurements of Paper B, only one transponder is located in the energizing field, which will imply an immediate response. Therefore $Q = 0$ always.

The divide ratio (DR) is used for the transponder to calculate the back scatter link frequency as $f_{BLF} = DR/TRcal$. The maximum value is chosen. A subcarrier is used for spectrum enhancements in dense interrogator environments. Specifically, in an RFID printer environment with a single interrogator this is not applicable so $M = 1$ always.

A.3 Estimation of maximum required recording time

In Paper B the complete period of events that is considered occur as half duplex communication. This means that the measurement system issues a command sequence, realized as a pulse train. After some time the transponder will reply back by modulating the reflection of the carrier, shifting between two distinct impedance states. The exact time until transponder reply is not known. However, the measurement system used in Paper B has a recording time which can be considered as long. The whole period of events may be repeated under different electrical conditions, such as RF power and carrier frequency. As an estimate for the maximum pulse generation period all parameters described previously are maximized according to Gen2. The period or link timing can be expressed as

$$T = t_{pr} + t_{QUERY} + t_{CW,1} + t_{reply} + t_{CW,2} \quad (\text{A.3})$$

where

$$\begin{aligned}
t_{pr} &= Del + Tari + RTcal + TRcal \\
t_{QUERY} &= 15Tari + 6Data_1 \\
t_{CW,1} &\in \max \left(RTcal, 10 \frac{TRcal}{DR} \right) [0.85, 1.15] \\
&\quad + [-2, +2] \mu s \\
t_{reply} &= 23 \frac{TRcal}{DR}, \quad t_{CW,2} \in [3, 20] \frac{TRcal}{DR}.
\end{aligned} \tag{A.4}$$

t_{QUERY} is based on the number of symbols in (A.2). t_{reply} is based on the six symbol FM0-preamble, 16 symbol RN16 and *dummy1* symbol according to Gen2. Maximizing (A.4) according to Table A.1 yields a maximum pulse generation period of roughly $T_{max} = 1.6$ ms.

In the measurement system of Paper B the described link timing defines a single sweep in the vector network analyzer. The RN16 is a random based sequence, issued by the transponder. It would then be impossible to measure the impedance within a pulse for these symbols. However, the FM0-preamble is fixed, although the timing resides within intervals specified by the protocol. Yet still, the pulse time is long enough as to capture stable values of complex impedance over sweeps. Hence, the FM0-preamble serves as impedance data set. An averaging over sweeps is done in a post analysis process.

A.4 Minimum required system bandwidth

The reference for calculation of the required bandwidth is the timing of the transponder reply. From Gen2 the FM0 baseband signal has a minimum duty cycle of 45%. The shortest pulse width in the transponder reply, is obtained from the maximum backscatter link frequency by choosing the minimum value of $TRcal$ in Table A.1, given as $2.75 Tari_{min} = 17.2 \mu s$. By taking into account the duty cycle and $DR = 64/3$, the minimum pulse length to be resolved is $0.36 \mu s$ which roughly corresponds to a required system bandwidth of 2.8 MHz.

Appendix B

Graphical user interfaces

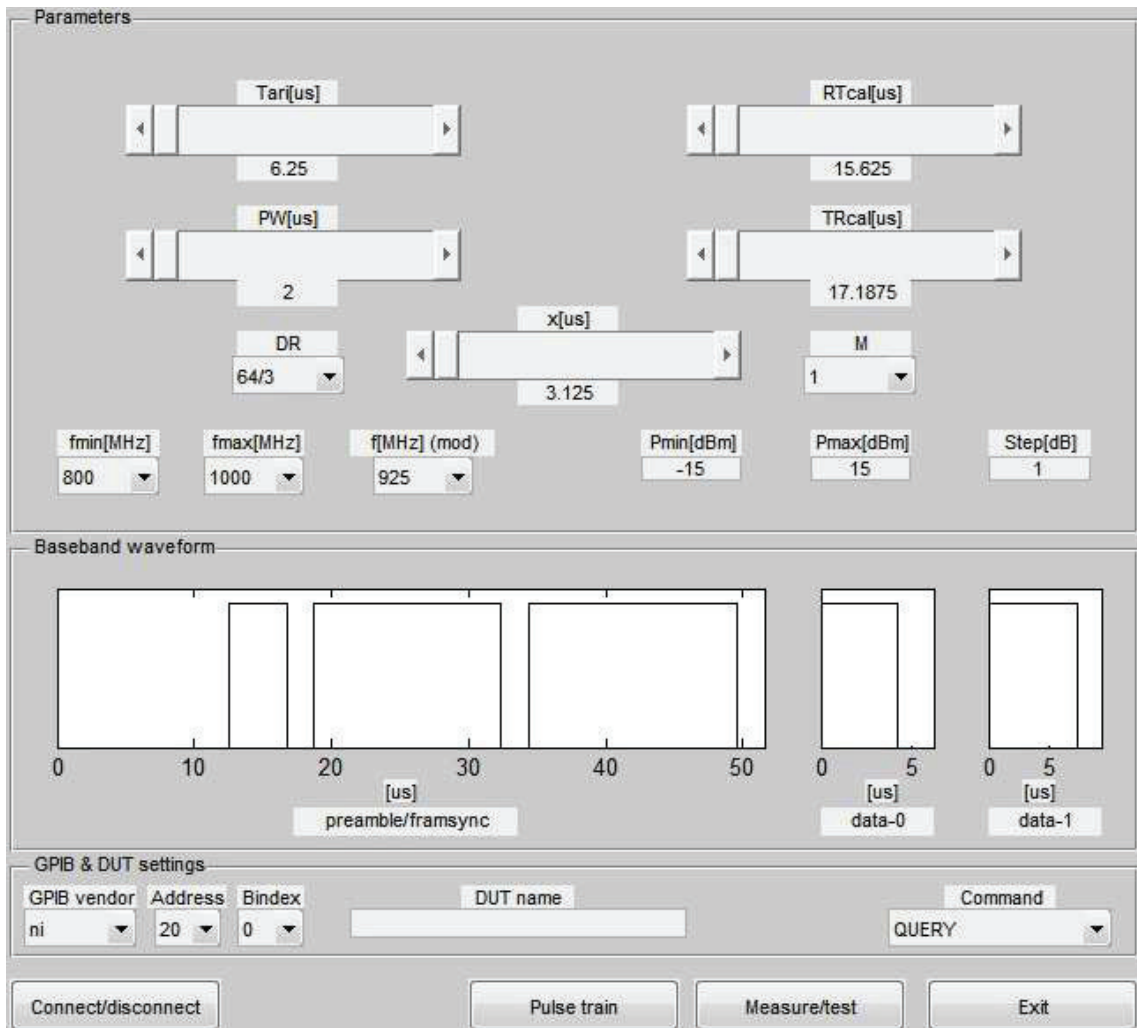


Figure B.1: RFID application GUI.

In Paper B transponder chips from several vendors with several individuals of each are measured. Many repetitive moments are required. MATLAB offers a

vast functionality for the design of graphical user interfaces (GUI), with an easy to implement control of R&S instrumentation. This is utilized to program an application/measurement GUI, shown in Figure B.1

The major functionality that is provided consists of the baseband signal design, initialization of the GPIB connection, and start of measurement sweeps using SCPI commands. The baseband signal may be arbitrarily designed, where the timing parameters are constrained to intervals specified by Gen2 [2]. Except calibration of the ZVA/ZVAX, which is a manual step, the instruments are run remotely during the entire measurement.

After a measurement sweep has been completed, using any of the combinations listed in Section 3.6, data is stored on the host PC. Since data is not averaged in the VNA, a partially manual post analysis procedure is needed before the final quantities can be calculated. The reason for the external post analysis is the removal of dead sweeps. Otherwise the average would be erroneously calculated. A MATLAB GUI was also programmed for post analysis, shown in Figure B.2.

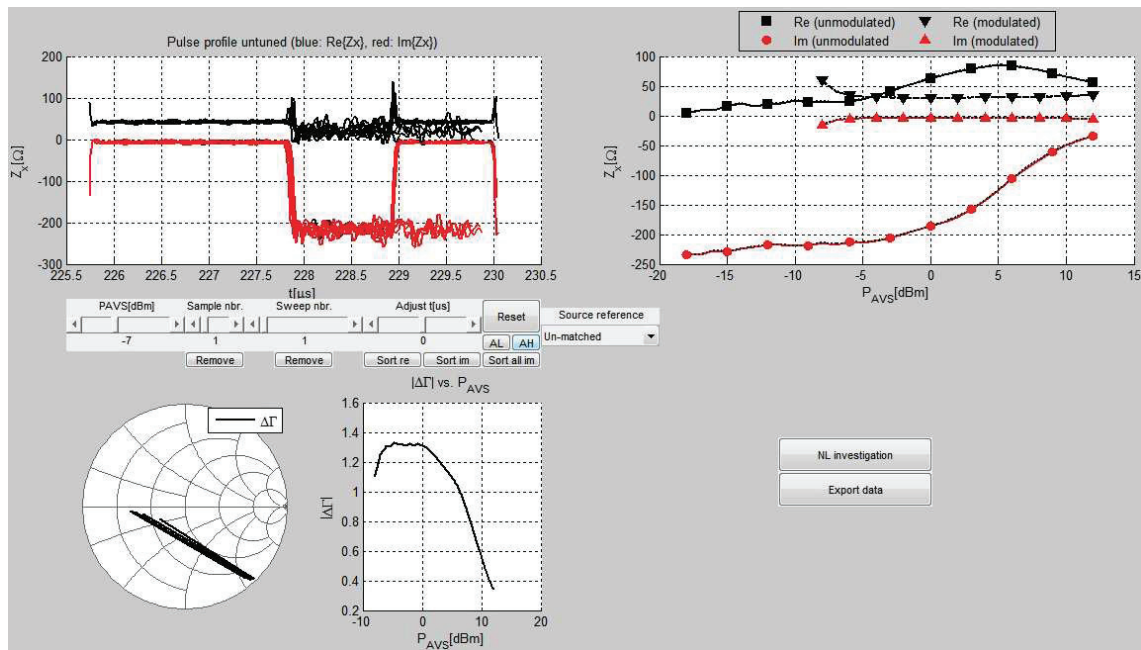


Figure B.2: GUI for the post analysis.

One of the important features in the post analysis GUI is the sorting of pulse profile samples. An algorithm for adding time offsets has been implemented. The sorting is done separately for real and imaginary data, using the identical algorithm. Hence, it suffices to only take the imaginary part as example. In practice it is observed that the biggest change in impedance for the transfer from low to high pulse state occurs for the imaginary part, making the imaginary part algorithm the most used. The algorithm is implemented as follows. The pulsed reactance data is stored in an $M \times N$ matrix $X = (x_{kl})$, where M is the number of sweep points in time and N is the number of sweep samples. Let $X_{min} = \min(X)$ and $X_{max} = \max(X)$

be the minimum and maximum value of reactance in X , respectively. The pivot $\bar{X} = (X_{min} + X_{max}) / 2$, is then used as threshold value for the assignment of ones or zeros, according to

$$x_{norm,kl} = \begin{cases} 0, & x_{kl} \leq \bar{X} \\ 1, & x_{kl} > \bar{X} \end{cases}, \quad k, l \in [M \times N]. \quad (\text{B.1})$$

The result is a an $M \times N$ matrix $X_{norm} = (x_{norm,kl})$ with only zeros and ones, serving as indicators for low and high impedance state, respectively. The first column of X_{norm} , $X_{norm,1}$ is now used as reference, where the flipped versions of the remaining columns, $X_{norm,k}$, $k = 2, 3, \dots, N$, are being convolved with the reference

$$C_k = \left(x_{norm,Mk}, x_{(norm,M-1)k}, \dots, x_{norm,2k}, x_{norm,1k} \right)^t * X_{norm,1}, \quad k = 2, 2, \dots, N. \quad (\text{B.2})$$

C_k is an $2M - 1$ vector, which will have a maximum value at indices $i_{k,max,l}$, $l = 1, 2, \dots, L$. Note that usually the maximum value is not unique. Further, $i_{k,max,l} > M$ is possible. The chosen value $i_{k,max}$ is taken as

$$i_{k,max} = \begin{cases} i_{k,max,l}, & \max_l (i_{k,max,l}) > M \\ i_{k,max,1}, & \text{else.} \end{cases} \quad (\text{B.3})$$

If the minimum time step in the sweep is δt , the time offset for each sample is finally calculated as $\Delta t_k = i_{k,max} \delta t$.

Summary of appended papers

Paper A

Differential Impedance Measurement Method of RFID Transponder Chips at UHF

The paper presents a novel dual probe connection method for direct on wafer characterization of RFID transponder chips. The dual probe connection enables a connection to chip of varying sizes factors.

I developed the concept/idea with theory, carried out the measurements and wrote the manuscript.

Paper B

Shifted Source Impedance and Non-Linearity Impact on RFID Transponder Communication for Drive Level Offsets

The paper develops a theory for non-linear characterization of RFID transponder chips, based on mismatch theory. A figure of merit (FOM) is defined and used in a performance comparison between commercially available transponders from different vendors.

I developed the concept/idea with theory, carried out the measurements and wrote the manuscript.

Paper C

A Simplified Model for the Electromagnetical Interaction between Two Differentially Fed Sub-Wavelength Transmission Line Loops

The paper develops a field theoretic model, based on mutual coupling parameters, for the interaction between two arbitrary shaped closed current loops located in parallel planes. From the derived impedance parameters conclusions are drawn on the impact of geometric overlap, being useful for explaining certain phenomena addressed in the theory of Paper D.

I developed the concept/idea with theory, carried out the simulations and wrote the manuscript.

Paper D

Differential Transmission Line Loop for RFID Reactive Near Field Coupling

The paper presents the differential transmission line loop (DTLL) as a novel and highly efficient coupling element for reactive near field programming of RFID inlays. By utilizing reactive near field properties of the inlay with localized coupling to the closed current loop, common for all inlays, geometry independency is achieved with very high coupling factors.

I developed the concept/idea with theory, did the design, carried out the simulations/measurements, and wrote the manuscript.

Paper E

Lumped Element Balun with Inherent Complex Impedance Transformation

The paper presents a novel concept of lumped balanced to unbalanced transformation with inherent complex impedance transformation. This is an extension from the real to real case used as excitation in the design of the DTLL in Paper D, to achieve a more compact design. The design is based on the modification of the out-of-phase-compensated-power-splitter topology.

I developed the concept/idea with theory, did the design, carried out the simulations/measurements and wrote the manuscript.

Paper F

Design Equations for Lumped Element Balun with Inherent Complex Impedance Transformation

The paper is an extended paper of Paper E for the special issue of the IEEE-TMTT. In the paper, in addition to the balance parameter theory, further equations and theory are provided for the unique determination of all component values in the balun, from requirements on a fully matched state.

I developed the concept/idea with theory, did the design, carried out the simulations/measurements and wrote the manuscript.

Paper G

Phase Compensated Transmission Line for Leakage Field Coupling in UHF RFID Applications

The paper develops theory of segmented and phase compensated transmission lines, with the target application of reactive near field coupling towards RFID inlays. The theory is reused for array implementations of the DTLL (Paper D) in the final chapter of the thesis.

I developed the concept/idea with theory, did the design, carried out the simulations/measurements/tests and wrote the manuscript.

Bibliography

- [1] K. Finkenzeller, *RFID Handbook: Fundamentals and Applications in Contactless Smart Cards, Radio Frequency Identification and Near-Field Communication*. Hoboken, NJ, USA: Wiley, 2010.
- [2] GS1 EPCGlobal Inc., “EPC™ Radio-Frequency Identity Protocols Generation-2 UHF RFID,” Apr. 2015.
- [3] GS1 EPCGlobal Inc., “EPC™ Radio-Frequency Identity Protocols EPC Class-1 HF RFID Air Interface Protocol for Communications at 13.56 MHz,” Sept. 2011.
- [4] B. Y. Tsirlin, “UHF RFID Antennas for Printer-Encoders Part 1,” *High Frequency Electronics*, vol. 6, no. 9, pp. 28–39, Sept. 2007.
- [5] B. Y. Tsirlin, “UHF RFID Antennas for Printer-Encoders Part 2,” *High Frequency Electronics*, vol. 6, no. 10, pp. 36–45, Oct. 2007.
- [6] B. Y. Tsirlin, “UHF RFID Antennas for Printer-Encoders Part 3,” *High Frequency Electronics*, vol. 6, no. 11, pp. 18–25, Nov. 2007.
- [7] M. Frank, “Magnetic RFID Coupler With Balanced Signal Configuration,” US Patent 8,022,815, 2011.
- [8] L. M. Chiu, “Capacitively-Coupled RFID Encoder,” US Patent 7,348,885, 2008.
- [9] B. Y. Tsirlin, M. Tian, and K. Torchalski, “Near Field Coupling Devices and Associated Systems and Methods,” US Patent 8,791,874, 2014.
- [10] B. Y. Tsirlin *et al.*, “Encoding Module, Associated Encoding Element, Connector, Printer-Encoder and Access Control System,” US Patent 8,878,652, 2014.
- [11] GGB Industries, inc., Naples, FL 34101, USA, <http://www.ggb.com>, Feb. 2016.
- [12] G. Gonzalez, *Microwave Transistor Amplifiers*. Prentice Hall, 1997.
- [13] D. Pozar, *Microwave Engineering*, 4th ed. Wiley, 2012.
- [14] R. E. Collin, *Foundations for Microwave Engineering*. McGraw-Hill, 1992.
- [15] C. A. Balanis, *Antenna Theory: Analysis and Design*, 3rd ed. Wiley, May 2005.

-
- [16] P. V. Nikitin, K. V. S. Rao, and S. Lazar, "An Overview of Near Field UHF RFID," in *2007 IEEE International Conference on RFID*, 2007, pp. 167–174.
- [17] J. P. Curty, N. Joehl, C. Dehollain, and M. J. Declercq, "Remotely Powered Addressable UHF RFID Integrated System," *IEEE Journal of Solid-State Circuits*, vol. 40, no. 11, pp. 2193–2202, Nov. 2005.
- [18] A. Facen and A. Boni, "A CMOS Analog Frontend for a Passive UHF RFID Tag," in *Proceedings of the 2006 International Symposium on Low Power Electronics and Design*, 2006, pp. 280–285.
- [19] J. Essel, D. Brenk, J. Heidrich, and R. Weigel, "A Highly Efficient UHF RFID Frontend Approach," in *IEEE MTT-S International Microwave Workshop on Wireless Sensing, Lokal Positioning and RFID (IMWS 2009 - Croatia)*, 2009, pp. 1–4.
- [20] C.-H. Loo *et al.*, "Chip Impedance Matching for UHF RFID Tag Antenna Design," *Progress In Electromagnetics Research*, vol. 81, pp. 359–370, 2008.
- [21] P. V. Nikitin, K. V. S. Rao, R. Martinez, and S. F. Lam, "Sensitivity and Impedance Measurements of UHF RFID Chips," *IEEE Transactions on Microwave Theory and Techniques*, vol. 57, no. 5, pp. 1297–1302, May 2009.
- [22] A. Ghiotto, T. P. Vuong, and K. Wu, "Chip and antenna impedance measurement for the design of passive UHF RFID tag," in *2010 European Microwave Conference (EuMC)*, 2010, pp. 1086–1089.
- [23] H. Yojima, Y. Tanaka, Y. Umeda, O. Takyu, M. Nakayama, and K. Kodama, "Dynamic Impedance Measurement of UHF Passive RFID Tags for Sensitivity Estimation," in *2010 International Symposium on Communications and Information Technologies (ISCIT)*, 2010, pp. 344–349.
- [24] G. A. Vera, Y. Duroc, and S. Tedjini, "RFID Test Platform: Nonlinear Characterization," *IEEE Transactions on Instrumentation and Measurement*, vol. PP, no. 99, 2014.
- [25] J. Essel, D. Brenk, J. Heidrich, R. Weigel, and D. Kissinger, "Large-Signal Measurements and Nonlinear Characterization of an Analog Frontend for Passive UHF CMOS RFID Transponders," *IEEE Transactions on Microwave Theory and Techniques*, vol. 61, no. 2, pp. 948–959, Feb. 2013.
- [26] E. V. Damme, J. Verspecht, F. Verbeyst, and M. V. Bossche, "Large-Signal Network Analysis - A Measurement Concept to Characterize Nonlinear Devices and Systems," Agilent Technologies, Tech. Rep., 2002.
- [27] L. W. Mayer and A. L. Scholtz, "Sensitivity and Impedance Measurements on UHF RFID Transponder Chips," in *The Second International EURASIP Workshop on RFID Technology*, 2008, pp. 1–10.

- [28] D. G. Kuester, D. R. Novotny, J. R. Guerrieri, and Z. Popović, “Simple Test and Modeling of RFID Tag Backscatter,” *IEEE Transactions on Microwave Theory and Techniques*, vol. 60, no. 7, pp. 2248–2258, Jul. 2012.
- [29] S. C. Cripps, *RF Power Amplifiers for Wireless Communications*. Artech House, 1999.
- [30] G. De Vita and I. G., “Design Criteria for the RF Section of UHF and Microwave Passive RFID Transponders,” *IEEE Journal of Solid-State Circuits*, vol. 38, no. 10, pp. 1602–1608, Oct. 2005.
- [31] U. Karthaus and F. M., “Fully Integrated Passive UHF RFID Transponder IC With 16.7- μ W Minimum RF Input Power,” *IEEE Journal of Solid-State Circuits*, vol. 38, no. 10, pp. 1602–1608, Oct. 2003.
- [32] S. A. Maas, *Nonlinear Microwave and RF Circuits*. Artech House, 2003.
- [33] M. Abramowitz and I. A. Stegun, *Handbook of Mathematical Functions*. New York: Dover, 1970.
- [34] K. Kurokawa, “Power Waves and the Scattering Matrix,” *IEEE Transactions on Microwave Theory and Techniques*, vol. 13, no. 2, pp. 194–202, Sept. 1965.
- [35] Rohde & Schwarz, <http://rohde-schwarz.com>, Apr. 2015.
- [36] IEEE, “IEEE standard for higher performance protocol for the standard digital interface for programmable instrumentation,” *IEEE Std 488.1-2003 (Revision of IEEE Std 488.1-1987)*, pp. 1–140, Dec. 2003.
- [37] Maury Microwave, <https://www.maurymw.com>, Apr. 2015.
- [38] S. B. Cohn, “Shielded Coupled-Strip Transmission Line,” *IRE Transactions on Microwave Theory and Techniques*, vol. 3, no. 5, pp. 29–38, Oct. 1955.
- [39] M. K. Krage and G. I. Haddad, “Characteristics of Coupled Microstrip Transmission Lines-I: Coupled-Mode Formulation of Inhomogeneous Lines,” *IEEE Transactions on Microwave Theory and Techniques*, vol. 18, no. 4, pp. 217–222, Apr. 1970.
- [40] M. K. Krage and G. I. Haddad, “Characteristics of Coupled Microstrip Transmission Lines-II: Evaluation of Coupled-Line Parameters,” *IEEE Transactions on Microwave Theory and Techniques*, vol. 18, no. 4, pp. 222–228, Apr. 1970.
- [41] S. B. Cohn, “Characteristic Impedances of Broadside-Coupled Strip Transmission Lines,” *IRE Transactions on Microwave Theory and Techniques*, vol. 8, no. 6, pp. 633–637, Nov. 1960.
- [42] M. Tran and C. Nguyen, “Modified Broadside-Coupled Microstrip Lines Suitable for MIC and MMIC Applications and a New Class of Broadside-coupled Band-Pass Filters,” *IEEE Transactions on Microwave Theory and Techniques*, vol. 41, no. 8, pp. 1336–1342, Aug. 1993.

-
- [43] J. L. Allen and M. F. Estes, "Broadside-Coupled Strips in a Layered Dielectric Medium," *IEEE Transactions on Microwave Theory and Techniques*, vol. 20, no. 10, pp. 662–669, Oct. 1972.
- [44] J. E. Dalley, "A strip-line directional coupler utilizing a non-homogeneous dielectric medium," *IEEE Transactions on Microwave Theory and Techniques*, vol. 17, no. 9, pp. 706–712, Sept. 1969.
- [45] I. J. Bahl and P. Bhartia, "Characteristics of inhomogeneous broadside-coupled striplines," *IEEE Transactions on Microwave Theory and Techniques*, vol. 28, no. 6, pp. 529–535, Jun. 1980.
- [46] F. J. Glandorf and I. Wolff, "A Spectral-Domain Analysis of Periodically Nonuniform Coupled Microstrip Lines," *IEEE Transactions on Microwave Theory and Techniques*, vol. 36, no. 3, pp. 522–528, Mar. 1988.
- [47] D. Kuylenstierna and P. Linnér, "Design of Broad-Band Lumped-Element Baluns With Inherent Impedance Transformation," *IEEE Transactions on Microwave Theory and Techniques*, vol. 52, no. 12, pp. 2739–2745, Dec. 2004.
- [48] J. Choo and J. Ryoo, "Analysis of Flip Chip Bonding for Performance Stability of UHF RFID Tags," *IEEE Transactions on Components, Packaging and Manufacturing Technology*, vol. 4, no. 10, pp. 1714–1721, Oct. 2014.
- [49] M. Frank, M. Thorsell, and P. Enoksson, "Shifted Source Impedance and Non-Linearity Impact on RFID Transponder Communication for Drive Level Offsets," *IEEE Transactions on Microwave Theory and Techniques*, vol. 64, no. 1, pp. 299–309, Jan. 2016.
- [50] N. Marchand, "Transmission Line Transformers," *Electronics*, vol. 17, no. 12, pp. 142–145, Dec. 1942.
- [51] E. G. Fubini and P. J. Sutro, "A wide-band transformer from an unbalanced to a balanced line," *Proceedings of the IRE*, vol. 35, no. 10, pp. 1153–1155, Oct. 1947.
- [52] W. K. Roberts, "A New Wide-Band Balun," *Proceedings of the IRE*, vol. 45, no. 12, pp. 1628–1631, Dec. 1957.
- [53] K. S. Ang and I. D. Robertson, "Analysis and design of impedance-transforming planar Marchand baluns," *IEEE Transactions on Microwave Theory and Techniques*, vol. 49, no. 2, pp. 402–406, Feb. 2001.
- [54] L. F. Tiemeijer, R. M. T. Pijper, C. Andrei, and E. Grenados, "Analysis, Design, Modeling, and Characterization of Low-Loss Scalable On-Chip Transformers," *IEEE Transactions on Microwave Theory and Techniques*, vol. 61, no. 7, pp. 2545–2557, Jul. 2013.

-
- [55] Z. Chen, X. Jiang, W. Hong, and J. Chen, "A Q-band doubly balanced mixer in 0.15 μ m GaAs pHEMT technology," in *2014 IEEE International Wireless Symposium (IWS 2014)*, Mar. 2014, pp. 1–4.
- [56] N. Haider, D. Caratelli, and A. G. Yarovoy, "Frequency Reconfiguration of a Dual-Band Phased Array Antenna With Variable-Impedance Matching," *IEEE Transactions on Antennas and Propagation*, vol. 63, no. 8, pp. 3477–3485, Aug. 2015.
- [57] K. Liu, R. Emigh, and R. C. Frye, "Small Form-factor Integrated Balun with Complex Impedance Matching," in *Microwave Symposium Digest, 2008 IEEE MTT-S International*, Jun. 2008, pp. 1239–1242.
- [58] W. Zhang, Y. Wu, Y. Liu, C. Yu, and W. Chen, "Compact coupled-line balun with complex impedances transformation and high isolation," *IET Microwaves, Antennas Propagation*, vol. 9, no. 14, pp. 1587–1594, Nov. 2015.
- [59] R. S. Michaelsen, T. K. Johansen, and K. M. Tamborg, "Analysis and Design of Complex Impedance Transforming Marchand Baluns," in *Microwaves, Radar, and Wireless Communication (MIKON), 2014 20th International Conference on*, Jun. 2014, pp. 1–4.
- [60] L. K. Yeung and K.-L. Wu, "An LTCC balanced-to-unbalanced extracted-pole bandpass filter with complex load," *IEEE Transactions on Microwave Theory and Techniques*, vol. 54, no. 4, pp. 1512–1518, Jun. 2006.
- [61] M. Frank, M. Thorsell, and P. Enoksson, "Lumped Element Balun with Inherent Complex Impedance Transformation," in *2017 IEEE MTT-S International Microwave Symposium (IMS)*, Jun. 2017, pp. 1285–1288.
- [62] H.-K. Chiou, H.-H. Lin, and C.-Y. Chang, "Lumped-Element Compensated High/Low-Pass Balun Design for MMIC Double-Balanced Mixer," *IEEE Microwave and Guided Wave Letters*, vol. 7, no. 8, pp. 248–250, Aug. 1997.